

LAPPEENRANTA UNIVERSITY OF TECHNOLOGY

LUT School of Energy Systems

Energy Technology

*Moses Irunokhai*

**CFD SIMULATION OF TWO-BUCKET SAVONIUS TURBINE WITH  
NACA 0012 AIRFOIL STATOR VANES**

Supervisor: Associate Professor Aki Grönman

## **FOREWORD**

This thesis was done by Moses Irunokhai within April 2018 to February 2019.

## ABSTRACT

Lappeenranta University of Technology  
LUT School of Energy Systems  
Energy Technology

Moses Irunokhai

### **CFD simulation of two-bucket Savonius turbine with NACA 0012 airfoil stator vanes**

Master's thesis

2019

100 pages, 60 figures, 7 tables and 2 appendices

Examiner: Associate Professor Teemu Turunen-Saaresti (tenure track)

Supervisor: Associate Professor Aki Grönman

Keywords: Savonius, stator vane, rotor bucket, wind turbine, CFD simulation.

To mitigate against the effect of urbanization on the ecosystem, the need for an alternative and renewable source of energy is paramount. This has resulted in increased popularity of wind turbines. Savonius wind turbine is a seamless solution for the urban environment where the wind level is low and unsteady. But, the drawback to this kind of wind turbines is the low coefficient of power.

In this thesis, an attempt was made to improve the performance of the Savonius turbine by the addition of stator vanes. The current study utilizes CFD simulation to analyze the flow within a conventional Savonius rotor and the stator vaned configuration; to help identify the phenomena affecting the performance of the Savonius rotor. Although the addition of the stator did not improve the performance of the Savonius rotor, one key novelty that can be used to improve the performance of the Savonius turbine was observed.

The key novelty was that the use of the downstream stator vanes as was implemented in this study, extends flow attachment on the convex side of the rotor bucket to angle of  $180^\circ$ . On the downside, the observation was that the upstream vanes as implemented in this study, resulted in a reduced rotor bucket performance by reducing the flow attachments to the buckets' convex sides.

## TABLE OF CONTENTS

<b>FOREWORD.....</b>	<b>I</b>
<b>ABSTRACT.....</b>	<b>II</b>
<b>ABBREVIATIONS.....</b>	<b>V</b>
<b>SYMBOLS.....</b>	<b>VI</b>
<b>LIST OF FIGURES .....</b>	<b>VIII</b>
<b>LIST OF TABLES .....</b>	<b>XI</b>
<b>1 INTRODUCTION.....</b>	<b>1</b>
1.1 History and current trends in Wind turbines.....	1
1.1.1 Wind energy trend in EU .....	2
1.1.2 Wind Energy in Finland .....	3
1.1.3 Global Wind Energy Trend.....	4
1.2 Thesis motivation.....	6
1.3 Aerodynamics and modeling of a Savonius turbine .....	7
1.3.1 Aerodynamics of two-bucket Savonius turbine .....	8
1.3.2 Modeling of a Savonius Turbine.....	12
1.4 Organization and limitations of the thesis .....	14
1.4.1 Organization of the thesis.....	14
1.4.2 Limitations of the thesis .....	14
<b>2 LITERATURE REVIEW .....</b>	<b>16</b>
2.1 Experimental investigations of Savonius turbines.....	16
2.2 Simulation investigations of a Savonius turbine.....	20
2.3 Influence of geometry and flow parameters on Savonius type rotors .....	22
2.3.1 Impact of number of rotor buckets.....	22
2.3.2 Impact of number of turbine stages.....	23
2.3.3 Impact of end plates .....	23
2.3.4 Impact of aspect ratio .....	24
2.3.5 Impact of overlap ratio .....	25
2.3.6 Impact of bucket profile .....	26
2.3.7 Effect of Reynolds number .....	28

2.4	Savonius turbine augmentation techniques.....	28
2.4.1	Guide vanes, deflector plates, and guide box.....	28
2.4.2	Multi-turbine interaction .....	31
2.4.3	Stator Vanes .....	32
2.5	Summary .....	34
<b>3</b>	<b>NUMERICAL MODELLING .....</b>	<b>35</b>
3.1	Model description .....	35
3.1.1	The stator vanes.....	36
3.1.2	Stator solidity .....	38
3.2	Simulation procedure .....	38
3.2.1	Solver settings .....	39
3.2.2	Modeling turbulence .....	41
3.3	Mesh generation.....	41
3.3.1	Spatial discretization .....	42
3.3.2	Boundary layers modeling .....	43
3.3.3	Grid dependency study.....	45
3.3.4	Convergence criteria and validation.....	47
3.4	Summary .....	50
<b>4</b>	<b>RESULTS AND DISCUSSION .....</b>	<b>51</b>
4.1	Performance parameters.....	52
4.2	Effect of stator vanes .....	60
4.2.1	Improved torque performance analysis .....	61
4.2.2	Inferior torque performance analysis .....	64
4.3	Results summary .....	67
<b>5</b>	<b>CONCLUSION .....</b>	<b>68</b>
5.1	Findings of the thesis .....	68
5.2	Recommendation for future work.....	69
	<b>REFERENCES.....</b>	<b>71</b>
	<b>APPENDIX I .....</b>	<b>76</b>
	<b>APPENDIX II.....</b>	<b>82</b>

## ABBREVIATIONS

CFD	Computational fluid dynamics
EWT	Environmental Wind Tunnel
EU	European Union
FVD	Finite Volume Method
FVD	Finite Volume Method
GW	Gigawatt
GHG	Greenhouse gases
GBT	Guide box tunnel
HAWT	Horizontal Axis Wind Turbine
MVA	Mega-volt-ampere
MW	Megawatt
SST	Shear Stress Transport
TWh	Tera-watt-hour
VAWT	Vertical axis wind turbine

## SYMBOLS

$2D$	two-dimensional
$3D$	three-dimensional
$A_s$	turbine swept area
$c$	chord length
$C_p$	coefficient of power
$C_m$	coefficient of torque
$C_o$	Courant number
$C_{pm}$	maximum coefficient of power
$c_f$	skin friction
$D$	diameter
$e_d$	discretization error
$e_r$	round-off error
$H$	rotor height
$k$	turbulent kinetic energy
$n_b$	number of blades
$P$	power
$p$	pressure
$Q$	torque
$Re$	Reynolds number
$s/d$	gap spacing ratio
$s$	pitch

$U_{\infty}$	freestream velocity
$\omega$	angular velocity
$\alpha$	azimuthal angle
$\Delta x$	cell size
$^{\circ}$	degree
$\rho$	density
$\nu$	kinematic viscosity
$\tau$	shear stress
$\tau_w$	surface shear stress
$\Delta t$	time-step
$\lambda$	tip speed ratio

**Subscript**

m	moment
mp	maximum power
p	power
$\infty$	freestream



## LIST OF FIGURES

Figure 1-1: Smith-Putnam wind turbine, in Vermont, USA. (Rotor diameter 53.3 m and rated power of 1250 kW). (Hau, 2013).....	2
Figure 1-2: EU wind energy growth from 2008 - 2016. Electricity production (black) increased from 118 TWh in 2005 to 302.9 TWh in 2016. The installed capacity (orange) increased from 65 172 MW in 2005 to 154 847 MW in 2016. Wind Energy Barometer (2010 – 2018).....	3
Figure 1-3: Finland's wind energy growth from 2005 - 2016. Electricity production (black) increased from 0.15 TWh in 2005 to 3.068 in 2016. The installed capacity (orange) increased from 143 MW in 2005 to 1532 MW in 2016. Wind Energy Barometer (2011 – 2018).....	4
Figure 1-4: Regional share of installed capacity for the year 2016. Asia is the market leader 42% share. Data from Wind Energy Barometer, 2018. ....	5
Figure 1-5: Top 10 installed wind capacity by country in 2016. Data from Wind Energy Barometer, 2018.....	5
Figure 1-6: Schematic illustration of a Savonius turbine (Marmutova, 2016). ....	7
Figure 1-7: Actuator disc concept (Burton, et al., 2001). ....	8
Figure 1-8: 2-blades (buckets) and 3-blades (buckets) Savonius turbine (Paraschivoiu, 2002).....	9
Figure 1-9: Savonius rotor - calculation scheme (Paraschivoiu, 2002) .....	10
Figure 1-10: Normalized power coefficient vs. TSR. The thick line is the analytical solution (Paraschivoiu, 2002). ....	12
Figure 2-1: Flow in and around a still Savonius rotor; a: visualized flow field; b: flow inside the rotor; c: flow field; d: surface pressure distribution (Fujisawa & Gotoh, 1992) .....	17
Figure 2-2: Flow in and around a rotating Savonius rotor (TSR=0.9); a: visualized flow field; b: flow inside the rotor; c: flow field; d: surface pressure distribution (Fujisawa & Gotoh, 1992)..	18
Figure 2-3: Comparison of power and torque coefficient of 2- and 3- bucket Savonius rotors with gap width ratio of 0.15 at Re/m of $8.64 \times 10^5$ .....	20
Figure 2-4: Comparison of different turbulence models with experimental data (Roy & UjjwalK.Saha, 2013).....	21
Figure 2-5: Left: Models of single-, two-, three-stage rotor systems. Right: variation of power coefficient with velocity (Saha et al., 2008). ....	23

Figure 2-6: Endplates effect on the performance of a Savonius rotor (Ushiyama & Nagai, 1988)	24
Figure 2-7: Impacts of aspect on two-bucket Savonius turbine (Blackwell, et al., 1977).	25
Figure 2-8: Effect of bucket overlap on the performance of the Savonius turbine (Fujisawa, 1992).	26
Figure 2-9: Comparison of the helical Savonius rotor to the conventional Savonius rotor (Damak, et al., 2012).	27
Figure 2-10: Modified Savonius rotor profiles (Kamoji et al., 2008).	27
Figure 2-11: Re influence on Savonius rotor absolute pressure. (a) $Re = 43,350$ (b) $Re = 867,000$ (Akwa et al., 2012).	28
Figure 2-12: Guide vanes design (A), comparison of power coefficient between the conventional Savonius rotor and modified Savonius rotor with guide vanes (B) (El-Askary et al., 2015).	29
Figure 2-13: A modified Savonius rotor with curtains (A), comparison of power coefficient of conventional and curtain augmented Savonius turbine (B) (Altan & Atilgan, 2008).	30
Figure 2-14: Rotor and guide box tunnel as proposed by (Irabu & Roy, 2007)	31
Figure 2-15: Velocity vector plot for positive interaction condition.	32
Figure 2-16: Generic flow model for the vaned Savonius turbine (Grönman et al., 2018).	33
Figure 2-17. Top view of Omni-directional stator vanes (Shahizare, et al., 2016)	34
Figure 3-1: Savonius rotor with stator vanes	36
Figure 3-2: The lateral distances between two adjacent stators vanes.	37
Figure 3-3: Overview of Pressure-Based Coupled Algorithm (Fluent Inc., 2001).	40
Figure 3-4: Extent of the computational domain	42
Figure 3-5: Selective mesh resolution of the computational domain. The rotor buckets and the stator vanes having the highest resolutions.	43
Figure 3-6: Velocity profile for a turbulent boundary layer (Wilcox, 2006).	44
Figure 3-7: M3 mesh details.	47
Figure 3-8: Grid sensitivity analysis at $TSR = 0.5$ .	47
Figure 3-9: Convergence criteria	48
Figure 3-10: Percentage difference between the last two rotations per TSR.	48
Figure 3-11: Validation for the conventional Savonius rotor	49
Figure 4-1: Rotor angular positions for one complete rotation during transient simulation.	51

Figure 4-2: Performance parameters as a function of the tip speed ratio. (A) Torque coefficient (B) Power coefficient .....	53
Figure 4-3: Torque coefficient as a function of bucket angle at TSR = 0.4. (A) Torque coefficient for the rotor (B) Torque coefficient for the advancing bucket and, (C) Torque coefficient for the returning bucket .....	54
Figure 4-4: Torque coefficient as a function of bucket angle at TSR = 0.5. (A) Torque coefficient for the rotor (B) Torque coefficient for the advancing bucket and, (C) Torque coefficient for the returning bucket .....	55
Figure 4-5: Torque coefficient as a function of bucket angle at TSR = 0.6. (A) Torque coefficient for the rotor (B) Torque coefficient for the advancing bucket and, (C) Torque coefficient for the returning bucket .....	56
Figure 4-6: Torque coefficient as a function of bucket angle at TSR = 0.7. (A) Torque coefficient for the rotor (B) Torque coefficient for the advancing bucket and, (C) Torque coefficient for the returning bucket .....	57
Figure 4-7: Torque coefficient as a function of bucket angle at TSR = 0.8. (A) Torque coefficient for the rotor (B) Torque coefficient for the advancing bucket and, (C) Torque coefficient for the returning bucket .....	58
Figure 4-8: Torque coefficient as a function of bucket angle at TSR = 0.9. (A) Torque coefficient for the rotor (B) Torque coefficient for the advancing bucket and, (C) Torque coefficient for the returning bucket .....	59
Figure 4-9: Control lines A and B for measuring flow parameters. ....	61
Figure 4-10: Streamlines showing particle path for the vaned (left) and vaneless (right) Savonius turbine. ....	62
Figure 4-11: Pressure (left) and velocity (right) of control line A at a rotor angle of attack of $-30^\circ$ .....	63
Figure 4-12: Velocity vector showing the flow around and within a vaned Savonius rotor (left) and a vaneless Savonius rotor (right). Rotor angle of attack is $-30^\circ$ and the tip speed ratio is 0.5. ....	64
Figure 4-13: Velocity and particle path of vaned and vaneless Savonius turbine at TSR of 0.9, and a rotor angle of attack of $-60^\circ$ .....	65
Figure 4-14: Pressure profile of control line B at a rotor angle of attack of $-30^\circ$ .....	66

Figure 4-15: Pressure contour plots of vaned (left) and vaneless (right) Savonius turbine at TSR 0.9 and a rotor angle of attack of $-30^\circ$ .	66
Figure 5-1: Proposed configuration for the Savonius turbine.	69
Figure II-1: Streamlines and velocity vector showing the flow stream in a vaned and vaneless Savonius turbine for various angles at TSR of 0.4. (1) is for rotor angle of 30, (2) is for angle of 60, (3) is for angle of 90, (4) is for angle of 120, (5) is for angle of 150 and, (6) is for angle of 180.	82
Figure II-2: Streamlines and velocity vector showing the flow stream in a vaned and vaneless Savonius turbine for various angles at TSR of 0.5. (1) is for rotor angle of 30, (2) is for angle of 60, (3) is for angle of 90, (4) is for angle of 120, (5) is for angle.	83
Figure II-3: Streamlines and velocity vector showing the flow stream in a vaned and vaneless Savonius turbine for various angles at TSR of 0.6. (1) is for rotor angle of 30, (2) is for angle of 60, (3) is for angle of 90, (4) is for angle of 120, (5) is for angle.	84
Figure II-4: Streamlines and velocity vector showing the flow stream in a vaned and vaneless Savonius turbine for various angles at TSR of 0.7. (1) is for rotor angle of 30, (2) is for angle of 60, (3) is for angle of 90, (4) is for angle of 120, (5) is for angle.	85
Figure II-5: Streamlines and velocity vector showing the flow stream in a vaned and vaneless Savonius turbine for various angles at TSR of 0.8. (1) is for rotor angle of 30, (2) is for angle of 60, (3) is for angle of 90, (4) is for angle of 120, (5) is for angle.	86
Figure II-6: Streamlines and velocity vector showing the flow stream in a vaned and vaneless Savonius turbine for various angles at TSR of 0.9. (1) is for rotor angle of 30, (2) is for angle of 60, (3) is for angle of 90, (4) is for angle of 120, (5) is for angle.	87

## LIST OF TABLES

Table 2-1: Experiment parameters of Blackwell, et al., 1977.	19
Table 3-1: Stator vanes parameters	37
Table 3-2: Stator design parameters	37
Table 3-3: Flow and geometry parameters for calculating first cell height from the wall.	45
Table 3-4: Mesh sensitivity analysis for the vaned configuration.	46

Table 3-5: Mesh sensitivity analysis for the vaneless configuration. ....	46
Table 3-6: Elaborate solver settings for simulated cases. ....	50

# 1 INTRODUCTION

## 1.1 History and current trends in Wind turbines

Wind is air movement caused by the irregular warming of the atmosphere by the sun. Wind Energy Conversion Systems (WECS) exploits the kinetic energy of wind to useful energy. Historically, in the mid-19<sup>th</sup> century, WECS (often called windmills) was generally used for small-scale applications such as water pumping and farming (Schubel & Crossley, 2012). The American engineer, Palmer Cosslett Putnam in October 1942, was the first to actualize the utilization of large wind turbines for electricity generation, see fig 1-1. Although Danish and German engineers in Europe have already developed various concepts, World War II halted the implementation of these concepts. In his design, Putnam developed a two-bladed rotor with 53.5 meters in diameter; installation of a 1250 kW synchronous generator, on a 35.6 m high lattice tower structure (Hau, 2013).

The need for an alternative source of energy, particularly renewable energy, became public interest in 1973 due to the energy crisis. Unending public debates were organized to discuss the dependence of the industrialized western world on oil exporting countries; scientist and engineers with the aid of political support searched for ways to utilize renewables and solve dependencies on oil importation. In the USA, the creation of the US Federal Wind Energy Programme with a budget of about \$ 200 million in 1973 under the Department of Energy (International Symposium on Wind Energy Systems, 1982). In Denmark, a commission of experts proposed that it was possible to generate over 10% of Danish power requirement from wind energy; by giving subsidies to users of wind turbines. In the Federal Republic of Germany, subsidization of wind energy started in 1974, with various programmes under the Bundesministerium für Forschung und Technologie. In Sweden, 280 million Swedish Crowns were made available for the research and development of wind energy in 1975 by the newly created National Swedish Board for Energy Source Development (Hau, 2013). Currently, the trend continues, more countries have a direct and indirect support program for the development of wind energy technology.

Furthermore, in recent times, global participation in the use of wind energy for electricity generation has increased. A good example is in Asia, where China is aggressively developing its

wind energy capacity. Also, Europe and America are not left out in this global race of wind energy development. The next sections present recent trends in the development of wind energy resources in the EU, Finland and globally.



Figure 1-1: Smith-Putnam wind turbine, in Vermont, USA. (Rotor diameter 53.3 m and rated power of 1250 kW). (Hau, 2013)

### 1.1.1 Wind energy trend in EU

With the increasing rate of fossil fuel and coal power plants decommissioning in EU, wind energy became the second largest form of power generation in capacity by 2016 and has come to play a critical role in meeting EU energy mix. Also, EU wind energy capacity has increased from 65 GW in 2008 to 154.8 GW by 2016, with a similar increase in electricity production from wind as shown in figure 1-2. In the year 2017, the EU states decommissioned a total of 11963 MW capacity of coal and fossil (WindEurope, 2018), while installing a cumulative capacity of 14750 MW of wind energy (EurObserv'ER, 2018). The three largest markets, that is, Germany, UK and France with a newly installed capacity of 6440 MW, 4270 MW and 1798 MW respectively in 2017 accounts for 80% of all new installation in EU in 2017. In total, the installed wind energy capacity in Europe at the end of 2017 was 169 GW (onshore and offshore inclusive) with a total electricity production of 336 TWh accounting for 11.6% of EU electricity consumption. Finally, the wind energy forecast

in EU is promising, and growth in the industry is expected to continue with an addition of 25 GW new capacity installation by 2020 (EurObserv'ER, 2018).

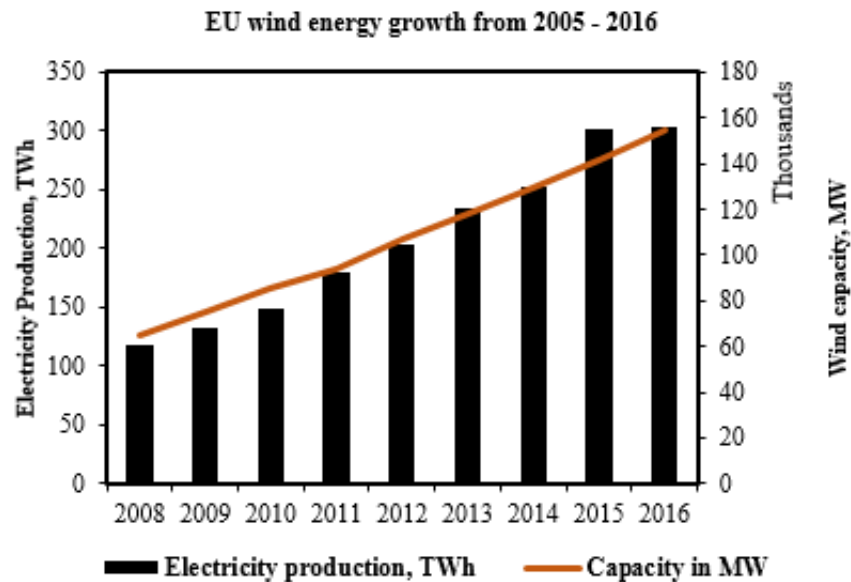


Figure 1-2: EU wind energy growth from 2008 - 2016. Electricity production (black) increased from 118 TWh in 2005 to 302.9 TWh in 2016. The installed capacity (orange) increased from 65 172 MW in 2005 to 154 847 MW in 2016. Wind Energy Barometer (2010 – 2018).

### 1.1.2 Wind Energy in Finland

Wind energy has a critical role to play in Finland's renewable energy mix, as the need to increase the use of clean energy and mitigate against greenhouse gases (GHG) in the power industry continues. In Finland's National Renewable Energy Action Plan (NREAP), the target is to have an installed wind capacity of 2500 MVA and 6 TWh per year, by the year 2020 (Energy Department, 2012). Finland's electricity production from wind has increased from 0.15 TWh in 2005 to 3068 TWh in 2016 (EurObserv'ER, 2018) shown in fig. 1-3. According to WindEurope, Finland added 535 MW to its wind energy capacity in the year 2017, taking Finland's cumulative wind energy capacity to 2113 MW. Also, Finland's wind capacity installation accounted for 3.4% of all new installations made in EU in the year 2017. In the EU (2017) Finland has the fourth largest newly installed wind capacity after Germany, UK, and France respectively. The wind energy outlook in Finland is progressive, as production in Finland is likely to increase to meet the NREAP target.



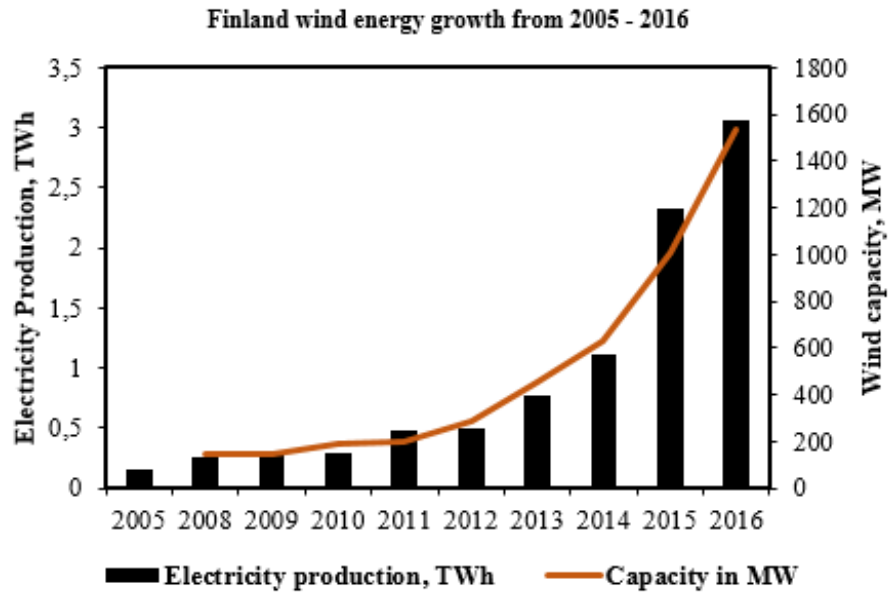


Figure 1-3: Finland's wind energy growth from 2005 - 2016. Electricity production (black) increased from 0.15 TWh in 2005 to 3.068 in 2016. The installed capacity (orange) increased from 143 MW in 2005 to 1532 MW in 2016. Wind Energy Barometer (2011 – 2018).

### 1.1.3 Global Wind Energy Trend

Finally, in a global perspective, the wind energy installed capacity has developed steadily from 17.7 GW in the year 2000 to 539.2 GW in 2017; indicating a landmark achievement in the history of wind energy utilization. Asia was the market leader in wind energy capacity, spearheaded by China (188 GW) and India. Asia accounted for 42% share of worldwide wind installed capacity by the end of 2016, followed by Europe accounting for 33% and North America 20% as presented in fig. 1-4 and fig. 1-5. In Europe, Germany recorded the largest amount of installed wind energy capacity of 56.1 GW taking it to the third position in global rankings. The United States maintained its second position in the global ranking, with an installed capacity of over 89 GW at the end of the year 2017. India was in the fourth position with 32.8 GW installed wind capacity.

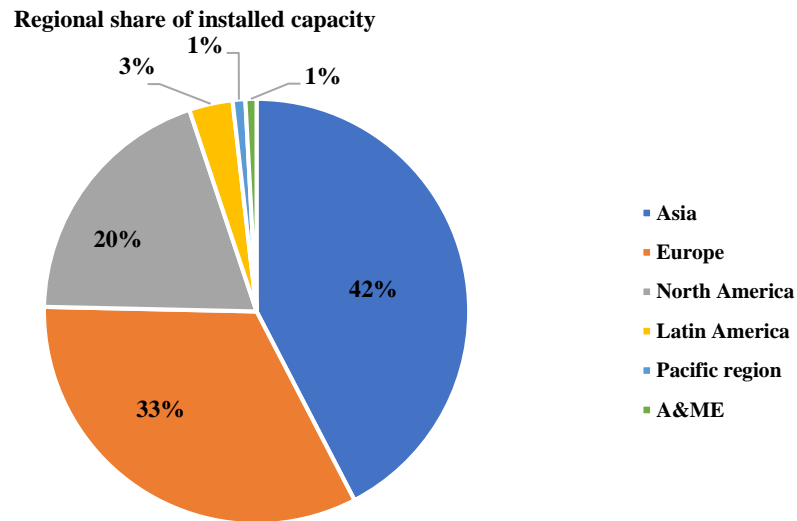


Figure 1-4: Regional share of installed capacity for the year 2016. Asia is the market leader 42% share. Data from Wind Energy Barometer, 2018.

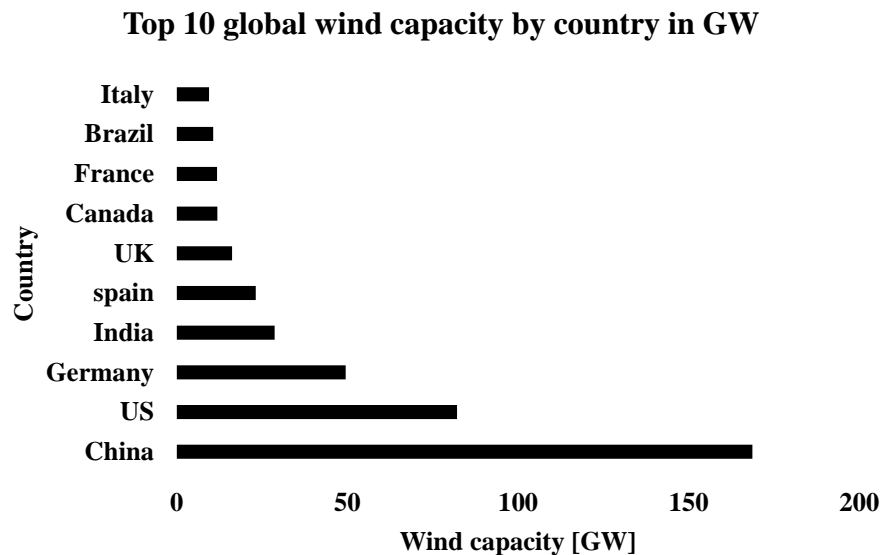


Figure 1-5: Top 10 installed wind capacity by country in 2016. Data from Wind Energy Barometer, 2018.

In conclusion, this section presents the background and the current trends in the development of the wind industry. The current trends indicate that the wind energy market is in an expansion phase. The key drivers of this expansions according to World Energy Resource Wind 2016 are policy support, investors' familiarity and technology maturity and improvement (increased power factor

and availability, production in low wind speed sites). This thesis aims to investigate the possible technological improvement in wind turbines for urban areas low wind speed application by developing, modeling, simulating a Savonius wind turbine with airfoil stator vanes.

## **1.2 Thesis motivation**

Callatay et al., 2011 pointed out that over 70% of the EU population resides in the urban area. Also, consumption of 70% of the produced heat and power is in the city, and the urban areas produce 75% of EU greenhouse gas emission. Recent trends show that urbanization is still increasing. Therefore there is a need to develop an alternative and viable source of renewable energy for urban utilization. Wind energy is the perfect fit to tackle the challenge of energizing the urban cities successfully. However, some challenges arise when trying to utilize conventional wind turbine (HAWT) in an urban area, these challenges include, low wind speed not suitable for HAWT, variable wind direction, and low-frequency aerodynamic noise associated with high level of turbulence in wind turbine wake (Ledo et al., 2011). Therefore for a wind turbine to successfully operate in the urban environment, these challenges must be resolved to an acceptable level; this means that the wind turbine must meet some conditions such as city specified noise level, architectural blend with existing buildings, aesthetic appearance, effective use of low-speed wind and acceptability. The Savonius wind turbine amongst other wind converting machine, especially VAWT, meets the above-listed conditions.

The Savonius wind turbine is a vertical axis wind turbine (VAWT) with curved rotor blades to harvest the incoming wind, to produce a mechanical rotation used to rotate the shaft of the generator. The Savonius wind turbine primarily generates its torque from the drag force in the direction of the wind. Figure 1-6 shows the independence of a Savonius rotor to the wind direction, showing that there is no need for the complex yawing system used in the HAWT. Also, other advantages that make the Savonius turbine suitable for urban utilization include:

- i. Operation at wind speed level associated with an urban environment.
- ii. Ability to operate in multi-directional wind conditions because of its simple geometry.
- iii. The generator is mounted on the ground to ease maintenance requirement both financially and technically.

- iv. The Savonius turbine operates at almost a noiseless condition.
- v. Low cost of fabrication and production.

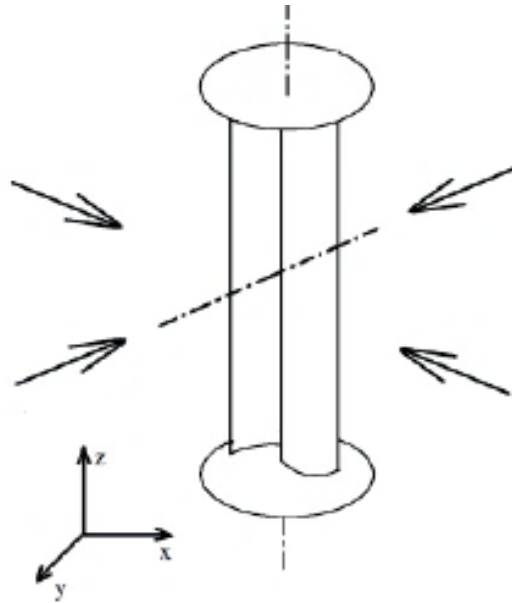


Figure 1-6: Schematic illustration of a Savonius turbine (Marmutova, 2016).

According to (Marmutova, 2016), in her doctoral thesis, she highlighted the potential sites for the successful installation of a Savonius turbine, which are; roofs tops of building, masts, wind tunnels created between proximity buildings and traffic tunnels.

Irrespective of the advantageous qualities discussed above; the Savonius turbine remains unpopular in urban environments. The unpopularity of the Savonius turbine is because of the low coefficient of power associated with the drag type wind converters. The typical power coefficient values of drag operating wind turbines (VAWT) are generally lower than those of lift operating wind turbines (HAWT); this leads to the first research question of **how to effectively increase the aerodynamic power coefficient of the Savonius turbine?**

### 1.3 Aerodynamics and modeling of a Savonius turbine

Wind energy converters are commonly known as wind turbines. A wind turbine converts the kinetic energy of moving wind into mechanical energy for either electrical production (with generators shaft) or other uses like water pumping. The general concept of wind turbine assumes that only the mass of air that passes through the rotor is affected and that the mass of air outside

the rotor is separated and therefore a boundary surface can be drawn between these two masses of air at the rotor. Also, the boundary can be extended to the rotor upstream and downstream; and because no flow of air crosses the boundary, the air mass flow is equal within this boundary (Burton, et al., 2001). The presence of the turbine causes the approaching wind speed to reduce gradually, while pressure increases as it approaches the turbine. After the turbine, the speed of the wind continues its reduction while the pressure experiences an abrupt drop. Finally, because in wind turbine analysis, air is assumed to be incompressible the cross-section of the stream-tube will expand to allow for speed reduction. This concept is known as the Actuator Disc concept, and all wind turbine types work based on this principle.

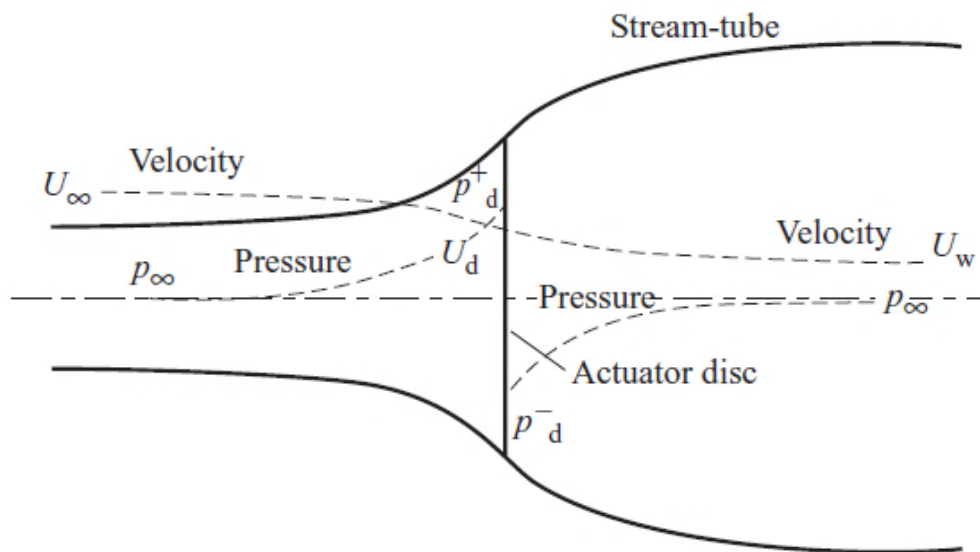


Figure 1-7: Actuator disc concept (Burton, et al., 2001).

### 1.3.1 Aerodynamics of two-bucket Savonius turbine

The Savonius turbine as introduced in the previous section is a VAWT that majorly utilizes drag force to convert wind energy into mechanical energy. The two buckets and the three buckets configuration are the most common configurations investigated by researchers. Figure 2-2 shows the 2-bucket and 3-bucket Savonius turbine configuration.

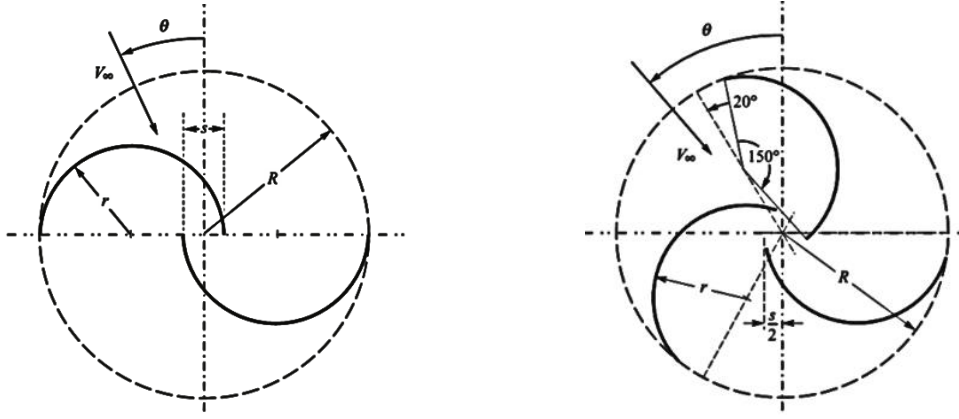


Figure 1-8: 2-blades (buckets) and 3-blades (buckets) Savonius turbine (Paraschivoiu, 2002)

The mathematical model of the Savonius turbine aerodynamics as presented by (Paraschivoiu, 2002) indicates that the total torque acting on a two bucket Savonius turbine is the sum of the individual torque associated with individual rotor bucket.

$$Q = Q_M + Q_D \quad (1.1)$$

Also, the total torque is obtained using the difference in pressure between the advancing blade and the retreating blade.

Mathematically,

$$Q = 2r^2 \cdot H \int_0^{\pi/2} (\Delta P_M - \Delta P_D) \sin 2\theta d\theta \quad (1.2)$$

Where  $r$  is the radius of the rotor bucket for an overlap ratio of 0 (fig 1-9),  $H$ , is rotor height,  $\theta$  is the rotor bucket angular position,  $\Delta P_M$  and  $\Delta P_D$  are the pressure difference on the returning blade and the advancing blade respectively. The change in pressure was evaluated using experimental procedures; the procedure requires the placement of seven pressure gauges on both the front and back surfaces of the advancing and the returning blades. Equation 1.3 present the derived pressure difference correlation based on the gauge measurement.

$$\frac{\Delta P_M^{(f)}}{\frac{1}{2} \rho V_e^2} = K \quad (1.3)$$

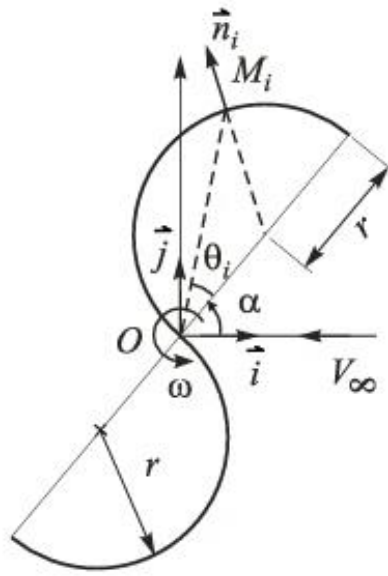


Figure 1-9: Savonius rotor - calculation scheme (Paraschivoiu, 2002)

And,

$$\frac{\Delta P_D^{(f)}}{\frac{1}{2} \rho V_i^2} = K' \quad (1.4)$$

Where  $K$  and  $K'$  are sinusoidal functions of the blade azimuthal angle  $\alpha$  and  $V_e = V_\infty - V_i$  where  $V_\infty$  is the freestream velocity, and  $V_i$  is the absolute velocity on the blade on point  $M_i$ . Inserting equation 1.3 and 1.4 into equation 1.2 gives

$$Q_M = \rho r^2 H K \left[ V_\infty^2 + 2\dot{\alpha}^2 r^2 - \frac{\pi}{2} V_\infty \dot{\alpha} r \cos \alpha - 2V_\infty \dot{\alpha} r \sin \alpha \right] \quad (1.5)$$

And,

$$Q_D = 2\rho r^4 H \dot{\alpha}^2 K' \quad (1.6)$$

The average power,  $P$ , of the Savonius turbine, is the torque (equation. 1.2) integral over the azimuthal angle in the range of 0 to  $\pi$ . Mathematically,

$$P = \omega \cdot Q = \frac{\omega}{\pi} \int_0^\pi Q d\alpha \quad (1.7)$$

And the normalized power coefficient is given by

$$C_P^* = \frac{P}{\frac{1}{2}\rho V_\infty^3 A_s} \quad (1.8)$$

Where \* represents a normalized variable,  $\omega$  is the angular velocity of the turbine and  $A_s$  is the total turbine swept area. Combining equation 1.5, 1.6, 1.7, and 1.8 gives

$$C_P^* = \left[ \frac{K\lambda}{2} \frac{1}{2} - \frac{K\lambda^2}{2\pi} + \frac{K - K'}{K} \cdot \frac{\lambda^3}{4} \right]$$

Making  $K' = K$  eliminates the last term which has no physical implication. Therefore,

$$C_P^* = \left[ \frac{K\lambda}{2} \frac{1}{2} - \frac{K\lambda^2}{2\pi} \right] \quad (1.9)$$

Maximum power coefficient occurs when

$$\frac{dC_P^*}{d\lambda} = 0 \quad (1.10)$$

Solving equation (1.10) using product rule helps to eliminate  $K$ , the resulting solution is substituted back into equation (1.9) gives

$$C_P^* = C_{Pm}^* 16 \left( \frac{\lambda}{\pi} \right) \left[ \frac{1}{2} - \left( \frac{\lambda}{\pi} \right) \right] \quad (1.11)$$

Where  $C_{Pm}^*$  is the normalized maximum power coefficient. Equating  $C_P^*$  to  $C_{Pm}^*$  and solving the resultant equations gives a value of TSR as 0.79 for maximum coefficient of power; this value corresponds to the experiments conducted by Sandia National Laboratories on two blades Savonius turbine with  $s/d = 0$ , the result of the experiment shows that the maximum power coefficient occurs when TSR is close to 0.8. Figure 2-4 shows the comparison between the analytical solution and the experimental results.



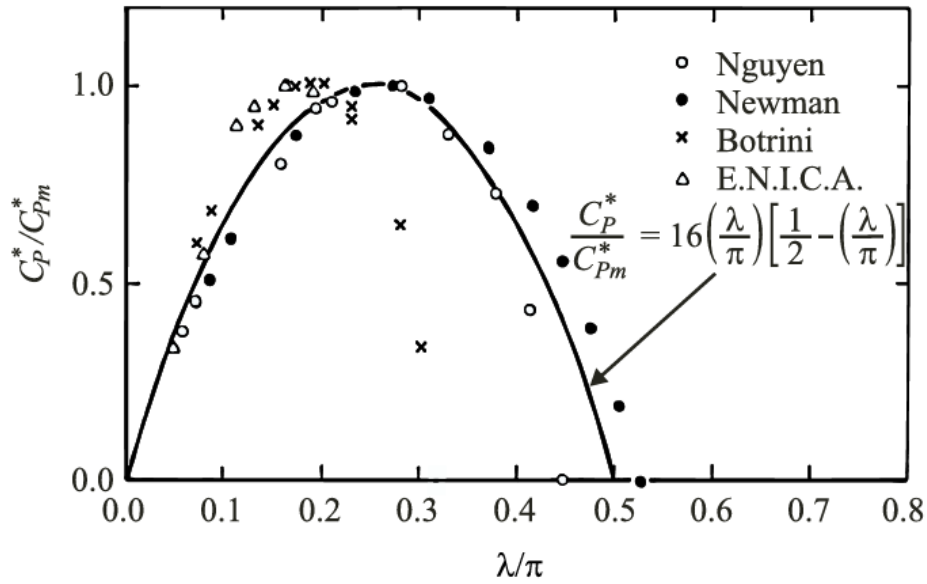


Figure 1-10: Normalized power coefficient vs. TSR. The thick line is the analytical solution (Paraschivoiu, 2002).

### 1.3.2 Modeling of a Savonius Turbine

The most common cost-effective way of modeling a Savonius turbine is the use of computational fluid dynamics (CFD) methods. CFD involves the use of available software (referred to as solvers) to solve the complex partial differential mathematics (governing equations) of fluid mechanics around a body. The interaction of the body and the fluid can either be steady or transient; steady interaction meaning the body is at rest, while transient means that the body is in motion. The simulation of the Savonius turbine utilizes both the steady and the transient solver to calculate the interaction between the turbine and the flow field. The process of modeling a Savonius turbine involves firstly, the construction of the geometry, the generation of the computational domain and finally the use of CFD solvers. Chapter 3 presents the details of the modeling processes.

It is important to point out at this juncture that the utilization of the CFD approach has inherent errors that can adversely affect the results and sometimes cause large discrepancies between simulation results and experimental results. The errors associated with CFD emanates from the deficiencies of the individual process that makes up CFD itself. It is, therefore, impossible to get rid of all the errors in CFD but can be reduced to an acceptable level and validated by experimental results. The prominent errors for Savonius turbine simulations include discretization error, rounding-off error, and convergence error. The discretization error occurs when insufficient mesh

density is utilized to capture the algebraic solution of the governing differential equations inadequately; discretization errors results in over-approximation of the solution (Zikanov, 2010). Another source of error is the rounding-off error. It is the difference between the actual solution of the discretization equation and the exact solution of the discretization equation. A rounding-off error has a direct relationship with the precision limits of a solver, for this thesis the precision of Fluent was double-precision. Double precision means that the calculated values are rounded-off to 15 significant digits. Also, mathematically the discretization error and the round-off error are related as follows. Using the follow notation

$C_{ma}$  is the exact analytical solution of the PDE that represents the Savonius turbine torque

$C_{md}$  is the exact solution of the system of the discretization equation and,

$C_{mn}$  is the actual solution of the system of discretization equation (solver results),

Therefore, the discretization error,  $e_d$

$$e_d = C_{md} - C_{ma} \quad (1.12)$$

And, the round-off error,  $e_r$  is

$$e_r = C_{mn} - C_{md} \quad (1.13)$$

Equation 1.13, indicates that the actual solution differs from the exact solution with the magnitude of the round-off error. In general round-off errors are very small but can sum up quickly if numerous transient simulations are conducted and ruin the results of the simulations (Zikanov, 2010).

The convergence error is the difference between the ideally fully converged solution and the non-converged solution. Nonconvergence of a simulation is typically relative, based on the solver settings. For Fluent the convergence is controlled by the residual tolerance level; a higher residual tolerance level will converge the solution quickly but with inaccurate results, while a very low residual level will require more computational resources but with better solution accuracy. Therefore, trading-off between computational resource requirement and solution accuracy is a dilemma regularly faced in CFD simulations. In this thesis, the residual level was 1e-6 for all variables. This residual value is proposed for VAWT simulation (Balduzzi et al., 2016). Other

factors that affect the solution convergence in Fluent include, boundary conditions, solution initialization, time step size, number of internal iteration and the Courant number.

Noting the errors associated with CFD discussed earlier the second research question arises **how to correctly use CFD to analyze the aerodynamics of a Savonius turbine?**

## **1.4 Organization and limitations of the thesis**

### **1.4.1 Organization of the thesis**

The thesis is made up of five chapters, the first chapter consists of two sections, the first section presents the history and current trends in the wind energy industry. While the second section, discusses the aerodynamics of two bucket Savonius turbine without an air gap, also it informs on the numerical modeling of Savonius turbine and its associated errors. Finally, this chapter presents the research questions.

The second chapter reviews the studies already done on the Savonius turbine. In particular, the chapter highlighted the research trend in the field of the Savonius turbine; presenting both experimental and simulation studies. In this chapter, the influence of various configurations was reviewed and presented. The third chapter discusses the numerical modeling, this includes the model description, the mesh generation, and the simulation procedure.

The fourth chapter presents and analyzes the simulation results. Revealing phenomena that resulted from the modification of the Savonius rotor. While the final chapter gives a conclusion about the thesis, highlighting the findings of this research. Finally, presenting suggestion and further studies opportunities.

### **1.4.2 Limitations of the thesis**

Although the author of this thesis attempts to examine and present physical representative results rightfully, the author is faced with the following limitations:

- i. Various modified Savonius geometries were simulated, but only one was presented and further investigated in this thesis.

- ii. The experimental results of Blackwell, et al., 1977, was used to validate the conventional Savonius turbine presented in this thesis. On the other hand, experimental validation of the modified Savonius turbine is pending and therefore not presented in this thesis.
- iii. This thesis makes use of the 2-D model, which assumes equal distribution of quantities along the rotor bucket height. Using a 2-D model will overestimate the performance of the turbine.
- iv. The total number of cells for the calculation domain was limited to 512,000 cells in accordance with the Ansys Student license requirement.
- v. This thesis investigates only the aerodynamics properties of Savonius turbine.

## **2 LITERATURE REVIEW**

The expectation of wind power generation in urban areas has increased, these expectations are, for example, small-scale generation for household use, the combination with solar power, and cogeneration of energy required by larger buildings. Although the HAWT has been able to meet some of these expectations its is highly unsuitable for many reasons. These reasons include the requirement of greater wind velocities not expected in city environments. Also, they produce low-frequency noises that are harmful to animals. The Savonius turbine, on the contrary, is not associated with these environmental problems and does not require high wind velocities to start. These qualities of the Savonius turbine has been a source of motivation for researchers to investigate the Savonius turbine further. There have been several types of research done in the field of the Savonius turbine. Researchers have investigated the effects of different configurations amongst which are the number of rotor buckets, numbers of rotor stages, overlap ratio, aspect ratio, endplates, rotor blade shapes, and stator inclusion.

### **2.1 Experimental investigations of Savonius turbines**

Experimental studies were the norm in the early stages of the investigations of the Savonius turbine, but with the recent advancement in computational power and better-improved CFD solvers, simulations have become popular in wind turbine investigations. Irrespective of this shift, experimental investigations remain very important, as they are used to validate simulation results. Therefore, it is necessary at this point to highlight the experimental investigation that contributes to the overall scientific knowledge of the Savonius turbine.

The experimental investigation of the Savonius turbine can be done in both controlled and uncontrolled environment. A controlled condition generally refers to a wind tunnel while an open atmosphere refers to as an uncontrolled environment. The common techniques utilized for Savonius turbine experiments are the flow visualization (Fujisawa & Gotoh, 1992) method and pressure measurement (Blackwell et al., 1977) on rotor buckets. In the experiment of (Fujisawa & Gotoh, 1992) the aerodynamics of the flow around and within a Savonius turbine was visualized alongside pressure measurements for both still and a rotating Savonius rotor. A remarkable difference between the static and the rotating rotor are as follows.

- i. The downward movement of the separation point. (compare figure 2.1c and figure 2.2c)
- ii. The relative decrease in the pressure coefficients in the convex side of the advancing bucket. (compare figure 2.1d and figure 2.2d)
- iii. Resisting flow caused by rotating effect weakens the Overlap flow. (compare figure 2.1b and figure 2.2b)

The difference in the flow around and within a still and a rotating Savonius rotor is mainly because of Coanda effect at small rotor angles of less than  $45^\circ$  figure 2-2a. For the rotating turbine, the separation of the attached flow occurs at higher rotor angles of  $90^\circ - 135^\circ$ . This attached flow in the rotating rotor contributes to the rotating torque of the rotor (figure 2-2d). But, on the other hand, the stagnation pressure is reduced when compared to the still rotor.

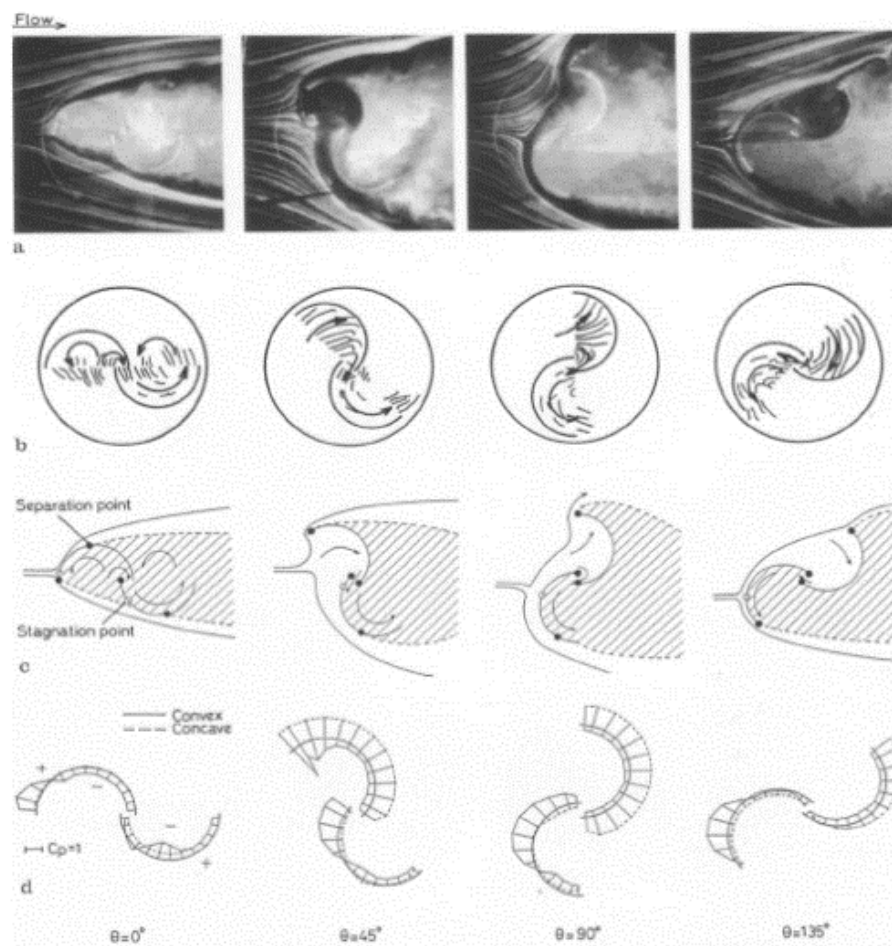


Figure 2-1: Flow in and around a still Savonius rotor; a: visualized flow field; b: flow inside the rotor; c: flow field; d: surface pressure distribution (Fujisawa & Gotoh, 1992)

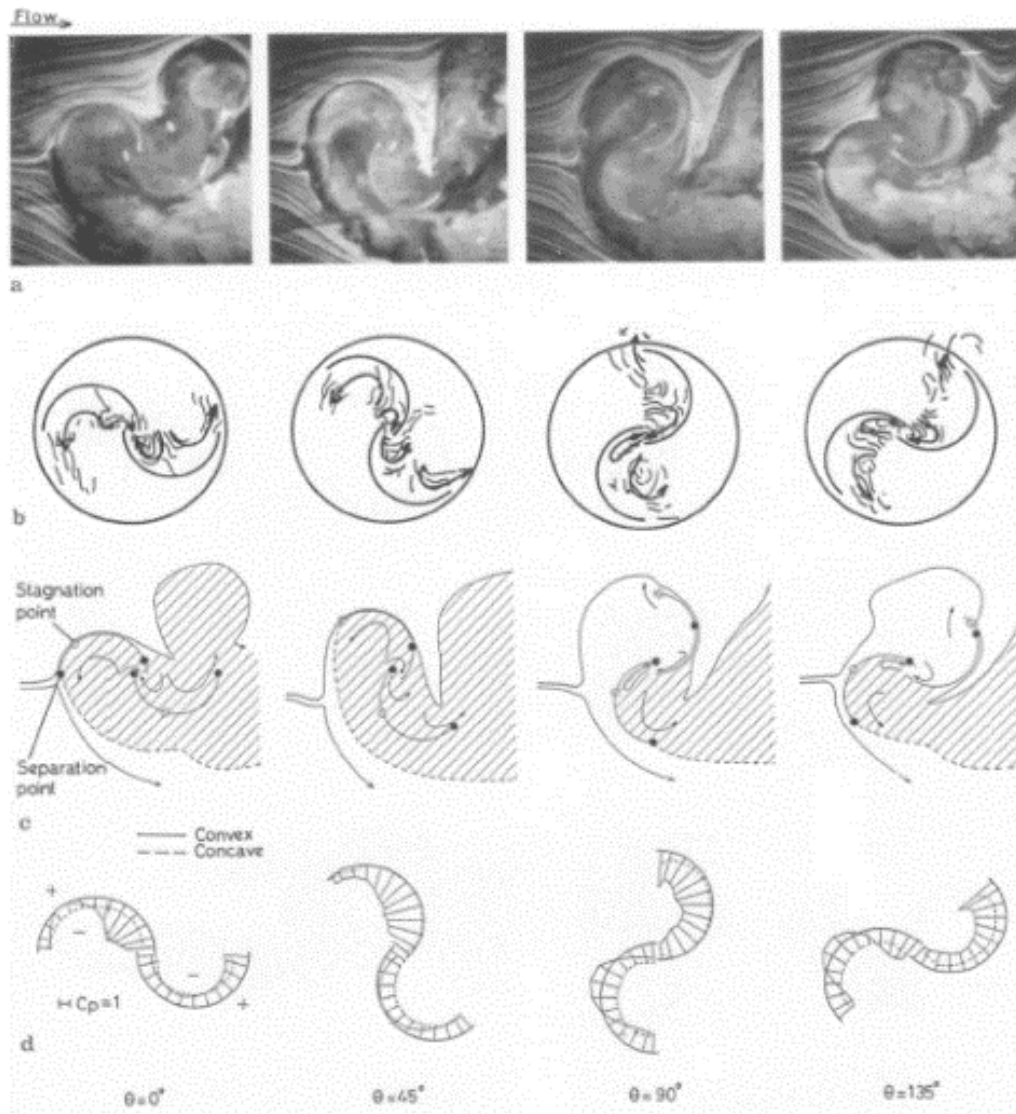


Figure 2-2: Flow in and around a rotating Savonius rotor (TSR=0.9); a: visualized flow field; b: flow inside the rotor; c: flow field; d: surface pressure distribution (Fujisawa & Gotoh, 1992)

(Blackwell, et al., 1977), conducted fascinating experiments that form the bases of result validation for the conventional Savonius rotor in this thesis. The authors conducted wind tunnel tests on various configurations of the Savonius turbine. In the experiments, geometry parameters like the number of buckets, gap spacing, and rotor height were varied. Also, flow parameters such as freestream velocity and the corresponding Reynolds numbers were varied. The table 2-1 presents the varied geometry and flow parameters

Table 2-1: Experiment parameters of Blackwell, et al., 1977.

Parameter	Values
Number of buckets	2,3
Gap spacing (s/d)	0.0, 0.1, 0.15, 0.2
Rotor height	1, 1.5
Freestream velocity	7 m/s, 14m/s
Reynolds number	$4.32 \times 10^5$ , $8.67 \times 10^5$

The experiments took place at the Vought Systems Division Low-Speed Wind Tunnel. The results show that for the three and two buckets rotor configurations except for the no gap configuration, the torque coefficient is all positive for all angular position. Another observation from the experiments was that for the two buckets rotor, the power coefficient peaks at a tip speed ratio close to 0.9 for all configuration; except for the no gap rotor which peaks at close to 0.8. While for the three-bucket configuration the maximum power coefficient was observed at TSR close to 0.6. Also, the three-bucket rotor produces lesser variation in static torque coefficient than the two-bucket rotor.

In comparing the two- and three-bucket Savonius rotors (figure 2-3), it is seen that the two-bucket rotor outperforms the three-bucket rotor on the bases of torque coefficient and power coefficient for all TSR with a factor of about 1.5. Noting that, the only temporary advantage the three-bucket rotor has over the two-bucket rotor is a better starting torque. This temporary advantage is easily removed by utilizing, a multi-stage two-bucket rotor to increase the starting torque as observed by the authors. Finally, the experiments concluded that;

- i. The two-bucket rotor experiences more variable torque per angular position than the three-bucket rotor.
- ii. The two-bucket rotor outperforms the three-bucket rotor aerodynamically, except for starting torque.
- iii. Increase Reynolds number generally increases the aerodynamic performance of all configurations.
- iv. The optimum dimensionless gap is in the range of 0.1 to 0.15.



- v. Finally, the recommended Savonius rotor configuration by the authors is a two-stage two-bucket rotor, rotated at  $90^\circ$  apart, with gap width ratio in the range of 0.1 – 0.15.

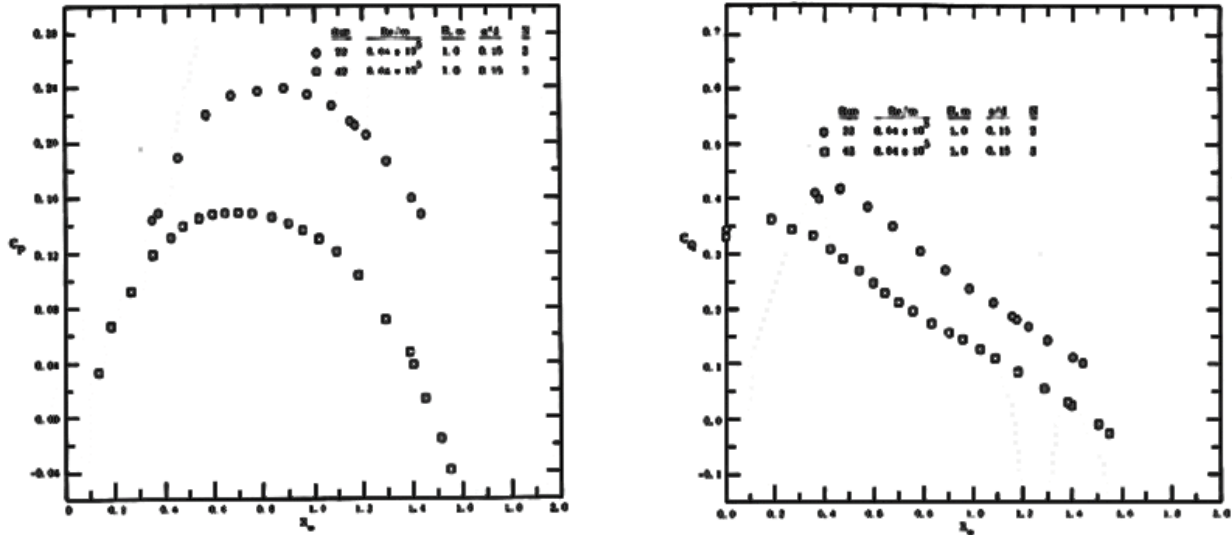


Figure 2-3: Comparison of power and torque coefficient of 2- and 3- bucket Savonius rotors with gap width ratio of 0.15 at  $Re/m$  of  $8.64 \times 10^5$

## 2.2 Simulation investigations of a Savonius turbine

The recent trends in Savonius rotor research are the use of simulation, although CFD has its disadvantages as highlighted in the previous chapter it also has its own merits. The main advantages are that it offers a reduction in the time and cost of conducting studies, that are generally expensive with experiments (Versteeg & Malalasekera, 2007). With the recent advances in high-speed computing, the popularity of CFD has grown immensely in engineering and scientific discipline. Therefore, it comes as no surprise that it is also popular in the analysis of flow within and around a Savonius turbine. The general pattern of Savonius rotor research has been to analyze the performance of the conventional Savonius rotor and after which flow, and geometry parameters are modified, and the effect of such modification on the performance parameters is studied.

Jaohindy, et al., 2013 investigated the effect of using variable aspect ratios, Wenchenubun et al., 2015 investigated the effect of number of blades of a Savonius turbine, El-Askary et al., 2015 simulated the effect of using guiding vanes, while Grönman, et al., 2018 used both experiments

and numerical analysis to study Savonius turbine with airfoil stator vanes. Also, Mohamed et al., 2010 placed an obstacle to shield flow from getting to the returning blade in order to increase the performance of the Savonius rotor.

In other studies, researchers investigated the correctness of different methodologies used in the numerical analysis of the Savonius turbine. Roy & Ujjwal K. Saha, 2013 observed that the use of various simulation techniques has a direct influence on the predicted rotor aerodynamic performance. The study shows that 3D computational study always predicts better result than its 2D counterpart. Also, the 2D simulation always over-predict the aerodynamic performance of the Savonius rotor. Finally, they suggested that the Hybrid Detached-Eddy Simulation (DES) and  $k-\omega$  SST turbulence model captures the unsteady effect of the Savonius rotor more accurately. However, the authors concluded that the 3D  $k-\omega$  SST model shows a close prediction when compared with the experimental results (figure 2-4).

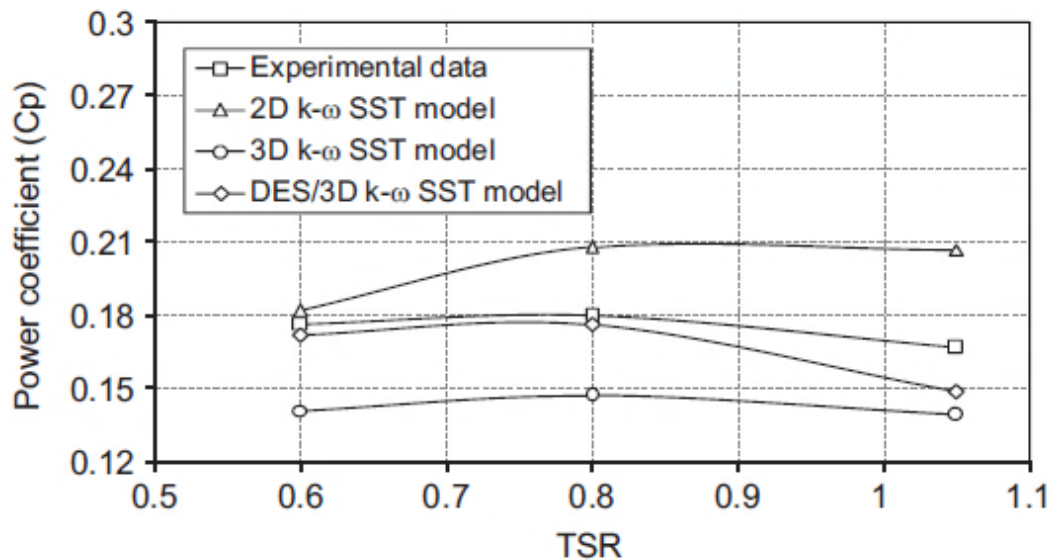


Figure 2-4: Comparison of different turbulence models with experimental data (Roy & Ujjwal K. Saha, 2013).

In another simulation research D'Alessandro, et al., 2010 gained an insight on the flow developing within and around the Savonius rotor; they observed a solid relationship between the variable torque and the TSR and time. Also, the research developed a computational fluid dynamics model for the interaction between the flow field and the rotor blades. Comparing the data obtained at the Environmental Wind Tunnel (EWT) laboratory of the Polytechnic University of Marche, validated

the result of the developed CFD model. Their numerical approach was to develop a computational methodology to solve RANS equations coupled with turbulence model using the Finite Volume Method (FVM) of the Fluent code. The convective term discretization was obtained using the MUSCL approach; the central differencing scheme was used to discretize the diffusive terms. The effect of numerical diffusion was cancelled by using second-order implicit scheme for the time-step. Finally, solving the pressure-velocity coupling with the SIMPLEC approach. The conclusion from the results is that the aerodynamic performance obtained by the developed computational methodology was in agreement with the experimental data. Therefore, the researchers suggest the use of this numerical approach for investigating the Savonius rotor.

### **2.3 Influence of geometry and flow parameters on Savonius type rotors**

Different parameters affect the aerodynamic performance of the Savonius turbine (Akwa et al., 2012). The commonly studied geometry parameters include the effect of end plates, aspect ratio, buckets spacing, buckets overlap, buckets shapes, buckets number, center shaft inclusion, and rotor stages. Also, flow parameter like Reynolds number is commonly studied to observe its effect on the performance of the Savonius turbine.

#### **2.3.1 Impact of number of rotor buckets**

Some studies have been conducted to understand the aerodynamic impact of varying bucket quantities on the Savonius turbine. Sheldahl, et al., 1978 conducted experiments on a various number of buckets and observed that the two-bucket rotor aerodynamic performance was better than that of the three- and four- bucket rotors. The numerical work of (Zhao et al., 2009) compares the power coefficient ( $C_p$ ) of the two- and the three- bucket rotor and found out that the maximum  $C_p$  for the two-bucket rotor is 0.165 and that for the three-bucket rotor is 0.12, which agrees with the work of (Saha et al., 2008). The general observation is that bucket addition to the Savonius rotor reduces the maximum  $C_p$  (figure 2-3). This is because, the added bucket will deflect the air flow that should focus on the next bucket, and this process repeats for the next bucket; therefore, creating a “cascade effect” that reduces the amount of wind energy converted to mechanical energy by the rotor and ultimately reducing the performance of the rotor (Akwa et al., 2012).

### 2.3.2 Impact of number of turbine stages

A common shortcoming of the two-bucket Savonius turbine is the large variation of the static moment at different rotor angle. Saha et al., 2008 wind tunnel tests found that a solution to this inadequacy is the utilization of multi-stage rotors. The authors experimented on single-stage, two-stage and three-stage rotors figure 2-5 (left).

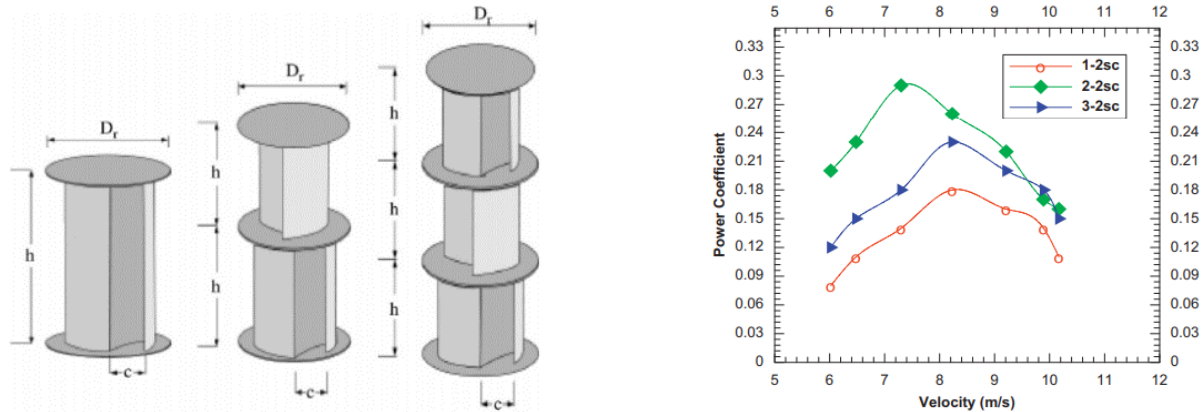


Figure 2-5: Left: Models of single-, two-, three-stage rotor systems. Right: variation of power coefficient with velocity (Saha et al., 2008).

The observation was that the turbine  $C_p$  increased when the number of stages increases from one to two, and  $C_p$  decreases when the number of stages increases from two to three figure 2-5 (right). The authors concluded that the turbine performance decreased when the stages increased from two to three because of the increase in the turbine inertia caused by the addition of the third stage.

### 2.3.3 Impact of end plates

Endplates have positive effects on the aerodynamic performance of the Savonius turbine (Ushiyama & Nagai, 1988) as presented in figure 2-6, this is because the endplates reduce losses by preventing the escaping air from the concave side of the buckets and maintains the pressure difference between the concave and the convex sides of the plates.

The general agreement is that the use of endplates increases the turbine performance, but the endplates thickness should be negligible when compared to the height of the rotor buckets. Furthermore, (Ushiyama & Nagai, 1988) have suggested that the endplates diameter should be 1.1 times the rotor diameter.

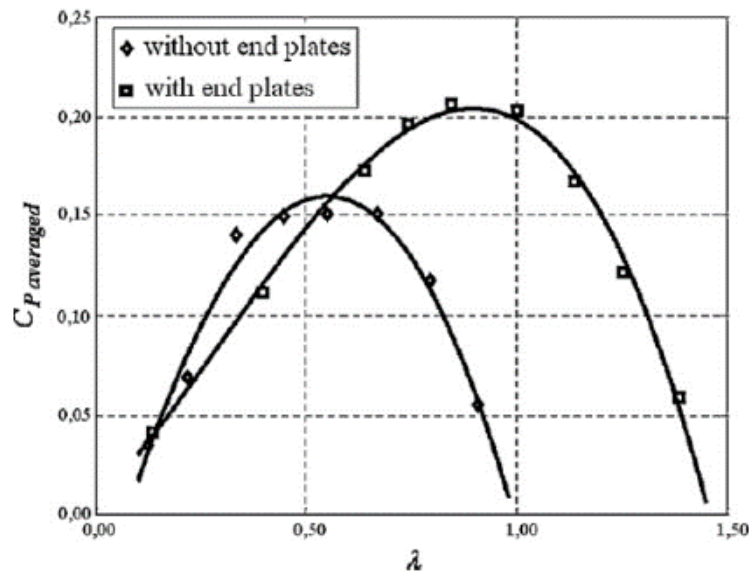


Figure 2-6: Endplates effect on the performance of a Savonius rotor (Ushiyama & Nagai, 1988)

### 2.3.4 Impact of aspect ratio

The aspect ratio is the dimensionless parameter relating the turbine height to the rotor diameter for a conventional Savonius rotor. The observation is that with an increase in aspect ratio, the tip losses reduces; therefore, increased aspect ratio has the same effect as the inclusion of endplates (Akwa et al., 2012). Various literature suggests that an optimum aspect ratio would be within 1 to 2. Blackwell, et al., 1977 also investigated the effect of aspect ratio on Savonius rotor performance. The authors experimented with aspect ratios of 1.0 and 1.5, the observation was that the aerodynamic performance of the rotor with an aspect ratio of 1.5 was better than that of the rotor with an aspect ratio of 1.0.

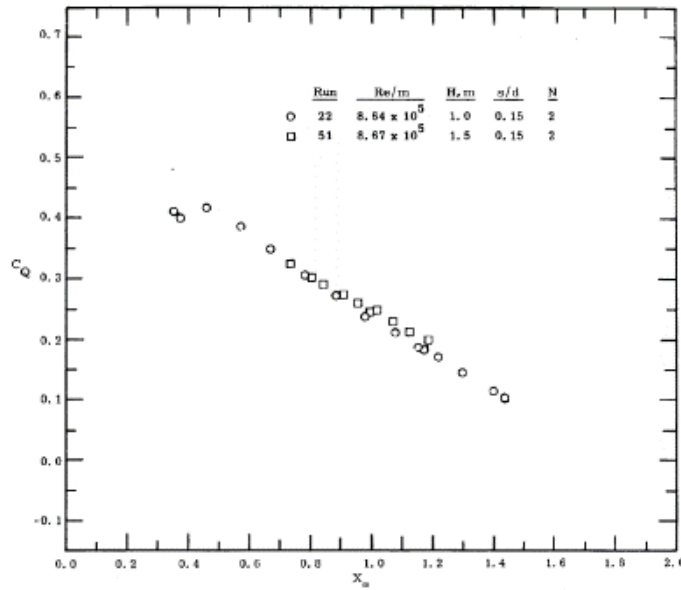


Figure 2-7: Impacts of aspect on two-bucket Savonius turbine (Blackwell, et al., 1977).

### 2.3.5 Impact of overlap ratio

The overlap ratio is the dimensionless ratio of the overlap space and the bucket diameter. Various authors have a different opinion of what is the optimum overlap ratio. Fujisawa, 1992 shown in figure 2-7, and Kamoji, et al., 2008 in their research observed an optimum overlap ratio of 0.15, (Blackwell et al., 1977) said that the optimum value of overlap ratio was between 0.1 and 0.15. (Alexander & Holownia, 1978) and (Mojola, 1985) both gave an optimum overlap ratio in the range of 0.2 to 0.3. According to (Kamoji et al., 2008) the vorticity losses of the Savonius turbine increases at overlap ratios greater than 0.15, which reduces the rotor aerodynamic performance.

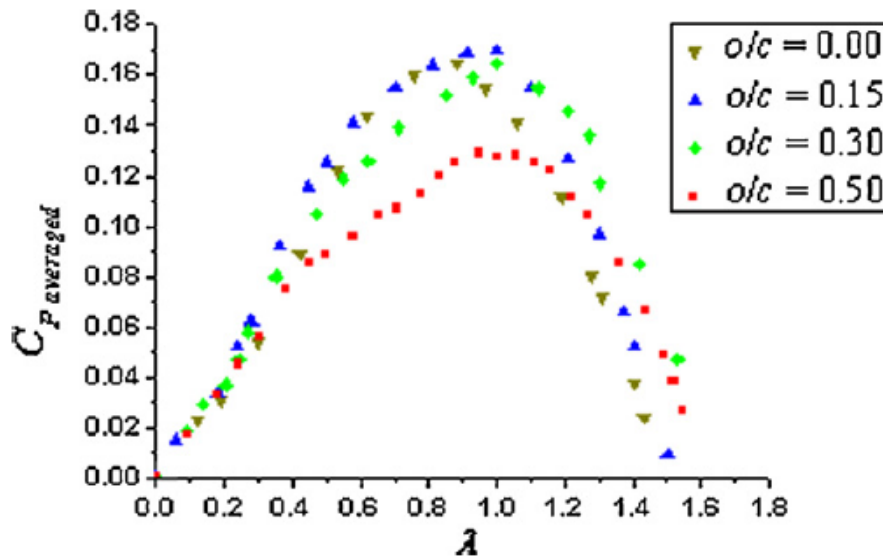


Figure 2-8: Effect of bucket overlap on the performance of the Savonius turbine (Fujisawa, 1992).

### 2.3.6 Impact of bucket profile

Researchers have studied different types of bucket profile; the helically shaped bucket profile is amongst the most studied alternative to the semi-circular rotor. Damak et al., 2012 investigated the aerodynamic behavior of a modified helical Savonius rotor with a twist of  $180^\circ$ . The observation from the authors' experiment was that the Savonius turbine with a helically shaped bucket had better performance than the conventional Savonius rotor as shown in figure 2-8. In the wind tunnel tests of Saha et al., 2008 they investigated the aerodynamic performance of  $12.5^\circ$  twisted buckets (see figure 2-10 A for examples of helically twisted Savonius rotor). The conclusion the authors inferred was that the twisted bucket shows better performance because; in the case of the conventional buckets (semi-circular), the maximum force acts at the center of curvature. While for the twisted bucket geometry, the maximum force acts on the tip of the bucket.

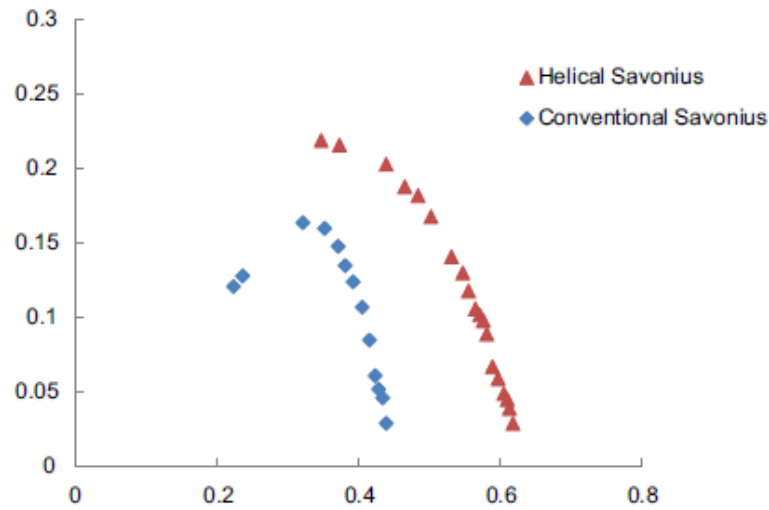


Fig. 9. Comparison of helical Savonius rotor with the conventional Savonius rotor.

Figure 2-9: Comparison of the helical Savonius rotor to the conventional Savonius rotor (Damak, et al., 2012).

(Kamoji et al., 2008) also investigated a modified rotor buckets shape, shown in figure 2-10, in a wind tunnel test. The authors' observation was that the maximum  $C_p$  of the modified buckets was 17%, 11%, and 18% higher when compared to the conventional Savonius turbine at Reynolds number of  $1e5$ ,  $1.2e5$  and  $1.5e5$  respectively.

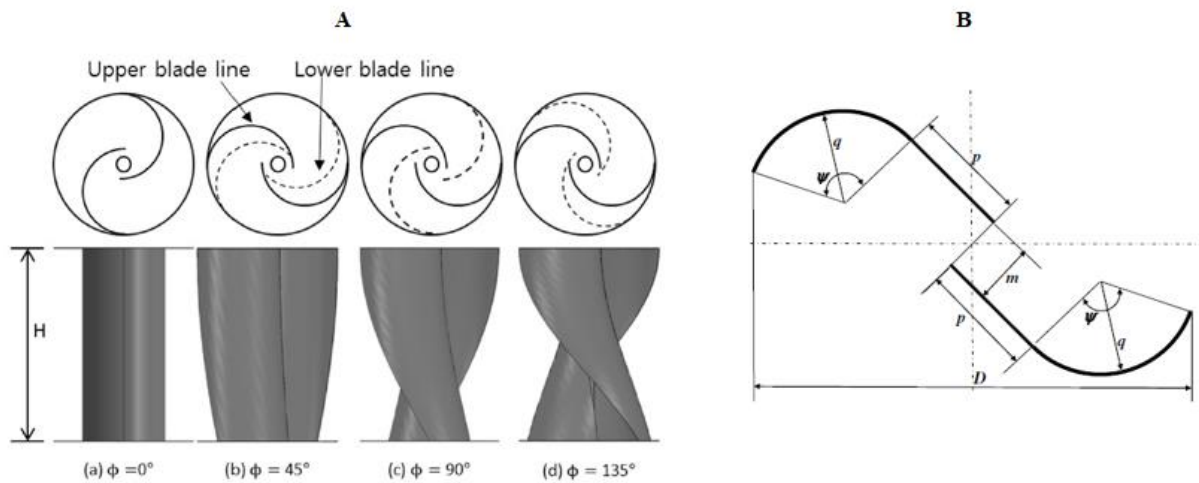


Figure 2-10: Modified Savonius rotor profiles



### 2.3.7 Effect of Reynolds number

(Blackwell et al., 1977) investigated the effect Reynolds number has on the Savonius rotor performance, and the observation was that; with an increase in Reynolds number, the turbine aerodynamic performance improves. The observed improvement is because an increase in the  $Re$  delays the boundary layer separation on the convex side of the bucket. The delayed boundary layer separation increases the lift force contribution to the resultant force at an angular position close to  $0^\circ$  or  $180^\circ$  as seen in figure 2-11 (Akwa et al., 2012).

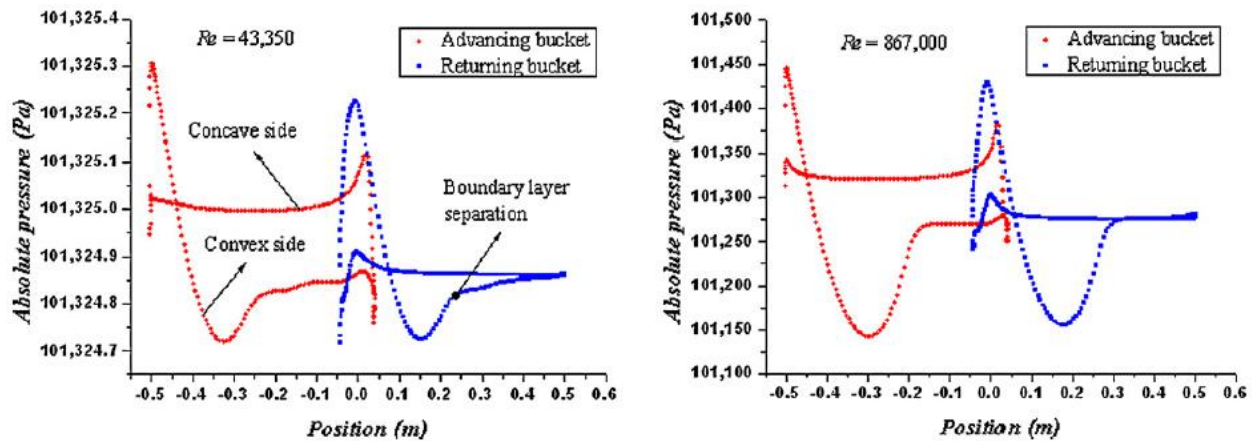


Figure 2-11:  $Re$  influence on Savonius rotor absolute pressure. (a)  $Re = 43,350$  (b)  $Re = 867,000$  (Akwa et al., 2012).

Figure 2-10 shows the influence of increased  $Re$  on the separation point and its contribution to the overall absolute pressure on the Savonius rotor.

## 2.4 Savonius turbine augmentation techniques

In this section, discussion on the improvement of Savonius turbine using additional features such as guide vanes (El-Askary et al., 2015), deflector plates (Altan & Atilgan, 2008), guide box tunnel (Irabu & Roy, 2007), stator (Grönman et al., 2018), and multiturbine interaction (Shigetomi et al., 2011) is presented. In most cases, the ideology is to manipulate the upstream flow, to focus it on the concave side of the advancing blade.

### 2.4.1 Guide vanes, deflector plates, and guide box

El-Askary et al., 2015 researched the improvement of the power coefficient of the Savonius turbine by guiding the incoming flow to the concave side of the advancing and returning blade using

special deflector plate designs shown in figure 2-12A. In the researchers' investigations, three different types of rotor designs were simulated using FLUENT®. The results show that the suggested design with curved passage shape, had no negative torque coefficient and therefore it is possible to self-start. Also, the suggested design resulted in an impressive maximum power coefficient of 0.52 shown in figure 2-12B. However, a significant amount of wake was generated by these new designs when compared to the conventional Savonius rotor. The major drawback of this design is its non-aesthetic outlook and as such not fully suitable for a modern city environment.

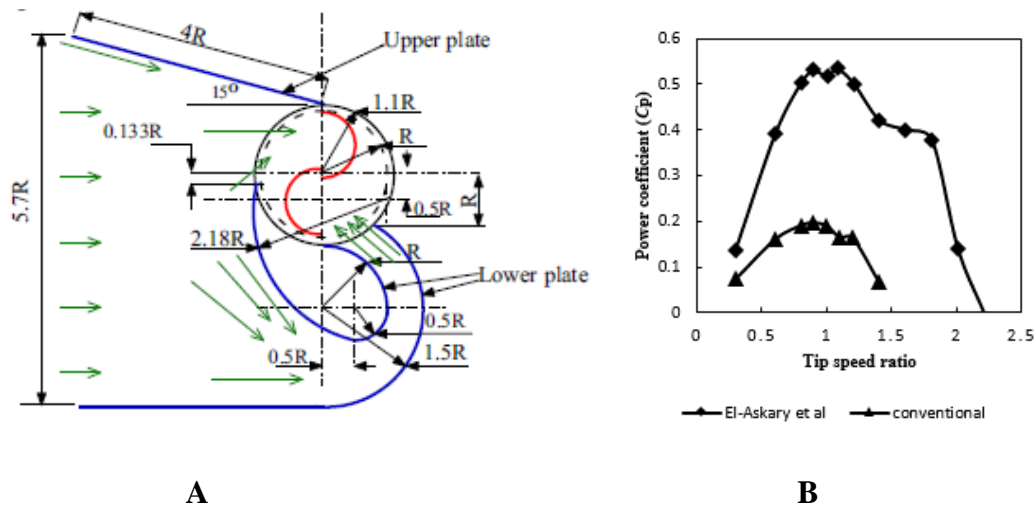


Figure 2-12: Guide vanes design (A), comparison of power coefficient between the conventional Savonius rotor and modified Savonius rotor with guide vanes (B) (El-Askary et al., 2015).

(Altan & Atilgan, 2008) conducted wind-tunnel experiments supported by numerical analysis of the use of deflector plates which are called curtains showed in fig 2-13A. The aim of augmenting the Savonius rotor with the curtains is to decrease the value of negative torque that is generated by the returning blade of the Savonius rotor. Furthermore, the curtains are designed to rotate  $360^\circ$  around the Savonius rotor with the aid of a sensor. The observation from the study shows that the Savonius turbine with curtain design has improved aerodynamic performance compared to the conventional Savonius rotor figure 2-13B. Also, it was observed by the authors that the worst curtain position is when the rotor angle is at  $90^\circ$  to the main flow as shown in figure 2-13A this is because the flow guided by the curtain escapes over the returning blade and increases the negative torque of the turbine. This design, although was able to increase the performance of the Savonius

turbine has a drawback of the complexity of using a wind direction sensor (yawing device) to reposition the curtain based on the direction of the wind.

Irabu & Roy, 2007 experimented with two- and three- blade conventional Savonius turbines augmented with a moving wall guide box as shown in figure 2-14 (note: for two-bucket shown). In this experiment a guide box tunnel (GBT) was used for the following purpose, firstly to increase the Savonius turbine output power and secondly act as a windshield for the Savonius rotor in very gusty wind conditions. The observation from the experiment shows that the utilization of GBT resulted in a maximum power coefficient 1.23 times greater than that of a conventional Savonius turbine for the case of the two-bucket rotor. While for the three-bucket case, the power coefficient of the GBT modified rotor was 1.5 times that of the conventional turbine. The drawback to this design is that it is unfeasible in the large-scale scenario and the guide box has a lot of moving parts which becomes difficult to maintain over time.

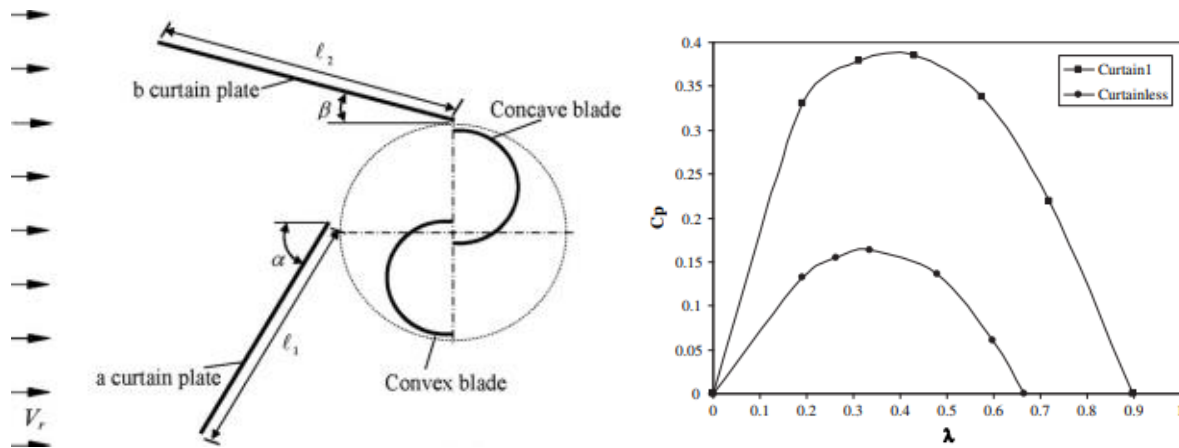


Figure 2-13: A modified Savonius rotor with curtains (A), comparison of power coefficient of conventional and curtain augmented Savonius turbine (B) (Altan & Atilgan, 2008).

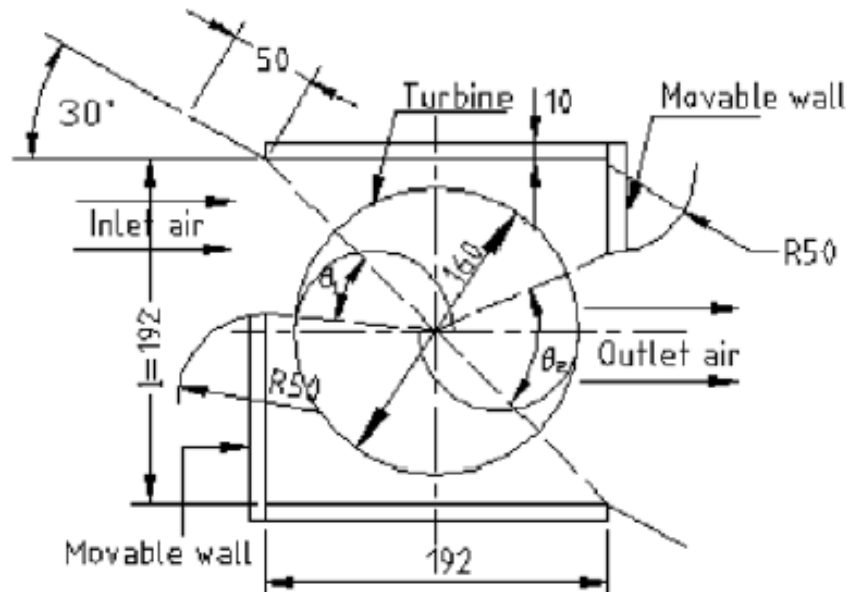


Figure 2-14: Rotor and guide box tunnel as proposed by (Irabu & Roy, 2007)

### 2.4.2 Multi-turbine interaction

(Shigetomi et al., 2011) took an interesting perspective, the authors investigated the interaction between two Savonius turbines in a nearby configuration in the horizontal plane. They found particular configurations that increased the turbines power, as an example see figure 2-15. The increase is mostly due to firstly the Magnus effect that alters the mainstream flow behind the first turbine to increase rotation in the downstream turbine. Secondly, vortex shedding and cyclic pressure fluctuation which causes periodic coupling between the Savonius turbines. Bi-coordinate system was used to present the interaction of the two turbines, and four locations were found to increase the two turbines performance above that of a single turbine. Positive effects were found firstly at,  $(x/D, y/D) = (1.5, 1.5)$ , as a result of the Magnus effect. Secondly, at  $(x/D, y/D) = (1.5, 1.5)$  due to mainstream flow bending behind the first turbine in this region. Thirdly, at  $(x/D, y/D) = (1.5, -1.5)$  this is due to the wake of the first turbine, vortex shedding, and pressure fluctuation. Fourthly, positive coupling is also observed at  $(x/D, y/D) = (0.5, -0.5)$ .

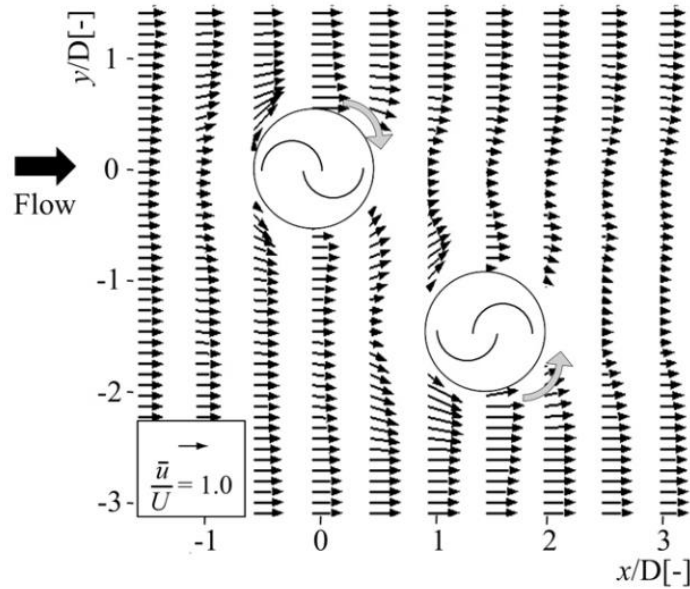


Figure 2-15: Velocity vector plot for positive interaction condition.

### 2.4.3 Stator Vanes

The stator vanes have also been used to augment the Savonius turbine, the research of (Shahizare, et al., 2016) indicated that the use of stator vanes has a positive impact on the overall turbine performance. In the study, the researchers observed that the turbine power coefficient increased with stator vanes addition. (Grönman et al., 2018) also used stator vanes to augment the 3-bladed Savonius rotor, but there was no direct comparison with the conventional 3-bladed Savonius rotor. In the study of (Grönman et al., 2018), experiments and numerical method was used to comprehensively analyze the flow within and around a stator only configuration and a stator-rotor interaction configuration. The authors' observations were that the stator has the tendencies of accelerating the flow above the free stream velocity. Also, the study presented a generic flow model for the vaned Savonius turbine as shown in figure 2-16.

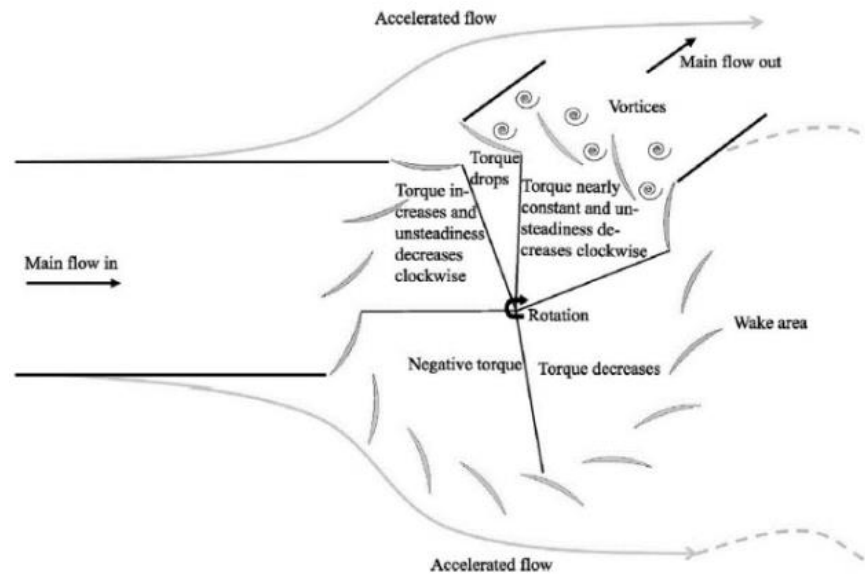


Figure 2-16: Generic flow model for the vaned Savonius turbine (Grönman et al., 2018).

Another study by (Shahizare et al., 2016) used numerical methods to investigate the effect of stator vane angles on the performance of the VAWT based on the author's previous study. The guide vanes consist of four pairs of guide vanes as shown in figure 2-16. The inference from the study was that, the optimal stator angles are when  $\beta = 55^\circ$  and  $\alpha = 20^\circ$ . At these angles the performance of the VAWT was improved by 40.9%, 36.5%, 35.3% and 33.2% at TSR of 0.745, 1.091, 1.901 and 2.53.

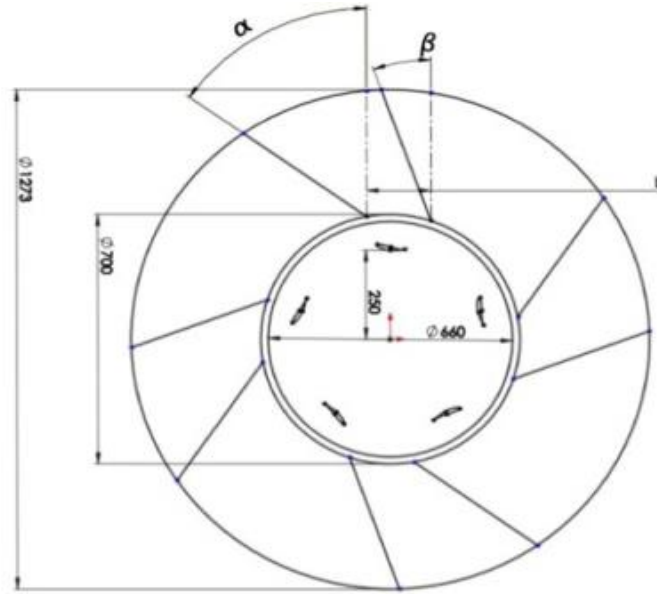


Figure 2-17. Top view of Omni-directional stator vanes (Shahizare, et al., 2016)

## 2.5 Summary

Many researchers have studied the conventional Savonius rotor to gain a full understanding of the flow phenomena that happens within and around the rotor. While others have tried to improve the overall performance of the turbine or improve a certain characteristic of the turbine like the starting torque. The historical method was to use experiments to study the Savonius rotor, but the current trend is to adopt a cost-effective numerical simulation alongside experimental validation to study the Savonius turbine. Also, turbine augmentation studies have become popular in the hopes of increasing the performance parameters of the Savonius rotor. In this thesis, stator vanes are added to the Savonius rotor, and the effect of the stator vanes on the aerodynamic properties is studied with the aid of numerical simulation.

### 3 NUMERICAL MODELLING

This chapter discusses the geometry creation, mesh generation and the numerical models used in this thesis. More so, this section also presents, to some detail, the governing equations of the fluid dynamics, turbulence models, near-wall modeling and discretization schemes. A 2D model of the Savonius rotor used in the experiment of Blackwell et al., 1977 was modified and numerically investigated in this thesis. The 2D geometry creation was made with Autodesk Fusion® 360 version 2.0.4391 student license. Autodesk Fusion® 360 present an easy but comprehensive interface for generating geometries. After the geometry creation, the next step involves the 2D mesh generation using Pointwise® mesh generation software. After which, the simulation is done by Ansys Fluent® 18.0 and the post-processing is done with CFD post.

The use of a two-dimensional geometry is acceptable because only the main flow phenomena are investigated in this thesis. Notwithstanding, the simulation results will be affected by using 2D geometry, this would generally result in the over-approximation of the turbine performance when compared to experimental data. The over-estimation occurs because the pressure profile varies with the rotor height and 2-D geometry does not capture this phenomenon. A way to mitigate against this issue would be to increase the aspect ratio of the rotor as was suggested by Grönman et al., 2018.

#### 3.1 Model description

In this thesis, part of the aim is to develop a modification, for the Savonius turbine, that increases the self-start capacity and the overall performance by using stator vanes. To the best of the author's knowledge, only a hand full of researches Grönman et al., 2018, Pope et al., 2010, and Shahizare et al., 2016 exist to this respect. The aim of using stator vanes by these researchers was to focus the upstream flow to the concave part of the Savonius turbine. The development of the stator vanes used in this thesis exploits the same ideas as was those of the above-mentioned researchers. Vividly, the modified turbine consists of the Savonius rotor and NACA 0012 stator vanes configuration as shown in figure 3-1.

The Savonius rotor in the experiment of (Blackwell et al., 1977) was improved with the addition of NACA 0012 airfoil. In its simple form, the geometry parameters of the Savonius rotor used by Blackwell, et al., 1977 are thus:



The overlap or gap ratio is 0.15, the rotor diameter is  $D_r$  is 0.9262 m, the bucket thickness  $t$  is 0.12 mm, bucket radius  $r$  is 0.5 m, the rotor height is 1 and finally an endplate with diameter with a ratio of 1.1 the rotor diameter (not shown in 2-D). From figure 3-1, the addition of six stator vanes (three upstream and three downstream) to the Savonius rotor is shown.

The stator vanes should perform two significant functions which are (1) to act as a curtain and block wind flow from getting to the convex side of the returning rotor blade and (2) to direct wind flow towards the concave side of the advancing rotor blade. The stator performs these two functions only at the rotor angular position  $90^\circ$  (shown in the figure 3-1) or  $270^\circ$  to the mainstream flow,  $U_\infty$ , because the stator vanes are static.

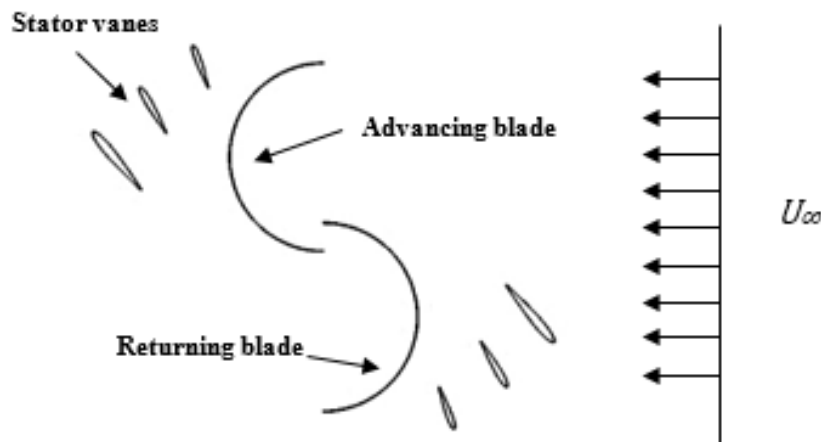


Figure 3-1: Savonius rotor with stator vanes

### 3.1.1 The stator vanes

The stator consists of 6 NACA 0012 airfoils each with different chord length, and variable angle of attack. The chord length and the angle of attack are selected based on the requirement to stop the upstream flow from getting to the convex side of the returning bucket and divert flow to the concave side of the advancing bucket respectively. The stator chord length is just enough to make sure that there is no lateral distance between the leading edge and the trailing edge of the adjacent airfoil as shown in figure 3-2, while the stator angle is selected to divert flow to the concave tip of the advancing blade.

The assumption is that blocking the direct flow towards the returning blade by the stator vanes will decrease the resistance caused by pressure buildup on the convex surface of the returning blade;

and thereby increases the pressure difference between the advancing and the returning blade which will increase the resultant drag force in the direction of the advancing blade. Table 3-1 and 3-2 show the stator vanes parameters. Finally, the downstream stator vanes, are identical to the upstream stator vanes but rotated at an angle of  $180^\circ$  about the z-axis. The downstream stator blade is used to maintain the omnidirectional property of the Savonius rotor while avoiding complicated yawing systems.

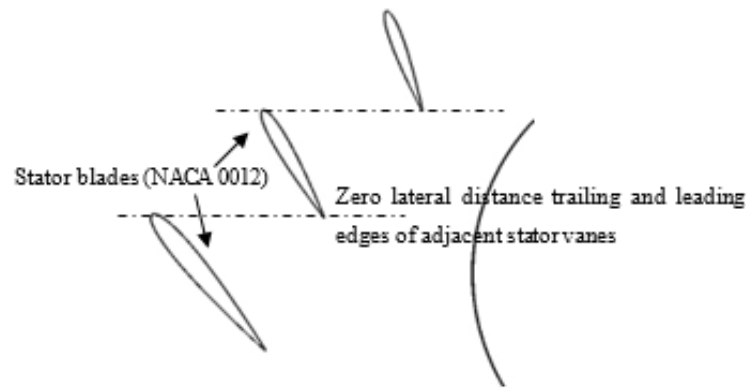


Figure 3-2: The lateral distances between two adjacent stators vanes.

Table 3-1: Stator vanes parameters

S/N	NACA type	Chord length [m]	Angle of attack
1	0012	0.20	$50^\circ$
2	0012	0.14	$60^\circ$
3	0012	0.12	$70^\circ$

Table 3-2: Stator design parameters

Stator outer radius [m]	0.675
Stator inner diameter [m]	0.5
Stator height [m]	1
Tip and hub clearance [m]	0.0389
Stator solidity	0.74

### 3.1.2 Stator solidity

Stator solidity is an important parameter to consider in this design modification. The stator solidity defined as the ratio of the blade length to the pitch is expressed mathematically as,

$$\text{stator solidity} = c/s \quad (3.1)$$

Where  $c$  is the chord length, and  $s$  is the pitch. The pitch is the ratio mean stator area to the number of blades which is

$$s = 2\pi r_m / n_b \quad (3.2)$$

Where  $n_b$  is the number of blades and  $r_m$  is the mean radius of the stator. For this stator the mean radius is

$$r_m = \sqrt{\frac{r_o^2 + r_i^2}{2}} \quad (3.3)$$

Where  $r_o$  and  $r_i$  are the stator outer and inner radius of the longest vane. The chord length  $c$  is the average chord length of the stator vanes given by

$$c = \frac{c_1 + \dots + c_{nb}}{n_b} \quad (3.4)$$

Inserting the numerical values from table 3-1 and 3-2 into equation 3.1 to 3.4 gives a solidity of 0.74. The value of the solidity correlates with the suggestion of Grönman et al., 2018. The suggestion of Grönman et al., 2018 is that the stator solidity should be in the region of 0.7.

## 3.2 Simulation procedure

This thesis required two simulation cases, the first case is the simulation of the conventional Savonius rotor (SIM1), while the second case is the simulation of the vaned configuration of the Savonius turbine (SIM2). Henceforth, the two cases are referred to as SIM1 and SIM2. Irrespective of the case, the same solver setting except for the Courant number are adopted. Adopting the same solver settings will allow both cases to be comparable to each other. The discretization of the transport equation was with the second-order upwind scheme in these simulations, but in order to avoid instability in the simulations, the solution was first initialized using a steady state flow with a moving reference flow around the turbine to get the initial guess for the transport variables. Then

the unsteady state simulations started with a first-order differencing scheme in both space and time for one rotation, before switching to the second-order scheme for the remaining rotations.

The turbulence model used by the solver was the  $k-\omega$  shear-stress transport (SST) as suggested by Balduzzi et al., 2016, the advantage of using the  $k-\omega$  SST model is that it combines the precise near wall formulation of the standard  $k-\omega$  with the free-stream formulation of the  $k-\epsilon$  model.

The following cell zones and boundary conditions are defined in the calculated domain and are presented in figure 3-4:

- A rectangular outer zone with a length of  $45 D$  and a height of  $20 D$ .
- A circular rotating mesh zone with a diameter 1.04 times the diameter of the rotor. The size of this zone is smaller than seen in the literature (Kacprzak et al., 2013), this is to reduce the clearance between the stator vanes and the rotor buckets.
- The wall boundary condition was used in the interface between the rotating domain and the far-field domain.
- The velocity inlet with a value of 7 m/s.
- The pressure outlet has a pressure of 1 atm.
- Finally, the upper and the lower wall of the far-field zone is symmetry condition.

### 3.2.1 Solver settings

This section presents the settings used for the Ansys Fluent® solver. First, the common settings between the SIM1 and SIM2 are discussed. After which, the discussion is focused on the different Courant numbers used in both simulations. In general, each simulation considered six design points. The tip to speed ratio forms the bases of each design point, each design point is assigned a TSR. In this thesis, TSR 0.4, 0.5, 0.6, 0.7, 0.8, and 0.9 are investigated by numerical methods for both the conventional and modified Savonius turbine.

Low Mach number is a characteristic of the flow within and around a Savonius turbine as such the flow is considered incompressible, therefore the pressure-based solver is used for both SIM1 and SIM2. In this approach, the continuity equation and the momentum equation are used to derive the

equation required to solve for the pressure field (Balduzzi et al., 2016). Also, both cases use the absolute velocity formulation as the size of the rotating zone is relatively small when compared to the calculation domain extent.

The next setting concerns the choice of the algorithm used to solve the pressure-velocity coupling; it is common in literature to utilize either the SIMPLE or the *Coupled* algorithm in VAWT simulations. Both solution algorithms are iterative; this is because the governing equations are non-linear and coupled, as such the solution loop must be solved until achieving a converged solution. The major difference between the two algorithms is the rate of convergence and the memory requirements. The SIMPLE algorithm requires less memory but has a slow rate of convergence. While the *Coupled* algorithm requires a memory increase of about 1.5 – 2 times of the SIMPLE algorithm, but the convergence rate is faster (Fluent Inc., 2001). Also, the *Coupled* algorithm solves the momentum and the derived pressure-based equation together, resulting in a robust and efficient solution for transient flow. Therefore, in both simulations, the *Coupled* algorithm is used to solve the pressure-velocity coupling problems. Each iteration of the coupled algorithm consists of the steps illustrated in figure 3-3.

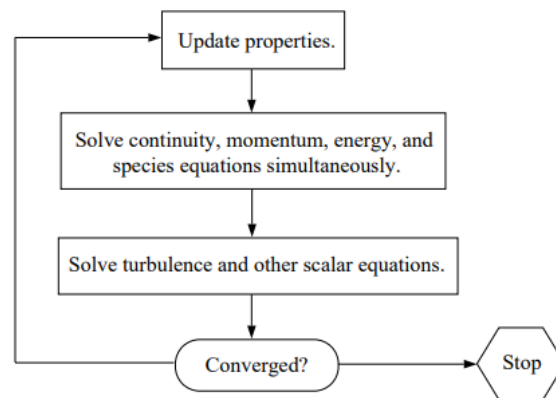


Figure 3-3: Overview of Pressure-Based Coupled Algorithm (Fluent Inc., 2001)

The angular timestep is the same for both simulations. An angular timestep of  $1^\circ$  was suitable to achieve a stable and converged solution. The timestep of  $1^\circ$  is common with the simulation of Savonius rotor (Lee et al., 2016), (Zhang et al., 2017). Focusing on the Courant-Friedrichs-Lewy (CFL) criterion that defines a Courant number,  $C_o$  as the dimensionless number representing the

ratio between the temporal timestep ( $\Delta t$ ) and the cell size ( $\Delta x$ ) multiplied by the convective flow velocity ( $V$ ).

$$C_o = V \frac{\Delta t}{\Delta x} \quad (3.9)$$

The Courant number of 1 is also common with the simulation of the Savonius turbine and is used in SIM1. However, for SIM2, the interaction of the upstream stator vanes with the main flow will result in an increase of the flow velocity within the Savonius rotor. Hence, a reduction in Courant number was required to maintain the convergence of the simulation results. Furthermore, a variable Courant number was used for SIM2, at low TSR the  $C_o$  was 0.5 and at higher TSR the  $C_o$  was 0.25.

### 3.2.2 Modeling turbulence

In Fluent<sup>®</sup> turbulence modeling is done with the robust and accurate  $k-\omega$  SST model developed by (Menter, 1994). The major difference between the standard and the SST  $k-\omega$  are that firstly, the SST model is an addition of the standard  $k-\omega$  and the  $k-\epsilon$  model multiplied by a blending factor. This blending factor has a value of 1 near the surface, which activates the  $k-\omega$  model, and 0 away from the wall which activates the  $k-\epsilon$  model. Secondly, the turbulent viscosity formulation is modified taking the effect of turbulent shear stress into consideration, hence the name  $k-\omega$  SST. These differences make the  $k-\omega$  SST model dependable over a range of wider kind of flows than the standard  $k-\omega$  model (Fluent Inc., 2001).

See Appendix I for the mathematical formulation of the SST  $k-\omega$  algorithm.

## 3.3 Mesh generation

A high-quality mesh is required if the aim is to mitigate instability and get converged solutions. For this reason, Pointwise<sup>®</sup> V18 is used to generate the calculating mesh. Pointwise is a dedicated mesh generation and pre-processing software for CFD simulation (Pointwise, 2018). The process of creating an adequate mesh to resolve the problem properly involves firstly, the construction of a computational domain large enough so that the domain does not influence the flow field. Secondly, the creation of adequate density meshes to capture the flow phenomena.

Figure 3-4 presents the extent of the computational domain; the length of the upstream and downstream domain is 15 times and 30 times the diameter of the rotor respectively. While the

height of the domain is 20 times the diameter of the rotor, this domain extent is large enough to avoid the blockage effect of the lateral boundaries following the suggestion of Balduzzi et al., 2016. The calculation domain consists of two parts which are the rotating domain and the far-field. The diameter of the rotating domain is 1.04 the diameter of the rotor, in order to reduce the needed computational requirement and reduce the clearance between the stator vanes and the rotor. The rotating and the far-field domains are made up of mixed mesh containing both triangular, and quadrilateral cells (see figure 3-7).

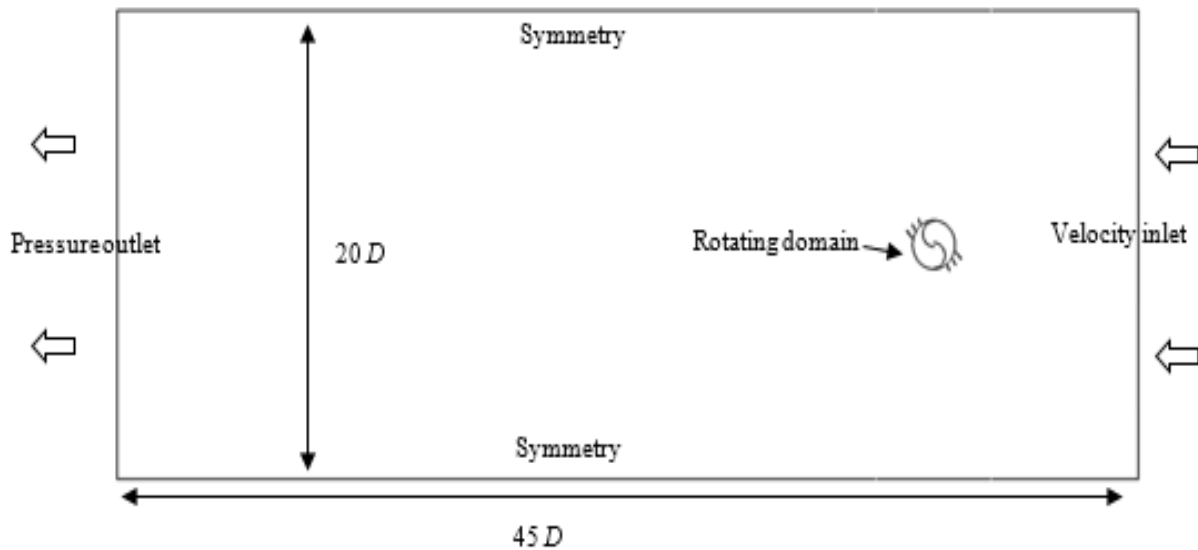


Figure 3-4: Extent of the computational domain

### 3.3.1 Spatial discretization

This section examines the density of mesh required to adequately solve the discretized Unsteady Reynolds Average Navier Stokes equations (URANS). It is required that a fine mesh is used to capture the gradient of the flow (Balduzzi et al., 2016), but due to solver license (Ansys Student) cell size limitations, the maximum number of cells cannot exceed 512000 cells. Therefore, an attempt is made to discretize the calculation domain to mitigate against solution instability and still be within the limits of the student license. The discretization will require selective order of resolution for different part of the computational domain. In this case, the near wall region (that is the rotor bucket and the stator vanes) have the highest resolution, see figure 3-5. The black region near the wall indicates high mesh density.

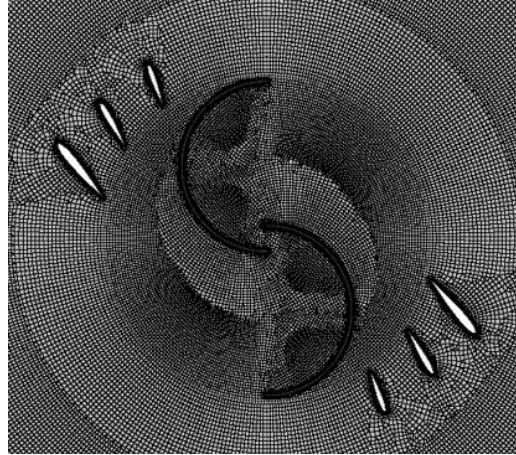


Figure 3-5: Selective mesh resolution of the computational domain. The rotor buckets and the stator vanes having the highest resolutions.

### 3.3.2 Boundary layers modeling

The near wall region of the calculation mesh is very important, and as such care was taken to mesh this region adequately. In the near wall region structured (quadrilateral cells) mesh was utilized to resolve the boundary layer profile ( $y^+$ ). The number of discretization nodes on the rotor bucket and the stator vanes profiles is crucial to resolving the incoming flow incidence angle on the bucket or stator vanes surface. For the rotor bucket, the nodes are densely distributed at the tips, while for the stator vanes the node points are densely distributed at the leading and the trailing edges.

The mesh in the region of the wall boundary is constructed with the aim of making the dimensionless wall distance,  $y^+$ , below 1 to avoid discontinuity (Balduzzi et al., 2016). The true  $y^+$  is not known a priori to the simulation. Therefore the  $y^+$  value used in the meshing stage was approximated using the law of the wall. The law of the wall is an empirical relationship in turbulent flows near solid boundaries. The law states that the velocity in the flow near the wall varies with the logarithmic distance from the wall (Wilcox, 2006). Figure 3-6 shows the graphical representation of the law of the wall, also the distance from the wall is approximated using the formula

$$y^+ \equiv \frac{y^+ v}{u_\tau} \quad (3.5)$$

Where the kinematic viscosity,  $\nu$ , is the ratio of the molecular viscosity  $\mu$ , and density  $\rho$ ,  $\nu = \mu/\rho$ , and  $u_\tau$  is the friction velocity defined as



$$u_\tau \equiv \sqrt{\frac{\tau_w}{\rho}} \quad (3.6)$$

Where  $\tau_w$  is the surface shear stress and given by

$$\tau_w = c_f \times \frac{1}{2} \rho U_\infty^2 \quad (3.7)$$

Where  $c_f$  is the skin friction and  $U_\infty$  is the freestream velocity. The skin friction is approximated using the Schlichting-Gersten correlation given by

$$\frac{1}{\sqrt{c_f}} = 4 \log_{10}(2 Re_D \sqrt{c_f}) - 1.6 \quad (3.8)$$

$Re_D$  is the Reynolds number and is a function of the average velocity across the surface and the surface diameter.

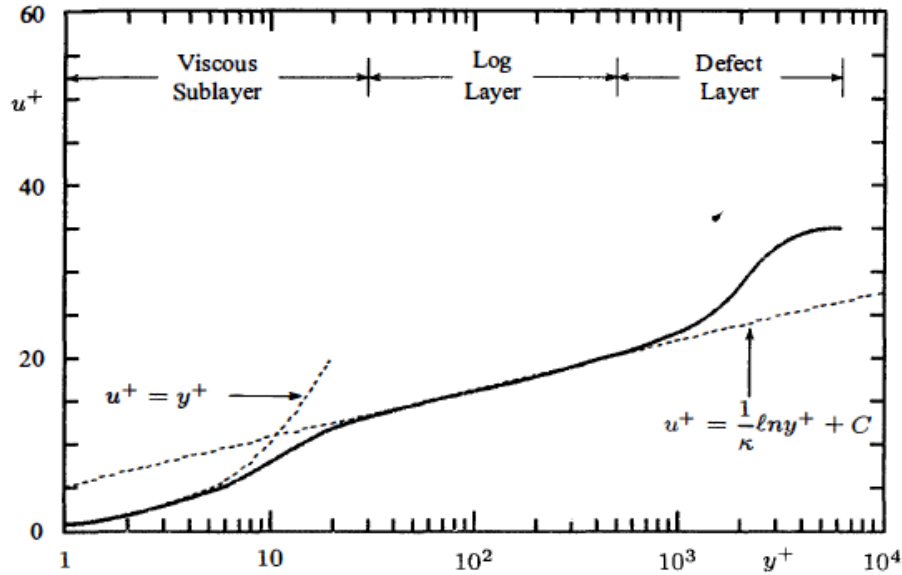


Figure 3-6: Velocity profile for a turbulent boundary layer (Wilcox, 2006).

Therefore, to maintain the  $y^+$  value below 1, the near boundary layer region has ten layers of the structured grid with a growth rate of 1.1, and the first cell from the wall has a height of  $2e-5$  m. Table 3-3 presents the flow and geometry parameters used for calculating the first cell height from the wall. Also, each rotor bucket is discretized with 3235 nodes, while the three stator vanes have 840 nodes, 590 nodes, and 507 nodes respectively from the longest to the shortest airfoil.

Table 3-3: Flow and geometry parameters for calculating first cell height from the wall.

Main velocity	7 m/s
Density	1.225 kg/m <sup>3</sup>
Dynamic viscosity	1.7894e-5 kg/ms
Turbine diameter	0.9262 m
Reynolds number	440 000
Desired y+	0.5

In pointwise, the immediate boundary layer mesh was created in the following order:

- i. Connectors profiles were generated from the geometry database using the *Entity on Database* command.
- ii. The connectors profiling the rotor buckets were discretized using the *Dimension (ctrl+W)* command under the *Grid* option on the toolbar.
- iii. The generated node points are distributed accordingly; to the tips for the rotor buckets, and to the leading and trailing edges for the stator vanes. The distribution is done with the *Distribute (ctrl+G)* command under the *Grid* option on the toolbar.
- iv. Finally, the rotor buckets and the stator vanes immediate mesh are generated using the *Normal Extrusion* command under the *Create* option on the toolbar.

### 3.3.3 Grid dependency study

To evaluate the impact of the grid extent and density, three grids are constructed for both the vaned and the vaneless turbine and simulated with a flow velocity of 7m/s which corresponds to the velocity used by Blackwell, et al., 1977. Tables 3-3 and 3-4 present the properties of the studied meshes, the main variables used in regulating the final grid is the number of node points on the rotor and the stator buckets, and the domain size. An example is figure 3-7 showing the details of the near wall resolution of the M3 mesh, (A) is showing the rotor bucket and the advancing stator vanes, (B) the stator vane and (C) the tip of the rotor bucket.

Table 3-4: Mesh sensitivity analysis for the vaned configuration.

Reference name	Type	Number of nodes on the rotor buckets	Number of nodes on the stator vanes	Total cells count	Domain size
M1	Coarse	1661	263, 304 and 432	181,728	$22.5D \times 10D$
M2	Normal	1661	263, 304 and 432	251,388	$30D \times 15D$
M3	Fine	3,235	507, 590 and 840	508,141	$45D \times 20D$

Table 3-5: Mesh sensitivity analysis for the vaneless configuration.

Reference name	Type	Number of nodes on the rotor buckets	Total cells count	Domain size
G1	Coarse	1661	151,825	$22.5D \times 10D$
G2	Normal	1661	221,501	$30D \times 15D$
G3	Fine	3,235	448 410	$45D \times 20D$

The impact of the meshes was evaluated using the average torque coefficient value at  $TSR = 0.5$  (see figure 3-7). The results show that the coarse meshes (M1 and G1) and the normal meshes (M2 and G2) overestimated the torque coefficient when compared to the fine meshes. The fine meshes (G3 and M3) generated could no longer be improved as it was a few cells count below the Ansys student limit of 512,000. Therefore, the simulation of the vaned and the vaneless configuration uses the fine meshes (M3 and G3) respectively. To prove the suitability of the fine mesh, a validation, and a convergence study is carried out in the next section, to evaluate the mesh and the solver setting performance.

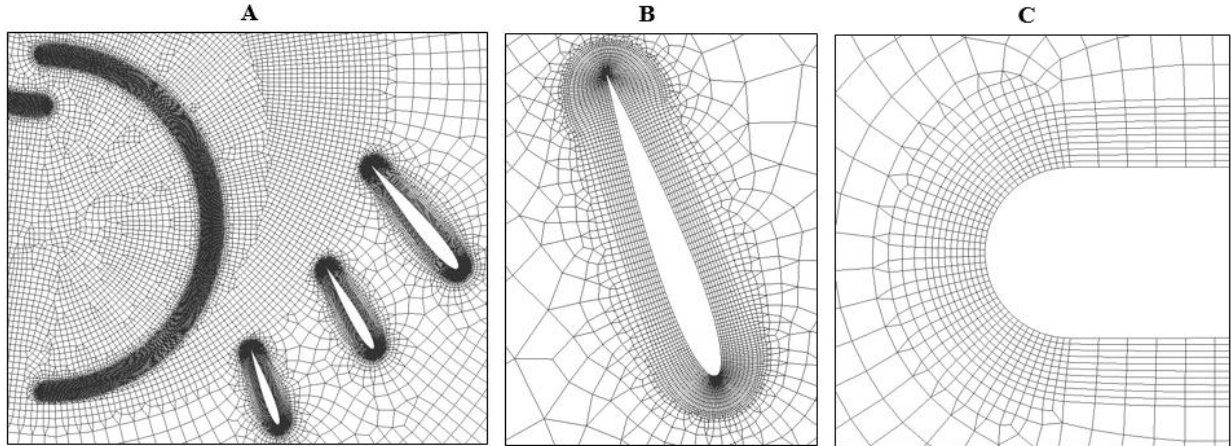


Figure 3-7: M3 mesh details.

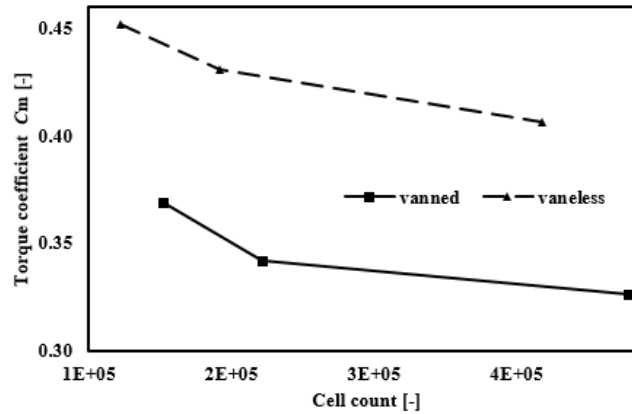


Figure 3-8: Grid sensitivity analysis at TSR = 0.5.

### 3.3.4 Convergence criteria and validation

The convergence criteria of the Savonius turbine, as common with different researches occurs when the performance parameters show a periodic behavior with a difference of less than 1%. Figure 3-9 shows that for TSR of 0.6, the vaneless configuration attained periodic behavior at flow time of 3 seconds. Figure 3-10 shows the percentage difference of the last two rotations for both the vanned and the vaneless configuration. The maximum difference for the vanned configuration was at TSR of 0.4 with a magnitude of 6%, while for the vaneless configuration the maximum difference was 4% at TSR of 0.4. This increase in the percentage difference was affected by the number of rotations per simulation. In this thesis, the maximum rotation for the simulations is 6.

But to achieve a difference of less than 1% it is common to use 10 rotations per simulation as was used by Grönman, et al., 2018.

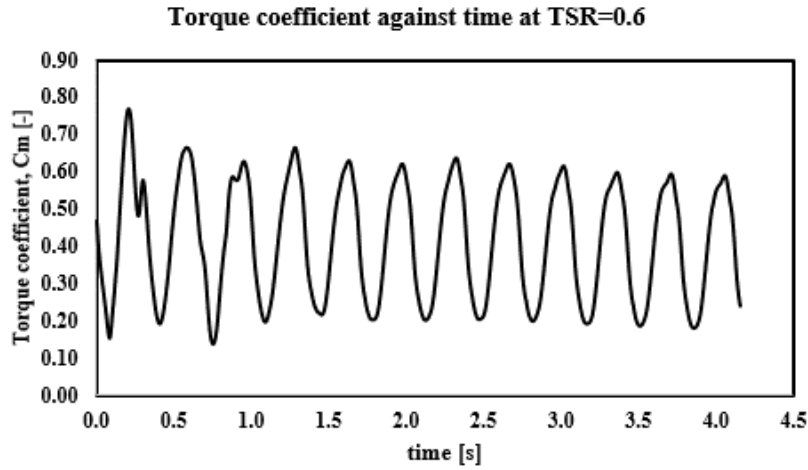


Figure 3-9: Convergence criteria

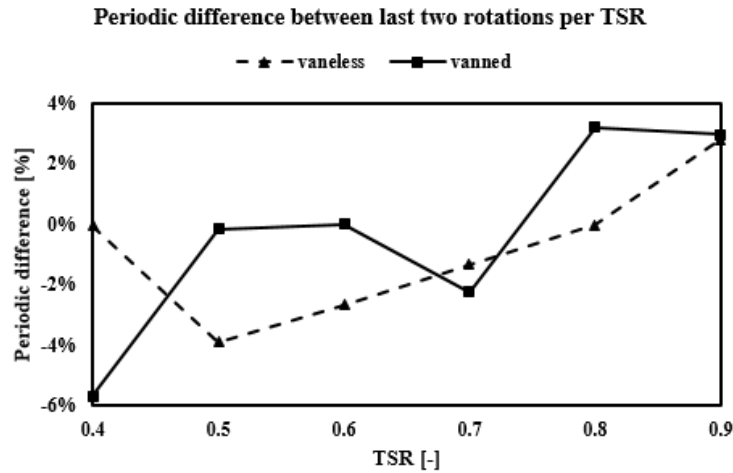


Figure 3-10: Percentage difference between the last two rotations per TSR.

The validation process for the vaneless configuration involves the comparison of the simulation results from the G3 mesh, with the experimental data of Blackwell et al., 1977. For validating the simulation of Savonius rotor three dimensionless parameters are regularly considered,

The tip speed ratio TSR is defined as

$$TSR = \frac{\omega R}{U_{\infty}} \quad (3.10)$$

While the torque coefficient is defined as

$$C_m = \frac{T}{0.5\rho ARU_\infty^2} \quad (3.11)$$

And the power coefficient is defined as

$$C_p = \frac{T\omega}{0.5\rho AU_\infty^3} = C_m \times TSR \quad (3.12)$$

Where  $\omega$  is the turbine angular speed,  $R$  is the rotor radius,  $\rho$  is the density and  $A$  is the swept area of the rotor.

Figure 3-11 shows the comparison between the simulated results and the experimental data, the dashed line represents the experimental data of Blackwell et al., 1977, while the solid line is the simulation result. Plot (A) shows the torque coefficient as a function of TSR while (B) shows the power coefficient as a function of TSR. The figure shows that there is a good matching between the simulation results and the experimental data for all TSR; with the optimal TSR in the range of 0.8 – 0.9 in both cases. However, slight differences are noticed in the magnitude of the performance parameters of the simulation results. The increase is because of the use of 2D geometry as earlier pointed out in section 3.1. More important is that the simulation results follow the same trend as the experimental data.

Due to the novel nature of the vaned turbine, no experimental data are available for validation.

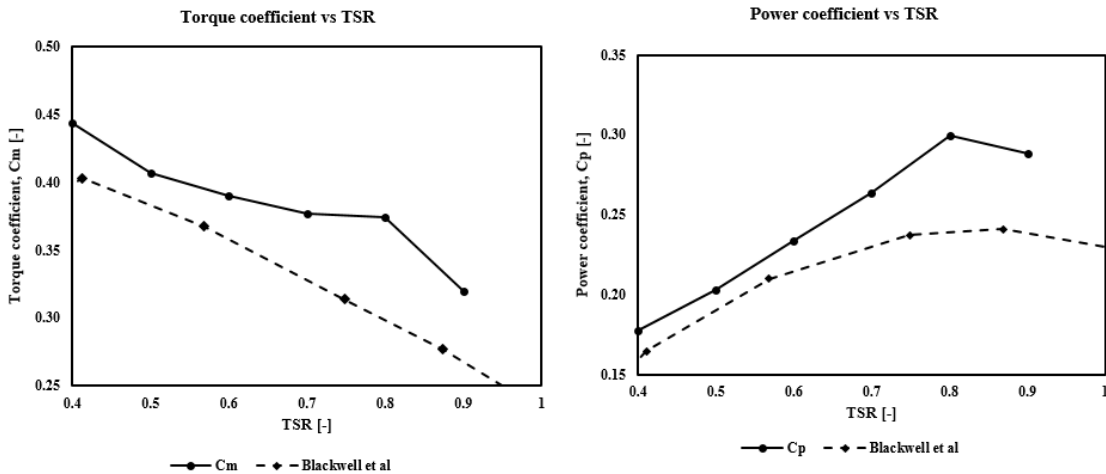


Figure 3-11: Validation for the conventional Savonius rotor

### 3.4 Summary

In summary two cases SIM1 and SIM2 were simulated in this thesis with the following settings and boundary conditions as presented in table 3-6.

Table 3-6: Elaborate solver settings for simulated cases.

Description	Settings
Simulation type	Transient
Velocity formulation	Absolute
Solver type	Pressure-based
Turbulence model	$k-\omega$ SST
<b>Cell zone motion</b>	
Rotating domain	Sliding mesh motion
Far-field domain	No motion
<b>Boundary conditions</b>	
Inlet boundary condition	Velocity inlet
Outlet boundary condition	Pressure outlet
Rotor boundary condition	Moving wall, rotational, with no slip
Stator boundary condition	Moving wall, rotational, with no slip
Mesh interface condition	Moving wall, rotational, with no slip
<b>Solution methods</b>	
Pressure-velocity scheme	Coupled
Momentum discretization	Second order upwind
Gradient discretization	Least Square Cell based
Transient formulation	Second-order implicit
Angular time-step	1°
Time-step method	Fixed
Iteration per time-step	30
Courant number	1 (for SIM1) and, 0.5 for TSR 0.4 – 0.7 and 0.25 for TSR 0.8 – 0.9 (for SIM2)

## 4 RESULTS AND DISCUSSION

This section will try to make sense of the significant amount of data generated by using CFD simulation, and present the results in a simple, meaningful and easy to understand manner. The first part of this chapter presents the transient simulation results in the forms of charts showing the average performance parameters for the design points investigated in this thesis. Transient simulation meaning that during the simulation the rotor was rotated along the z-axis in the direction of the flow as shown in figure 4-1. The average torque coefficient and the average coefficient of power is presented for both the vaned and the vaneless turbine configurations (see figure 4-2). After which the torque coefficient is presented for all design points for rotor angle ranging from  $-90^\circ$  to  $270^\circ$  (see figure 4-3 to 4-8). The other half of this section will try to analyze the generated result plots and contours plots to fully understand the impact of the NACA 0012 airfoil on the turbine performance.

More so, visual analysis is made by comparing the flow parameters contour plots of the vaneless and the vaned configurations at rotor angles of interest at selected TSR. Finally, because of the voluminous quantity, the contour plots showing the flow within and around the vaned Savonius turbines are presented in the Appendix II section of this thesis

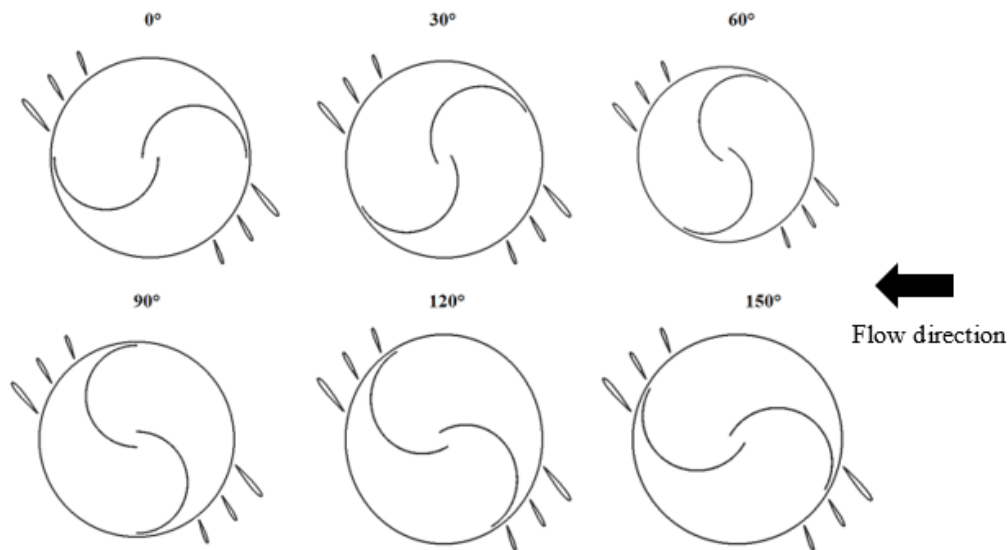


Figure 4-1: Rotor angular positions for one complete rotation during transient simulation.



## 4.1 Performance parameters

Focusing our attention on the average performance parameters over the range of design points. The results displayed in figure 4-2 presents (A) the average torque coefficient as a function of TSR, and (B) the average power coefficient as a function of TSR. One observation that is easy to notice in these figures is that the vaneless Savonius rotor outperforms the vaned turbine when considering both the torque coefficient and the power coefficient. Taking a closer look at the average torque coefficient chart (figure 4-2A), both the vaneless and the vaned Savonius turbine have the maximum torque coefficient when the tip speed ratio is 0.4 and follows the same trend. Although, the vaned turbine has a step-like behavior; with an almost constant average torque coefficient at a TSR of 0.4 to 0.7 before decreasing at TSR of 0.8 and remaining almost constant at TSR of 0.9. More so, for the power coefficient curve, the optimum TSR of the vaneless turbine is at 0.8, but for the vaned turbine the optimum TSR is outside the limit of the simulated design points. On the average, the vaneless Savonius rotor outperforms the vaned configuration by 20%.

Turning our attention to the starting capacity performance, as one of the initial aims of adding the vanes to the Savonius turbine was to improve the starting torque. Figures 4-3 to 4-8 presents the torque coefficient of the vaned (solid line) and the vaneless (dashed line) configurations as a function of the rotor angle of attack for one complete rotation ranging from  $-90^\circ$  to  $270^\circ$ . In this simulation the main flow direction is towards the negative x-axis and therefore the rotor bucket is rotated counterclockwise. Thus, the range of angles of the rotor indicates that at the starting position of the simulation; the rotor bucket is normal to the flow and rotates counterclockwise. The first chart, **A**, presents the rotor buckets torque coefficient, while the second chart, **B**, and the third chart, **C**, displays the torque coefficient for the advancing bucket and the returning bucket respectively. The observation from figures 4-3 to 4-8 regarding the starting torque is that the vaneless Savonius turbine has positive static torque coefficient on all simulated tip to speed ratio and can self-start at all rotor angular position. This agrees with the observation of Blackwell, et al., 1977. On the other hand, the vaned Savonius turbine has negative static torque coefficient when operating at TSR of 0.5 and 0.7. Also, for the vaned turbine, the static torque coefficient has very low minimum values for the other TSR. This indicates that the addition of the stator vanes as was implemented in this thesis diminishes the starting capacity of the Savonius turbine.

In one sentence, it can be said that the inclusion of stator vanes as was implemented in this thesis has a negative effect on the overall Savonius rotor performance. The latter part of this chapter is devoted to elucidating how the NACA 0012 airfoil reduces the performance of the Savonius rotor and if at all it has any positive contribution to the overall Savonius rotor performance.

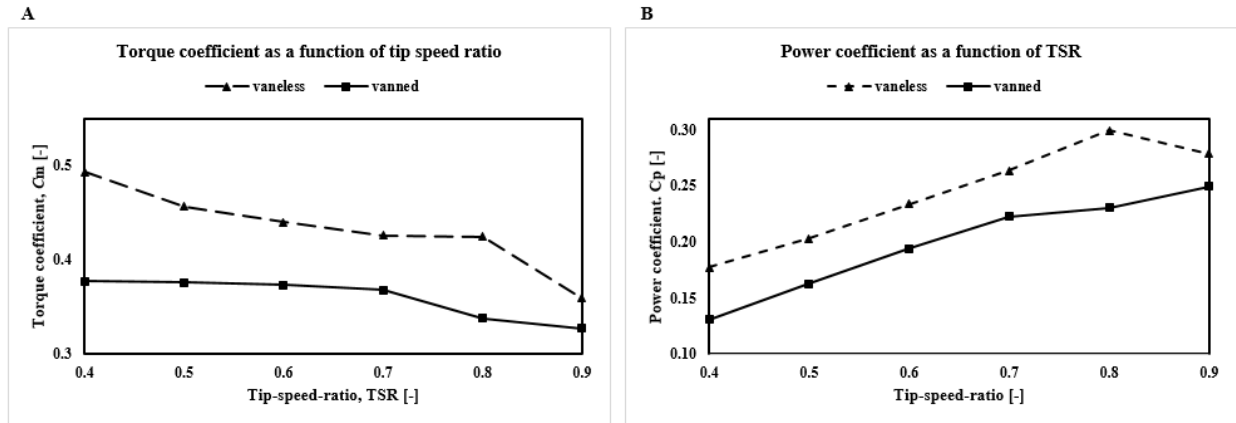


Figure 4-2: Performance parameters as a function of the tip speed ratio. (A) Torque coefficient (B) Power coefficient

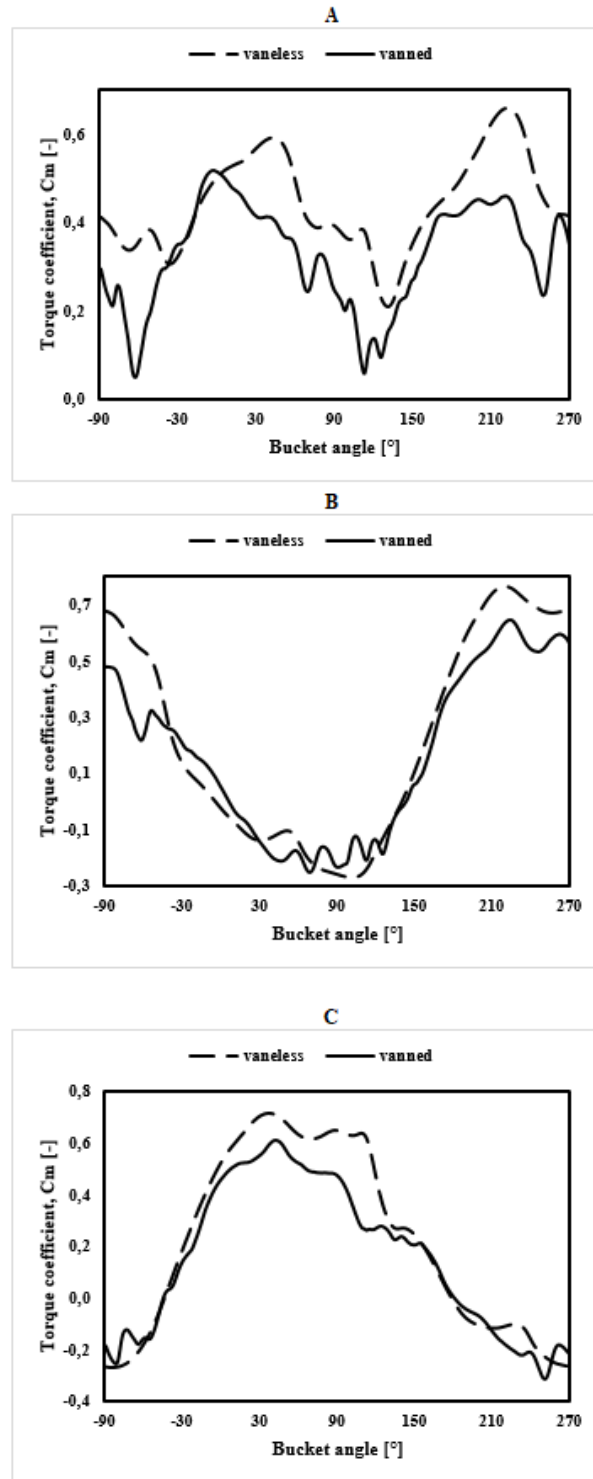


Figure 4-3: Torque coefficient as a function of bucket angle at  $TSR = 0.4$ . (A) Torque coefficient for the rotor (B) Torque coefficient for the advancing bucket and, (C) Torque coefficient for the returning bucket

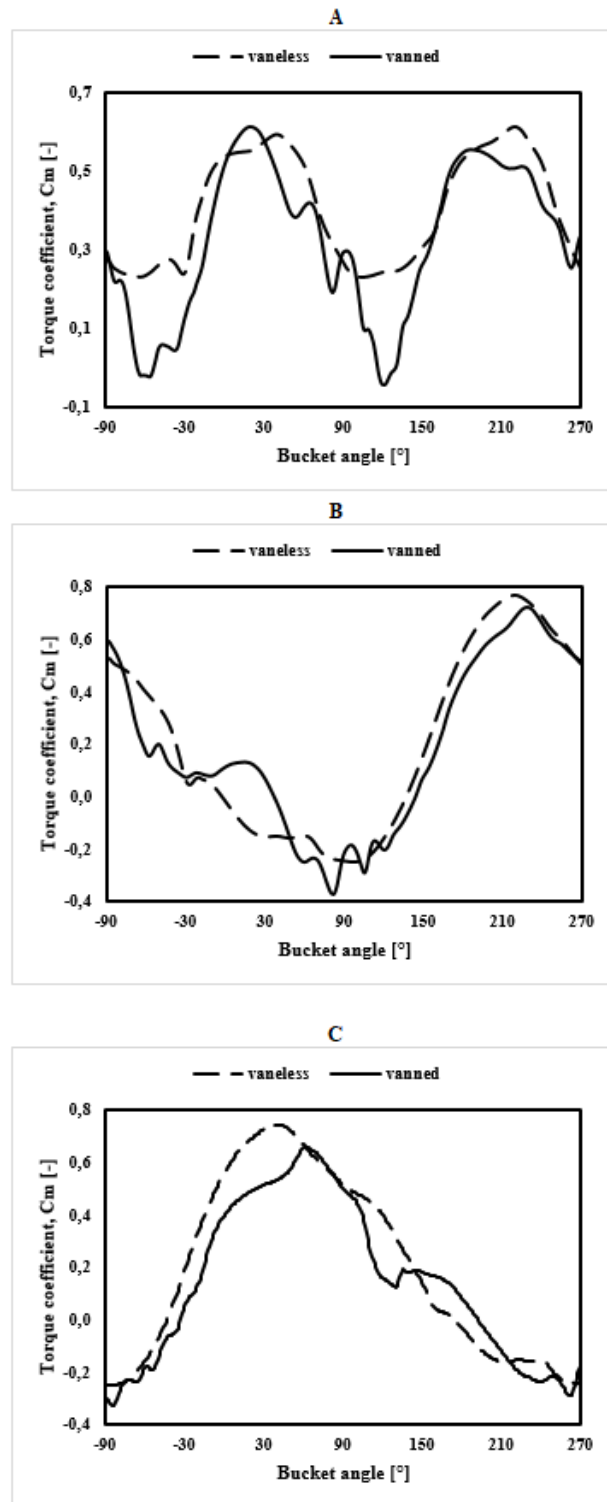


Figure 4-4: Torque coefficient as a function of bucket angle at TSR = 0.5. (A) Torque coefficient for the rotor (B) Torque coefficient for the advancing bucket and, (C) Torque coefficient for the returning bucket

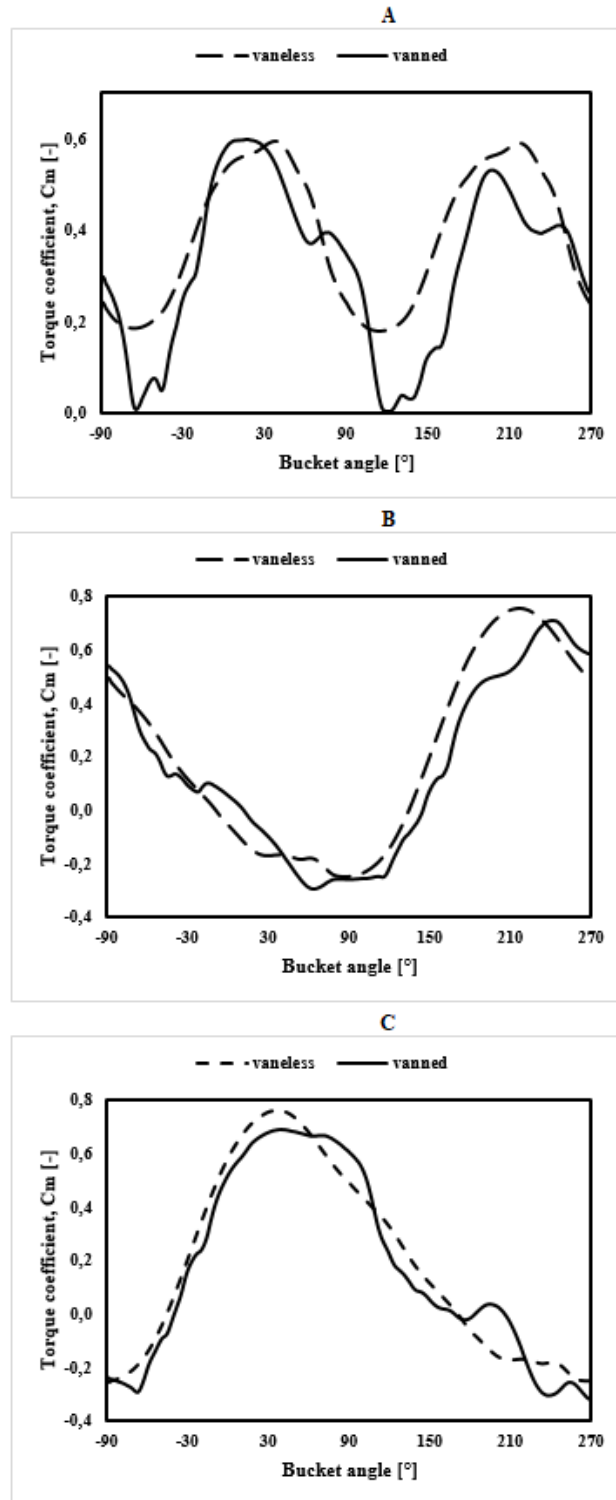


Figure 4-5: Torque coefficient as a function of bucket angle at TSR = 0.6. (A) Torque coefficient for the rotor (B) Torque coefficient for the advancing bucket and, (C) Torque coefficient for the returning bucket

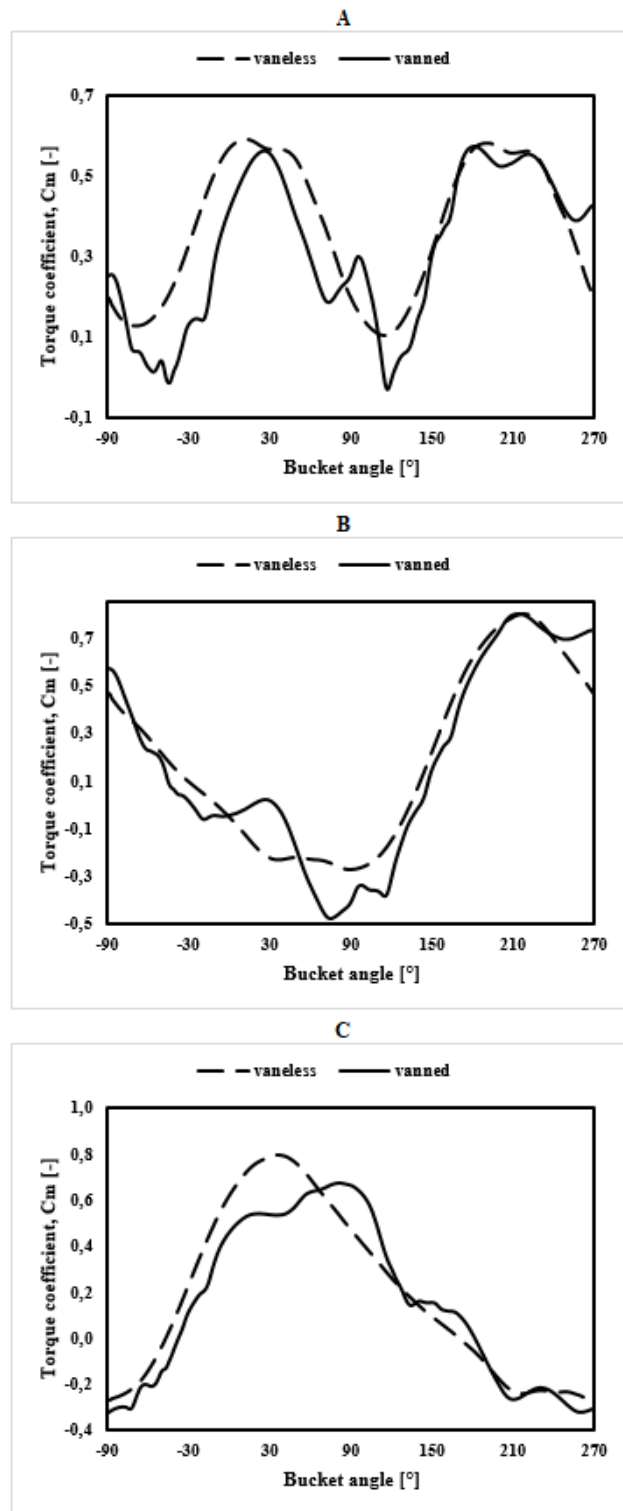


Figure 4-6: Torque coefficient as a function of bucket angle at  $TSR = 0.7$ . (A) Torque coefficient for the rotor (B) Torque coefficient for the advancing bucket and, (C) Torque coefficient for the returning bucket

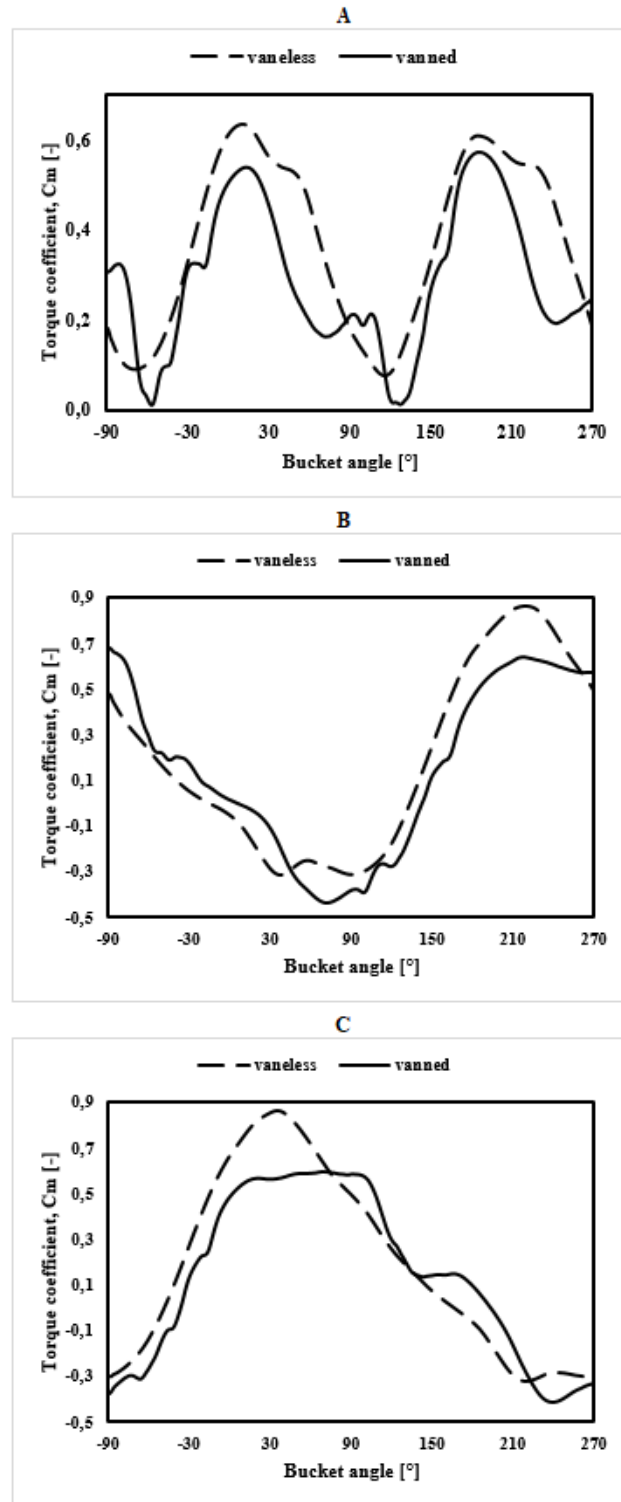


Figure 4-7: Torque coefficient as a function of bucket angle at TSR = 0.8. (A) Torque coefficient for the rotor (B) Torque coefficient for the advancing bucket and, (C) Torque coefficient for the returning bucket

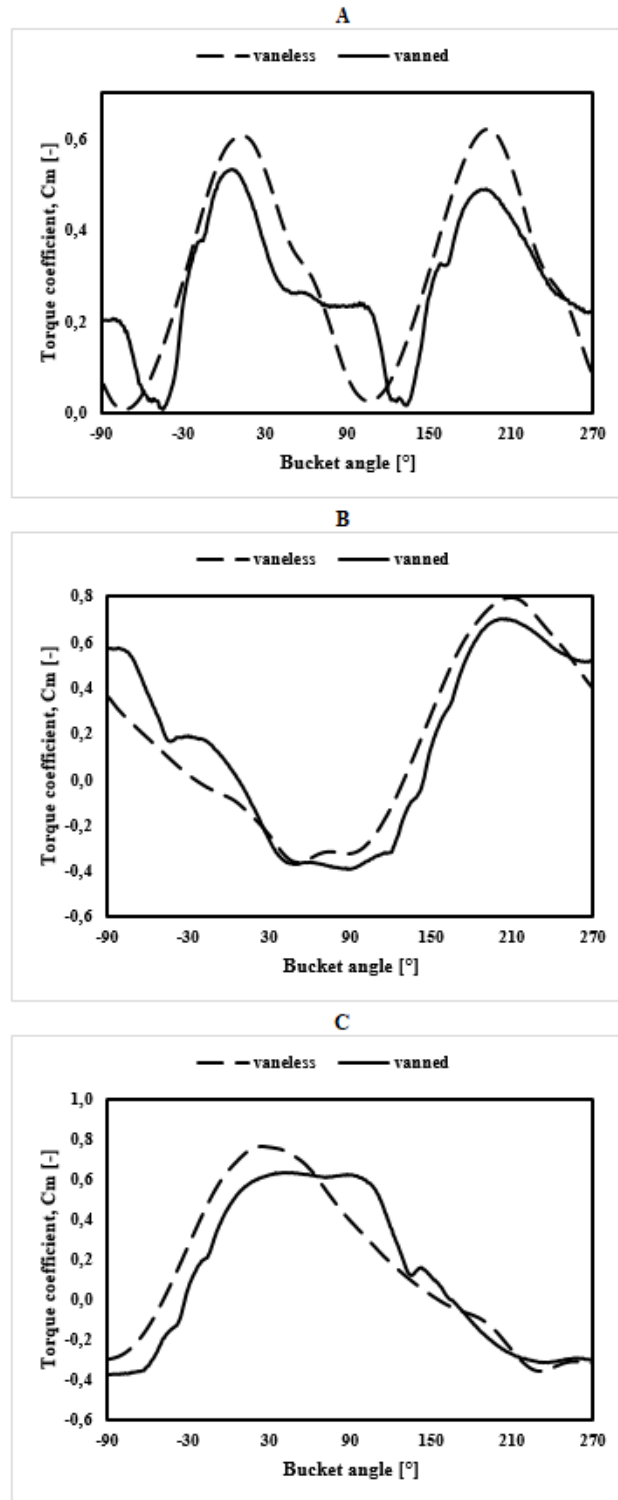


Figure 4-8: Torque coefficient as a function of bucket angle at TSR = 0.9. (A) Torque coefficient for the rotor (B) Torque coefficient for the advancing bucket and, (C) Torque coefficient for the returning bucket



## 4.2 Effect of stator vanes

On the topic of the influence of the stator vanes on the performance parameters; the observation from the former part of this chapter was that the stator vanes have undesirable impacts on the performance parameters. Therefore, this section is focused on giving a robust analysis of the interaction between the stator vanes, the rotor vanes and the flow field around and within the Savonius turbine; to elucidate why the addition of the stator vanes results to a negative overall Savonius rotor performance. Additionally, design point 2 and 6 corresponding to the turbine with a tip speed ratio of 0.5 and 0.9, is used for the solution analysis. The choice of using design point 2 was affected by the fact that different phenomenon affects the Savonius turbine at a lower speed while design point 6 is used to simulate phenomenon common to all design points, as it has the best operating design point for the vaned configuration examined in this thesis. Besides, the convergence and the accuracy of simulation at these design points are very good and the difference between the last two rotations is less than 3% as shown in figure 3-9.

The turbine parameters are affected differently by the upstream and the downstream stator vanes depending on the rotor buckets angle. It is easily observed from the torque coefficient figures 4-3 (B and C) to 4-8 (B and C), that firstly, for the advancing bucket, the torque coefficient of the vaned turbine is higher than that of the conventional Savonius rotor at certain rotor angles between  $-90^\circ$  to  $30^\circ$  for all design points (see figure 4-1 for rotor positions). For the returning bucket, this corresponds to a bucket angle in the range of  $90^\circ$  to  $210^\circ$ . Secondly, torque coefficient for the vaned turbine is lower than that of the vaneless configuration in the advancing bucket at bucket angles of attack ranging from  $30^\circ$  to  $210^\circ$  which corresponds to bucket angles of  $-90^\circ$  to  $90^\circ$  on the returning bucket. The gain in the advancing bucket occurs simultaneously with the loss in the returning bucket. Therefore, the total torque coefficient at any instance is a sum of the torque coefficient of the advancing and the returning buckets at that instance.

In order to explain the improved and inferior torque performance of the vaned turbine; a control line A, with one hundred control points (1 – 100) is drawn in front of the downstream vanes and behind the rotor buckets as shown in figure 4-9 (left). Also, a control line, B, with one hundred points (1 – 100) is drawn behind the upstream stator vanes and in front of the rotor buckets as shown in figure 4-9 (right). The analysis procedure involves changing the angle of attack of the rotor buckets and extracting flow properties along these control lines. After which pressure and,

velocity profile along these control line with the contour plots is used to explain the observed flow behavior as related to the turbine performance. Finally, control line **A** sectioning the advancing bucket will be used to analyze the improved torque performance, while the control line **B** sectioning the returning blade is used to analyze the inferior torque performance of the vaned Savonius turbine.

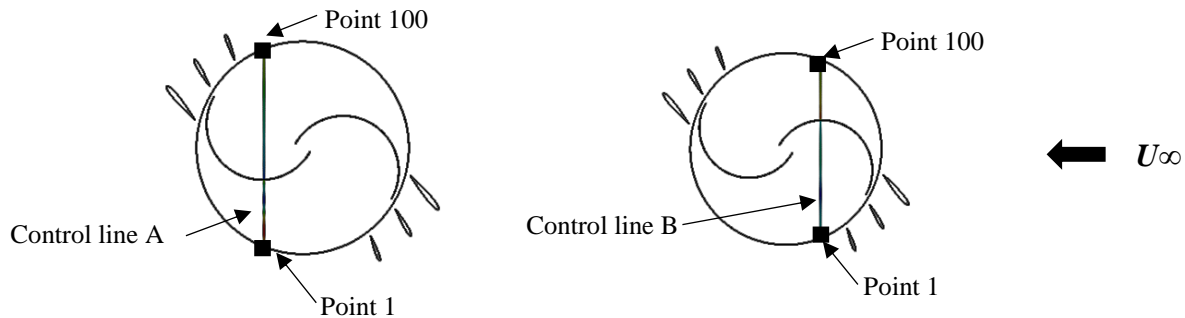


Figure 4-9: Control lines A and B for measuring flow parameters.

#### 4.2.1 Improved torque performance analysis

Although the overall performance of the vaned turbine is inferior when compared to the vaneless rotor. But there are rotor angles when a single bucket or the combine rotor buckets of the vaned turbine outperforms the vaneless turbine. The improved torque performance of the vaned Savonius turbine at these rotor angles is investigated in this section, with the hopes of replicating it across all rotor angles. The advancing bucket gain on the torque coefficient for the vaned turbine was observed when the rotor angle of attack was  $-90^\circ$  to  $30^\circ$  across all tip speed ratios. These angles correspond to positions, where the advancing bucket is the vicinity of the downstream vanes.

Regarding all the investigated tip speed ratio in this thesis, the phenomenon responsible for improved advancing bucket performance of the vaned turbine is the extended flow attachment on the convex side of the bucket. Fujisawa & Gotoh, 1992 observed that flow attachment improves the torque performance of a rotating Savonius rotor. The authors further observed that for a rotating Savonius rotor, flow separation occurs when angle of attack of the buckets is within of  $90^\circ$  and  $135^\circ$ ; for the case of the vaned Savonius rotor flow attachment to the convex side of the advancing is extended until the angle of attack of the rotor was at  $180^\circ$  before flow separation occurred. Figure 4-10 shows the particle path at a tip speed ratio of 0.9 for the rotor bucket with a  $180^\circ$  angle

of attack. The image on the left shows that the interaction between the downstream vanes and the flow causes an extended flow attachment to the convex side of the bucket. For the vaneless Savonius turbine, on the right, flow attachment to the advancing bucket is not observed at this angle. To the author's knowledge, the extension of flow attachment using downstream turbine is not documented in any literature, as such this is a novelty to this thesis.

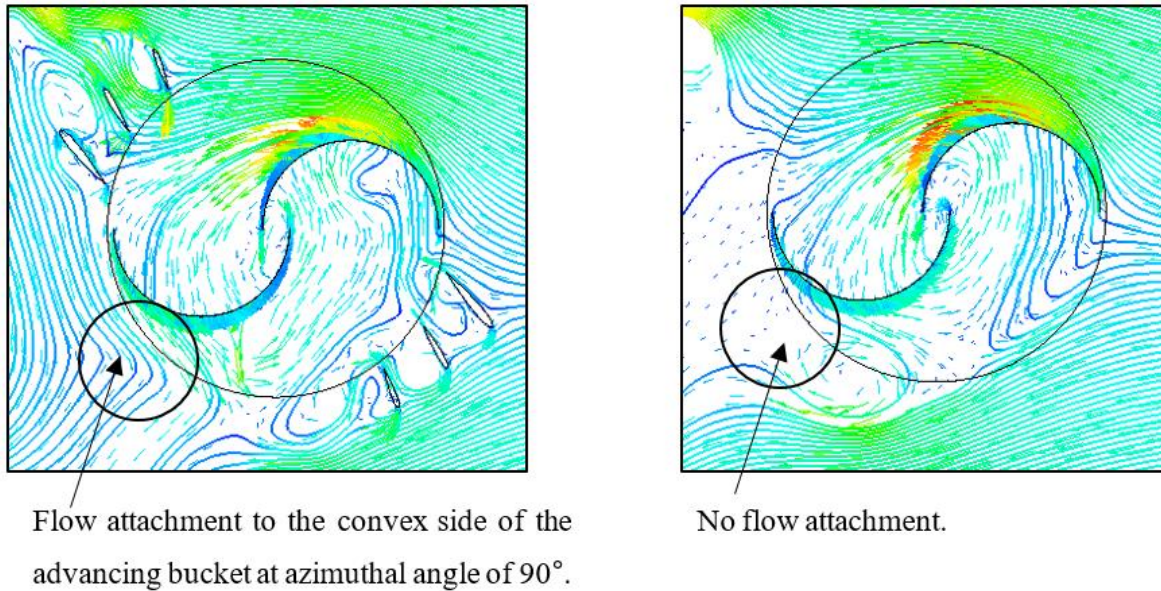


Figure 4-10: Streamlines showing particle path for the vaned (left) and vaneless (right) Savonius turbine.

Focusing our attention to the lower tip speed ratios; in addition to the extended flow attachment, another phenomenon responsible for improved advancing bucket performance is the presence of accelerated recirculating flow originating from the interaction of the upstream vanes with the main flow. This phenomenon is investigated using the control line *A*.

Concerning control line, *A*, at TSR of 0.5 and rotor angle of attack of  $-30^\circ$ , the advancing bucket lies between points 34 and 35. Figure 4-11 shows the pressure profile (left) and the velocity profile (right) along the control line *A* for the vaned (solid line) and the vaneless (dashed line) Savonius rotor at an angle of attack of  $-30^\circ$ . The observation is that the pressure on the convex side of the vaned turbine is lower than that of the vaneless turbine. This leads to a higher-pressure difference for the vaned turbine as the pressure on the concave side of the advancing bucket for both turbines are almost the same.

Prior to the convex surface (that is from points to 1 to 33) an oscillating velocity profile is observed in the vanned turbine. This oscillating profile is the outcome of a recirculating flow that is generated as the upstream stator vanes interact with the main flow. The interaction between the upstream vanes and the main flow accelerates the flow (seen in the generic flow model of Grönman, et al., 2018) and increases the flow velocity in the convex surface of the advancing blade. This is clearly visible in the velocity vector plot shown in figure 4-12.

The increased flow velocity is accompanied by a reduction in pressure, which leads to a larger pressure difference between the concave side and the convex side of the advancing bucket of the vanned Savonius turbine when compared to the vaneless rotor. The higher-pressure difference translates to better advancing bucket performance at this rotor angle for the vanned turbine. This phenomenon is observed at rotor buckets angle of attack in the range of  $-60^\circ$  to  $0^\circ$  for lower tip speed ratios of 0.4 to 0.7.

In summary, two phenomena are responsible for the improved performance on the advancing bucket of the vanned Savonius turbine. The first is the extended flow attachment caused by the interaction of the main flow with the downstream vanes. Secondly, the recirculating accelerated flow caused by the interaction of the upstream stator vanes with the main flow.

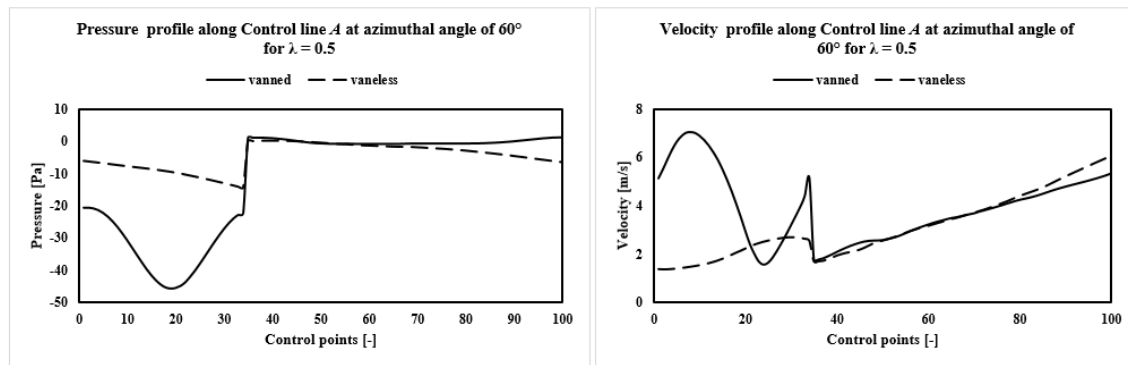


Figure 4-11: Pressure (left) and velocity (right) of control line A at a rotor angle of attack of  $-30^\circ$

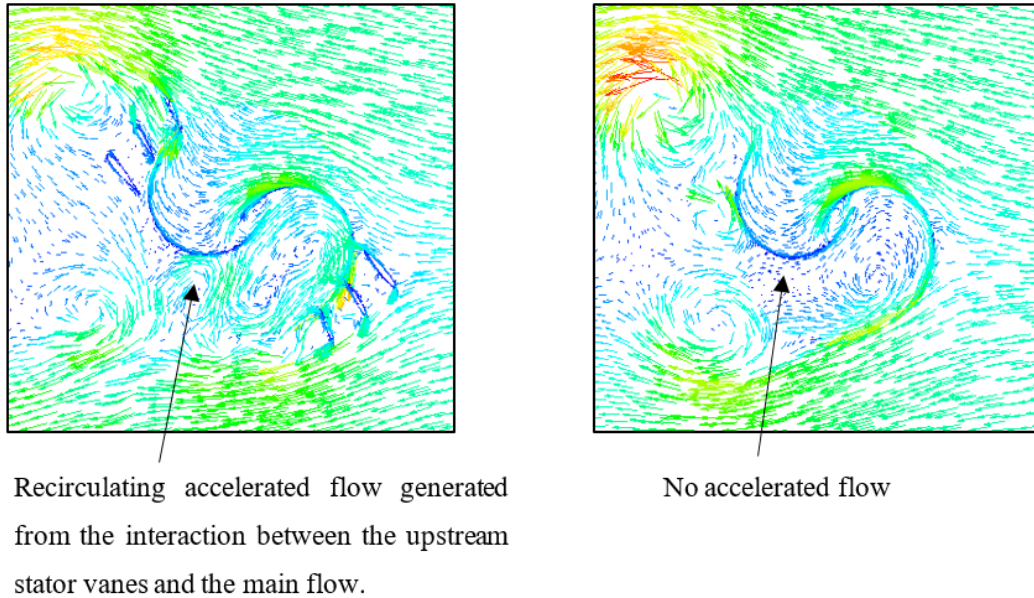


Figure 4-12: Velocity vector showing the flow around and within a vaned Savonius rotor (left) and a vaneless Savonius rotor (right). Rotor angle of attack is  $-30^\circ$  and the tip speed ratio is 0.5.

#### 4.2.2 Inferior torque performance analysis

The overall performance of the vaned Savonius turbine is inferior to the vaneless Savonius turbine, even though the rotor buckets experience some gain at certain angles as discussed in the previous section of this chapter. But ultimately, it has more angles of inferior performance than superior performance. This section will analyze the flow within the vaned Savonius rotor and compare it to the vaneless rotor; to find a meaningful explanation to the inferior performance as observed in the torque coefficient charts presented in figures 4-3 to 4-8, in the hopes of eliminating the causes.

The phenomena that cause the negative turbine performance is the same for all design points, as such only design point, 6 is analyzed in this section. But the analysis is done at two different angles of attack which are  $-60^\circ$  and  $30^\circ$ . Figure 4-13 shows the particle path within and around a Savonius turbine with a  $-60^\circ$  rotor bucket angle of attack. Focusing our attention to the vicinity of the upstream stator vanes, the quick observation is that the upstream vanes intercept the main flow before it reaches the returning bucket. The presence of the stator vanes totally halts flow attachment to the convex side of the returning bucket, thereby reducing the torque performance at this rotor angle of attack. This phenomenon is also common to other rotor angles.



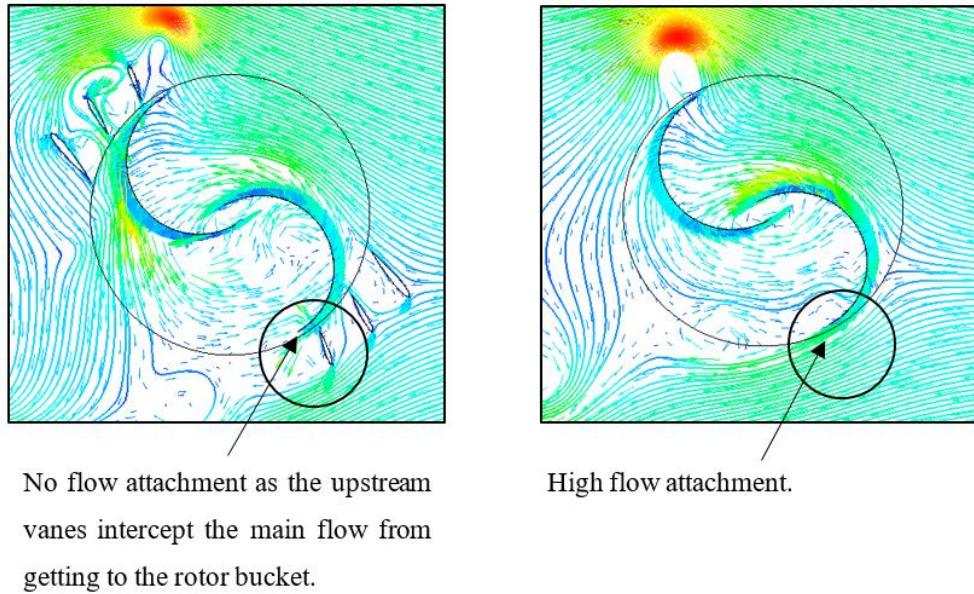


Figure 4-13: Velocity and particle path of vaned and vaneless Savonius turbine at TSR of 0.9, and a rotor angle of attack of  $-60^\circ$ .

Regarding higher angles of attack of  $-30^\circ$  and above, in addition to the reduced flow attachment, the wake and the vortices generated by the upstream vanes as it interacts with the main flow reduces the performance of the vaned Savonius turbine. To elucidate this phenomenon, flow parameters along control line B is examined at a rotor angle of  $30^\circ$ . At this rotor angle, the returning bucket is between control points 91 and 92 of the control line *B*. Examining the pressure profile along the control line *B* (see figure 4-14) clearly shows a reduced pressure on the concave side of the returning bucket. The pressure drop is as a result of velocity fluctuation caused by the wake generated by the interaction of the upstream stator with the main flow. This phenomenon is visible from the pressure contour plot in figure 4-15.

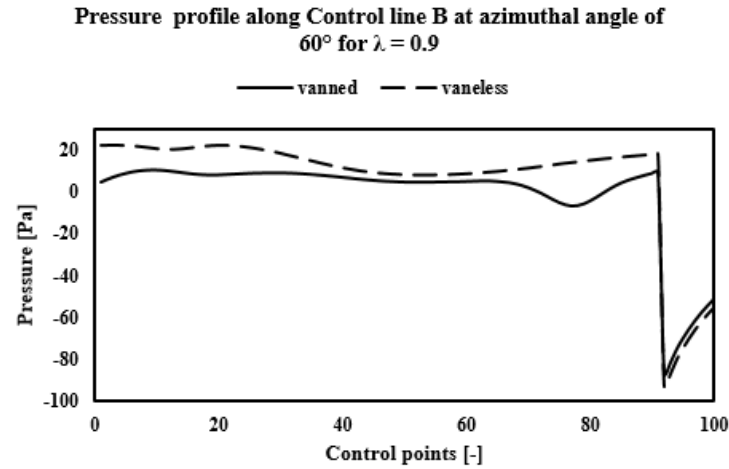


Figure 4-14: Pressure profile of control line B at a rotor angle of attack of  $-30^\circ$

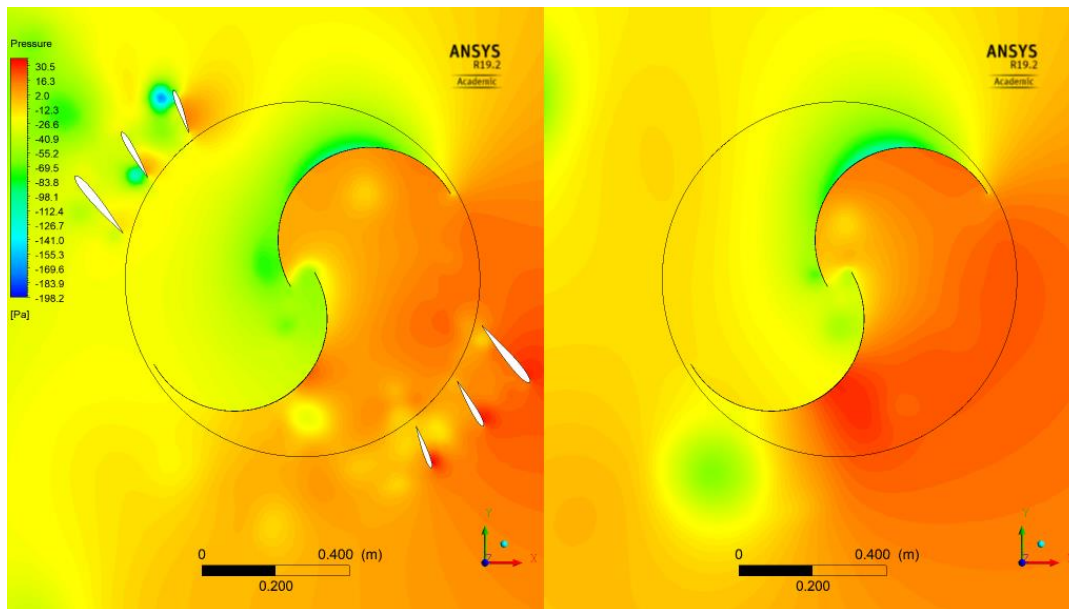


Figure 4-15: Pressure contour plots of vanned (left) and vaneless (right) Savonius turbine at TSR 0.9 and a rotor angle of attack of  $-30^\circ$ .

Therefore, the conclusion is that the two phenomena that reduce the performance of the vanned Savonius turbine are the flow separation caused by the flow interception by the upstream vanes before it reaches the convex side of the rotor bucket. The second is the pressure reduction on the concave surface of the bucket by the wakes and vortices generated from the interaction of the upstream vanes with the main flow.

### 4.3 Results summary

This section has presented and the discussed the results obtained from the simulation of the vaned and the vaneless Savonius turbine. In the first part of this chapter, the average performance parameters of the simulated turbines were examined. The results show that the vaneless turbine was superior to vaned Savonius turbine in all turbine performance parameters, even though there are certain rotor bucket angles in which the vaned configuration outperformed the vaneless rotor. The second part of this chapter was focused on elucidating why the vaned turbine performed so badly and if there is anything advantageous in using this configuration for the Savonius turbine. The following observations were made.

On the issue of improved performance;

1. The interaction of the main flow and the downstream stator vanes causes an extended flow attachment on the convex side of the advancing bucket which improves the rotor bucket performance. This extended flow attachment is a novelty to this thesis, as to the author's knowledge, this has not been documented in any literature.
2. The interaction of the upstream vanes with the main flow generates an accelerated recirculating flow which reduces the pressure on the convex side of the advancing bucket.

On the issue of reduced performance;

1. The upstream stator vanes intercept flow from getting to the convex side of the returning bucket and thereby reducing flow attachment. This, in turn, reduces the performance of the turbine.
2. The interaction of the upstream vanes with the main flow generates vortices and wake that reduces the pressure on the concave side of the returning blade. This reduces the pressure difference between the concave and the convex side of the returning blade.



## 5 CONCLUSION

This chapter presents a recap of the main findings and novelty of this thesis and the answers to the research questions. Finally, the proposal for future research work is presented.

### 5.1 Findings of the thesis

The full aim of adding the NACA 0012 stator vanes to the turbine was to improve the Savonius rotor performance. But unfortunately, the addition of the stator vanes did not improve the performance instead it diminished the Savonius turbine performance. On the bright note, this thesis has presented how NOT to configure a Savonius turbine.

Irrespective of the overall negative performance of the vaned configuration, some phenomena were observed that improved the performance of the Savonius turbine. And this phenomenon could be implemented in the future construction of a Savonius turbine. The most important and noticeable one is the flow attachment extension on the convex side of the bucket due to the interaction of the downstream vanes and the main flow. This phenomenon is a novelty to this thesis as this has never been documented in any literature to the best of the author's knowledge.

Concerning, the answers to the first research question asked in the first chapter, on **how to effectively increase the aerodynamic power coefficient of the Savonius turbine?**

Following the result presented in chapter 4 of this thesis. The suggestion for improved Savonius wind turbine performance is the utilization of only the downstream vanes when configuring a Savonius rotor (see figure 5-1). Using only the downstream vanes will enhance the performance of the Savonius by extending flow attachment on the convex side of the rotor buckets till a rotor bucket angle of attack of  $180^\circ$ . On the other hand, not using the upstream vanes will get rid of the disadvantages that arise as a result of the interaction of the upstream vanes with the main flow.

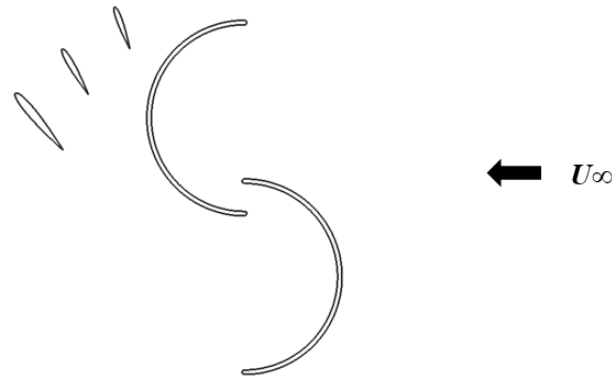


Figure 5-1: Proposed configuration for the Savonius turbine.

The backlash to this configuration is that the Savonius turbine will become unidirectional and will require a yawing system to rotate in the direction of the main flow. But this will be compensated by the increased performance.

The second research question on **how to correctly use CFD to analysis the aerodynamics of a Savonius turbine?**

To effectively use CFD to analyze the aerodynamics of the Savonius turbine the following steps are suggested.

- i. Design an accurate geometry representing the Savonius turbine.
- ii. Generate a computational domain large enough so that the domain does not affect the flow field.
- iii. Use accurate and physical representative solver settings and initial conditions.
- iv. Run the transient simulation for at least five rotations and finally,
- v. Validate the simulation results with available experimental data.

## 5.2 Recommendation for future work

For the future work, simulation and experimental study of the proposed modification of using just the downstream vanes could be done. The shape, the length, and distances between the vanes could be varied to achieve the optimum geometry configuration.

In this thesis wind tunnel conditions were used; further work could include open environment test conditions. Also, the use of a 3-dimensional geometry could help elucidate the pressure distribution on the vaned Savonius turbine configuration.

## REFERENCES

- Abbott, I. H., Doenhoff, A. E. V. & Louis S. Stivers, J., 1945. *Summary of Airfoil Data*, Virginia: Langley Memorial Aeronautical Laboratory.
- Akwa, J. V., Vielmo, H. A. & Petry, A. P., 2012. A review on the performance of Savonius wind turbines. *Renewable and Sustainable Energy Reviews*, Volume 16, pp. 3054-3064.
- Alexander, A. & Holownia, B., 1978. Wind tunnel tests on a savonius rotor. *Journal of Wind Engineering and Industrial Aerodynamics*, Volume 3, pp. 343-351.
- Almohammadi, K., Ingham, D., Maa, L. & Pourkashan, M., 2013. Computational fluid dynamics (CFD) mesh independency techniques for a straight blade vertical axis wind turbine. *Energy*, Volume 58, pp. 483-493.
- Altan, B. & Atilgan, M., 2008. An experimental and numerical study on the improvement of the performance of Savonius wind rotor.. *Energy conversion and Mangement*, 49(12), pp. 3425-3432.
- Balduzzi, F. et al., 2016. Critical issues in the CFD simulation of Darrieus wind turbines. *Renewable Energy*, Volume 85, pp. 419-435.
- Blackwell, B. F., Sheldahl, R. E. & Feltz, L. V., 1977. *Wind Tunnel Performance Data for Two- and Three- Bucket Savonius Rotors*, New Mexico: Sandia Laboratories.
- Burton, T., Sharpe, D., Jenkins, N. & Bossanyi, E., 2001. *Wind Energy Handbook*. 1st ed. West Sussex : John Wiley & Sons, Ltd.
- C.H, C., C, S., W, P. & Rivas, S., 2011. *Cities of tomorrow Challenges, visions, ways forward*, Brussel: European Commission, Directorate General for Regional Policy.
- D'Alessandro, V., Montelpare, S., Ricci, R. & Secchiaroli, A., 2010. Unsteady Aerodynamics of a Savonius wind rotor: a new computational approach for the simulation of energy performance. *Elsevier Energy*, Volume 35, pp. 3349 - 3363.
- Damak, A., Driss, Z. & Abid, M., 2012. Experimental investigation of Savonius rotor with a twist of 180 degrees. *Renewable Energy*, Volume 52, pp. 136-142.

EEA technical report, 2009. *Europe's onshore and offshore wind energy potential - An assessment of environmental and economic constraints*, Copenhagen: European Environment Agency.

EEA technical report, 2017. *Renewable energy in Europe – 2017 Update. Recent growth and knock-on effects*, Copenhagen: European Environment Agency.

El-Askary, W., Nasef, M., AbdEL-hamid, A. & Gad, H., 2015. Harvesting wind energy for improving performance of Savonius rotor. *Journal of Wind Engineering and Industrial Aerodynamics*, Issue 139, pp. 8-15.

Energy Department, 2012. *Finland's national action plan for promoting energy from renewable sources pursuant to Directive 2009/28/EC*, s.l.: MINISTRY OF EMPLOYMENT AND THE ECONOMY.

EurObserv'ER, 2010. *Wind Energy Barometer*, Paris: s.n.

EurObserv'ER, 2011. *Wind Energy Barometer*, Paris: s.n.

EurObserv'ER, 2012. *Wind Energy Barometer*, Paris: s.n.

EurObserv'ER, 2013. *Wind Energy Barometer*, Paris: s.n.

EurObserv'ER, 2014. *Wind Energy Barometer*, Paris: s.n.

EurObserv'ER, 2015. *Wind Energy Barometer*, Paris: s.n.

EurObserv'ER, 2016. *Wind Energy Barometer*, Paris: s.n.

EurObserv'ER, 2017. *Wind Energy Barometer*, Paris: s.n.

EurObserv'ER, 2018. *Wind energy barometer*, Paris: s.n.

Fluent Inc., 2001. *FLUENT 6.0 User's Guide*. New Hampshire: Fluent Inc..

Fujisawa, N., 1992. On the torque mechanism of Savonius rotors.. *Wind Energy and Industrial Aerodynamics*, Volume 40, pp. 277-292.

Fujisawa, N. & Gotoh, F., 1992. Visualization study of the flow in and around a Savonius rotor. *Experiments in Fluids*, Volume 12, pp. 407-412.

Global Wind Energy Council, 2016. *Global Wind Report*, Brussels: s.n.

Grönman, A. et al., 2018. Experimental and numerical analysis of vaned wind turbine performance and flow phenomena. *Energy*, Volume 159, pp. 827-841.

Hau, E., 2013. *Wind Turbines Fundamentals, Technologies, Application, Economics*. 3rd ed. Munich: Springer.

Hau, E., 2013. *Wind Turbines Fundamentals, Technologies, Applications, Economics*. 3rd ed. Heidelberg: Springer.

International Symposium on Wind Energy Systems; BHRA (Association); Sweden. Namnden for energiproduktionsforskning, 1982. *Papers presented and published at the Fourth International Symposium on Wind Energy Systems held at Stockholm, Sweden*. Stockholm, BHRA Fluid Engineering.

Irabu, K. & Roy, J. N., 2007. Characteristics of wind power on Savonius rotor using a guide-box tunnel. *Experimental Thermal and Fluid Science*, Volume 32, pp. 580-586.

Jaohindy, P., McTavish, S., Garde, F. & Bastide, A., 2013. An analysis of the transient forces acting on Savonius rotors with different aspect ratios. *Renewable Energy*, Volume 55, pp. 286-295.

Kacprzak, K., Liskiewicz, G. & Sobczak, K., 2013. Numerical investigation of conventional and modified Savonius wind turbines. *Renewable Energy*, Volume 60, pp. 578-585.

Kamoji, M., Kedare, S. & Prabhu, S., 2008. Experimental investigations on single stage modified Savonius rotor. *Applied Energy*, Volume 86, pp. 1064-1073.

Kang, C., Liu, H. & Yang, X., 2014. Review of fluid dynamics aspects of Savonius-rotor-based vertical-axis wind rotors. *Renewable and Sustainable Energy Reviews*, Volume 33, pp. 499-508.

Ledo, L., Kosasih, P. & Cooper, P., 2011. Roof mounting site analysis for micro-wind turbines. *Renewable Energy*, Volume 36, pp. 1379-1391.

Lee, J.-H., Lee, Y.-T. & Lim, H.-C., 2016. Effect of twist angle on the performance of Savonius wind turbine. *Renewable Energy*, Volume 89, pp. 231-244.

- Marmutova, S., 2016. *Performance of a Savonius wind turbine in urban sites using CFD analysis*, Vaasa: Vaasan yliopisto.
- Menter, F. R., 1994. Two-Equation Eddy-Viscosity Turbulence Models for Engineering Applications. *American Institute of Aeronautics and Astronautics*, 32(8), pp. 1598-1605.
- Mohamed, M., Janiga, G., Pap, E. & Thévenin, D., 2010. Optimization of Savonius turbines using an obstacle shielding the returning blade. *Renewable Energy*, Volume 35, pp. 2618-2626.
- Mojola, O., 1985. On aerodynamic design of the Savonius windmill rotor. *Journal of Wind Engineering and Industrial Aerodynamics*, Volume 21, pp. 223-231.
- Paraschivoiu, I., 2002. *Wind Turbine Design With Emphasis on Darrieus Concept*. Quebec: Presses internationales Polytechnique.
- Pointer, J., n.d. *Understanding Accuracy and Discretization Error in an FEA Model*, s.l.: s.n.
- Pointwise, 2018. *Pointwise*. [Online]  
Available at: <https://www.pointwise.com/about/index.html>  
[Accessed 9 September 2018].
- Pope, K. et al., 2010. Effects of stator vanes on power coefficients of a Zephyr vertical axis wind turbine. *Renewable Energy*, Volume 35, pp. 1043-1051.
- Roy, S. & UjjwalK.Saha, 2013. Review on the numerical investigations into the design and development of Savonius wind rotors. *Renewable and Sustainable Energy Reviews*, Volume 24, pp. 73-83.
- Saha, U., Thotla, S. & Maity, D., 2008. Optimum design configuration of Savonius rotor through wind tunnel experiments.. *Journal of Wind Engineering and Industrial Aerodynamics*, Volume 96, pp. 1359-1375.
- Schubel, P. J. & Crossley, R. J., 2012. Wind Turbine Blade Design. *Energies*, pp. 3425-3449.
- Shahizare, B. et al., 2016. Investigation of the optimal omni-direction-guide-vane design for vertical axis wind turbines based on unsteady flow CFD simulation.. *Energies*, 9(146).

Shahizare, B. et al., 2016. Novel investigation of the different omni-direction-guide vane angles effects on the urban vertical axis wind turbine output power via three-dimensional numerical simulation.. *Energy Conversion and Management*, Volume 117, pp. 206-217.

Sheldahl, R., Feltz, L. & Blackwell, B., 1978. Wind tunnel performance data for two- and three-bucket Savonius rotors.. *Journal of Energy*, Volume 2, pp. 160-164.

Shigetomi, A., Murai, Y., Tasaka, Y. & Takeda, Y., 2011. Interactive flow field around two Savonius turbines. *Elsevier Renewable Energy*, Volume 36, pp. 536-545.

Ushiyama, I. & Nagai, H., 1988. Optimum design configurations and performance of SavoSavonius. *Wind Energy*, Volume 12, pp. 59-75.

Wenehenubun, F., Saputra, A. & Sutanto, H., 2015. An experimental study on the performance of Savonius wind turbinesrelated with the number of blades. *Energy Procedia*, Volume 68, pp. 297-304.

Versteeg, H. K. & Malalasekera, W., 2007. *An Introduction to Computational Fluid Dynamics*. 2nd ed. Essex: Pearson Education Limited.

Wilcox, D. C., 2006. *Turbulence Modeling for CFD*. 3rd ed. California: DCW Industries.

WindEurope, 2018. *Wind in power 2017 Annual combined onshore and offshore wind energy statistics*, Brussel: s.n.

Zhang, B., Song, B., Mao, Z. & Tian, W., 2017. A novel wake energy reuse method to optimize the layout for Savonius-type vertical axis wind turbines. *Energy*, Volume 121, pp. 341-355.

Zhao, Z. et al., 2009. *Research on the Improvement of the Performance of Savonius Rotor Based on Numerical Study*. Nanjing, International Conference on Sustainable Power Generation and Supply.

Zikanov, O., 2010. *Essential computational fluid dynamics*. New Jersey: John Wiley & Sons, Inc.



## APPENDIX I

### SST $k$ - $\omega$ Model Transport Equations

$$\frac{\partial}{\partial t}(\rho k) + \frac{\partial}{\partial x_i}(\rho k u_i) = \frac{\partial}{\partial x_j} \left( \Gamma_k \frac{\partial k}{\partial x_j} \right) + G_k - Y_k + S_k \quad \text{I-1}$$

And

$$\frac{\partial}{\partial t}(\rho \omega) + \frac{\partial}{\partial x_i}(\rho \omega u_i) = \frac{\partial}{\partial x_j} \left( \Gamma_\omega \frac{\partial \omega}{\partial x_j} \right) + G_\omega - Y_\omega + D_\omega + S_\omega \quad \text{I-2}$$

In these equations,  $G_k$  represents turbulent kinetic energy generation, and  $G_\omega$  represents specific dissipation rate generation.  $\Gamma_k$  and  $\Gamma_\omega$  represent the effective diffusivity of  $k$  and  $\omega$ . Also,  $Y_k$  and  $Y_\omega$  are a dissipation of  $k$  and  $\omega$  due to turbulence. Finally,  $D_\omega$  is a cross-diffusion term while  $S_k$  and  $S_\omega$  are source terms.

### Modeling Effective Diffusivity

$$\Gamma_k = \mu + \frac{\mu_t}{\sigma_k} \quad \text{I-3}$$

$$\Gamma_\omega = \mu + \frac{\mu_t}{\sigma_\omega} \quad \text{I-4}$$

Where  $\sigma$  is the turbulent Prandtl numbers and  $\mu_t$  is the turbulent viscosity computed as

$$\mu_t = \frac{\rho k}{\omega} \frac{1}{\max \left[ \frac{1}{\alpha^*}, \frac{\Omega F_2}{\alpha_1 \omega} \right]} \quad \text{I-5}$$

Where

$$\Omega \equiv \sqrt{2\Omega_{ij}\Omega_{ij}} \quad \text{I-6}$$

$\Omega_{ij}$  is the average rate of rotation tensor and is given by

$$\Omega_{ij} = \frac{1}{2} \left( \frac{\partial u_i}{\partial x_j} - \frac{\partial u_j}{\partial x_i} \right) \quad \text{I-7}$$

$$\sigma_k = \frac{1}{\frac{F_1}{\sigma_{k,1}} + (1 - F_1)/\sigma_{k,2}} \quad \text{I-8}$$

$$\sigma_\omega = \frac{1}{\frac{F_1}{\sigma_{\omega,1}} + (1 - F_1)/\sigma_{\omega,2}} \quad \text{I-9}$$

### Low Reynolds number correction

$\alpha^*$  is responsible for low Reynolds number correction by damping the turbulent viscosity and it is given by

$$\alpha^* = \alpha_\infty^* \left( \frac{\alpha_0^* + Re_t/R_k}{1 + Re_t/R_k} \right) \quad \text{I-10}$$

Where

$$Re_t = \frac{\rho k}{\mu \omega} \quad \text{I-11}$$

$$R_k = 6 \quad \text{I-12}$$

$$\alpha_0^* = \frac{\beta_i}{3} \quad \text{I-13}$$

$$\beta_i = F_1 \beta_{i,1} + (1 - F_1) \beta_{i,2} \quad \text{I-14}$$

$\alpha_\infty^* = 1$ , for high Reynolds-number flow  $\alpha^* = \alpha_\infty^* = 1$ ,  $\beta_{i,1} = 0.075$  and  $\beta_{i,2} = 0.0828$ .

The blending functions  $F_1$  and  $F_2$  are given by

$$F_1 = \tanh(\Phi_1^4) \quad \text{I-15}$$

$$\Phi_1 = \min \left[ \max \left( \frac{\sqrt{k}}{0.09\omega y}, \frac{500\mu}{\rho y^2 \omega} \right), \frac{4\rho k}{\sigma_{\omega,2} D_{\omega}^+ y^2} \right] \quad \text{I-16}$$

$$D_{\omega}^+ = \max \left[ 2\rho \frac{1}{\sigma_{\omega,2}} \frac{1}{\omega} \frac{\partial k}{\partial x_j} \frac{\partial \omega}{\partial x_j}, 10^{-20} \right] \quad \text{I-17}$$

$$F_2 = \tanh(\Phi_2^2) \quad \text{I-18}$$

$$\Phi_2 = \max \left[ \frac{\sqrt{k}}{0.09\omega y}, \frac{500\mu}{\rho y^2 \omega} \right] \quad \text{I-19}$$

Where  $y$  is the distance to the next surface and  $D_{\omega}^+$  is the positive portion of the cross-diffusion term.

### Modeling turbulence production

Two terms represent the turbulence production in the SST  $k$ - $\omega$  transport equations; these terms are  $G_k$  and  $G_{\omega}$ .  $G_k$  represents the production of turbulence kinetic energy while  $G_{\omega}$  represents the specific dissipation rate production.

Production of  $k$

From the transport equation of  $k$ ,  $G_k$  may be defined as

$$G_k = \rho \bar{u}_i' \bar{u}_j' \frac{\partial u_j}{\partial x_i} \quad \text{I-20}$$

Applying the Boussinesq hypothesis in equation I-20,  $G_k$  becomes

$$G_k = \mu_t S^2 \quad \text{I-21}$$

Where  $S$  is the modulus of the average rate-of-strain tensor defined as

$$S \equiv \sqrt{2S_{ij}S_{ij}} \quad \text{I-22}$$

And

$$S_{ij} = \frac{1}{2} \left( \frac{\partial u_j}{\partial x_i} + \frac{\partial u_i}{\partial x_j} \right) \quad \text{I-23}$$

### Production of $\omega$

The production of  $\omega$  is represented by  $G_\omega$  in the transport equation, and it is given by

$$G_\omega = \frac{\alpha}{\nu_t} G_k \quad \text{I-24}$$

Where

$$\alpha = \frac{\alpha_\infty}{\alpha^*} \left( \frac{\alpha_0 + Re_t/R_\omega}{1 + Re_t/R_\omega} \right) \quad \text{I-25}$$

$R_\omega = 2.95$ , and  $\alpha_\infty$  is given as

$$\alpha_\infty = F_1 \alpha_{\infty,1} + (1 - F_1) \alpha_{\infty,2} \quad \text{I-26}$$

$$\alpha_{\infty,1} = \frac{\beta_{i,1}}{\beta_\infty^*} - \frac{\kappa^2}{\sigma_{\omega,1} \sqrt{\beta_\infty^*}} \quad \text{I-27}$$

$$\alpha_{\infty,2} = \frac{\beta_{i,2}}{\beta_\infty^*} - \frac{\kappa^2}{\sigma_{\omega,2} \sqrt{\beta_\infty^*}} \quad \text{I-28}$$

$\kappa = 0.41$ ,  $\beta_{i,1} = 0.075$  and  $\beta_{i,2} = 0.0828$ ,  $\beta_\infty^* = 0.09$ .

### Modeling turbulence dissipation

Turbulence dissipation is represented by  $Y_k$  and  $Y_\omega$  in the transport equation of the SST  $k-\omega$  model.

$Y_k$  is the dissipation of turbulent kinetic energy while  $Y_\omega$  is the dissipation of  $\omega$ .

Dissipation of  $k$

$$Y_k = \rho \beta^* f_{\beta^*} k \omega \quad \text{I-29}$$

Where  $f_{\beta^*} = 1$

$$\beta^* = \beta_\infty^* [1 + \beta_\infty^* \beta_\beta \beta_\beta] \quad \text{I-30}$$

$$\beta_i^* = \beta_\infty^* \left( \frac{4/15 + (Re_t/R_\beta)^4}{1 + (Re_t/R_\beta)^4} \right) \quad \text{I-31}$$

$\zeta^* = 1.5$ ,  $R_\beta = 8$  and  $\beta_\infty^*$  was given in the production of  $\omega$  section.  $F(M_t)$  is the compressibility correction function based on the turbulent Mach number, and it is given in equation I-34.

### Dissipation of $\omega$

$$Y_\omega = \rho \beta f_\beta \omega^2 \quad \text{I-32}$$

Where  $f_\beta = 1$  and,

$$\beta = \beta_i \left[ 1 + \frac{\beta_i^*}{\beta_i} \zeta^* F(M_t) \right] \quad \text{I-33}$$

Where  $\beta_i$  and  $\beta_i^*$  are defined in equation I-14 and I-31 respectively.

### Compressibility correction

$$F(M_t) = \begin{cases} 0 & M_t \leq M_{t0} \\ M_t^2 - M_{t0}^2 & M_t > M_{t0} \end{cases} \quad \text{I-34}$$

Where

$$M_t^2 = \frac{2k}{a^2} \quad \text{I-35}$$

$$M_{t0} = 0.25 \quad \text{I-36}$$

$$a = \sqrt{\gamma RT} \quad \text{I-37}$$

### Cross-Diffusion Modification

The cross-diffusion term,  $D_\omega$ , in the SST  $k$ - $\omega$  transport equation is as a result of the transformation of the  $k$ - $\epsilon$  model into equations based on  $k$  and  $\omega$ . The cross-diffusion term  $D_\omega$  is given by

$$D_{\omega} = 2(1 - F_1)\rho\sigma_{\omega,2}\frac{1}{\omega}\frac{\partial k}{\partial x_j}\frac{\partial \omega}{\partial x_j}$$

I-38

### Model Constants

$$\sigma_{k,1} = 1.176, \sigma_{\omega,1} = 2.0, \sigma_{k,2} = 1.0, \sigma_{\omega,2} = 1.168, a_1 = 0.31$$

## APPENDIX II

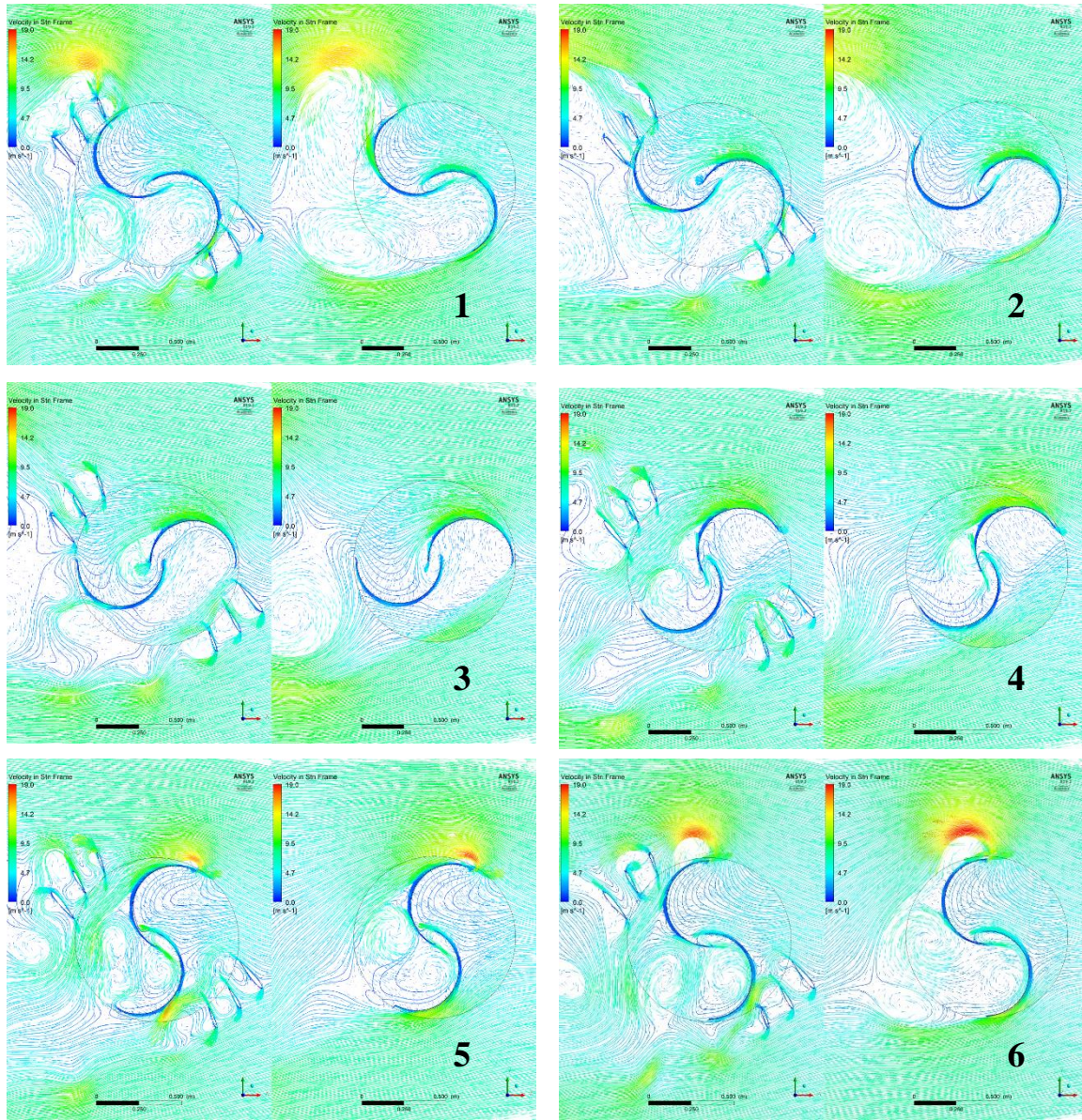


Figure II-1: Streamlines and velocity vector showing the flow stream in a vaned and vaneless Savonius turbine for various angles at TSR of 0.4. (1) is for rotor angle of 30, (2) is for angle of 60, (3) is for angle of 90, (4) is for angle of 120, (5) is for angle of 150 and, (6) is for angle of 180.



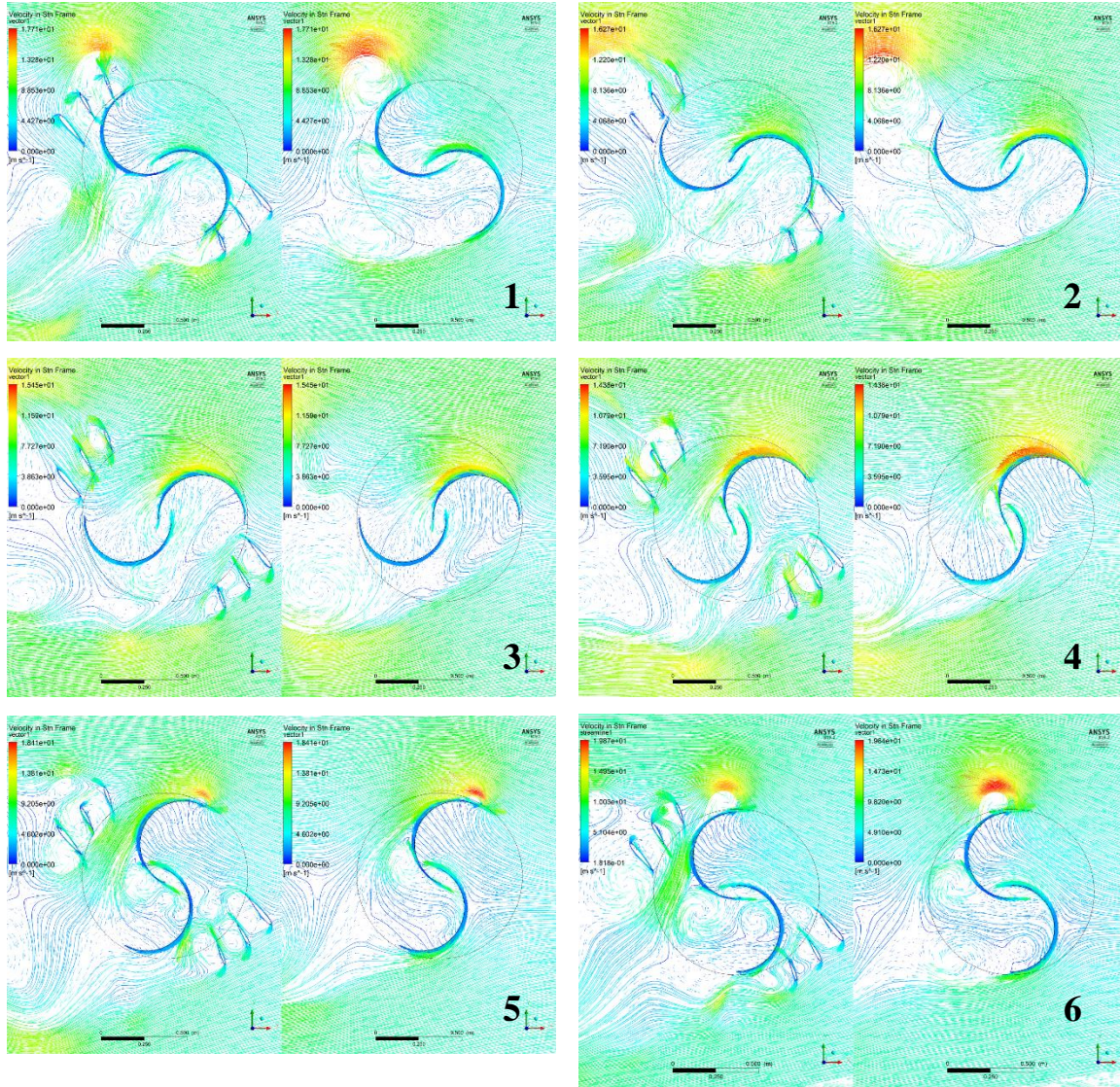


Figure II-2: Streamlines and velocity vector showing the flow stream in a vaned and vaneless Savonius turbine for various angles at TSR of 0.5. (1) is for rotor angle of 30, (2) is for angle of 60, (3) is for angle of 90, (4) is for angle of 120, (5) is for angle



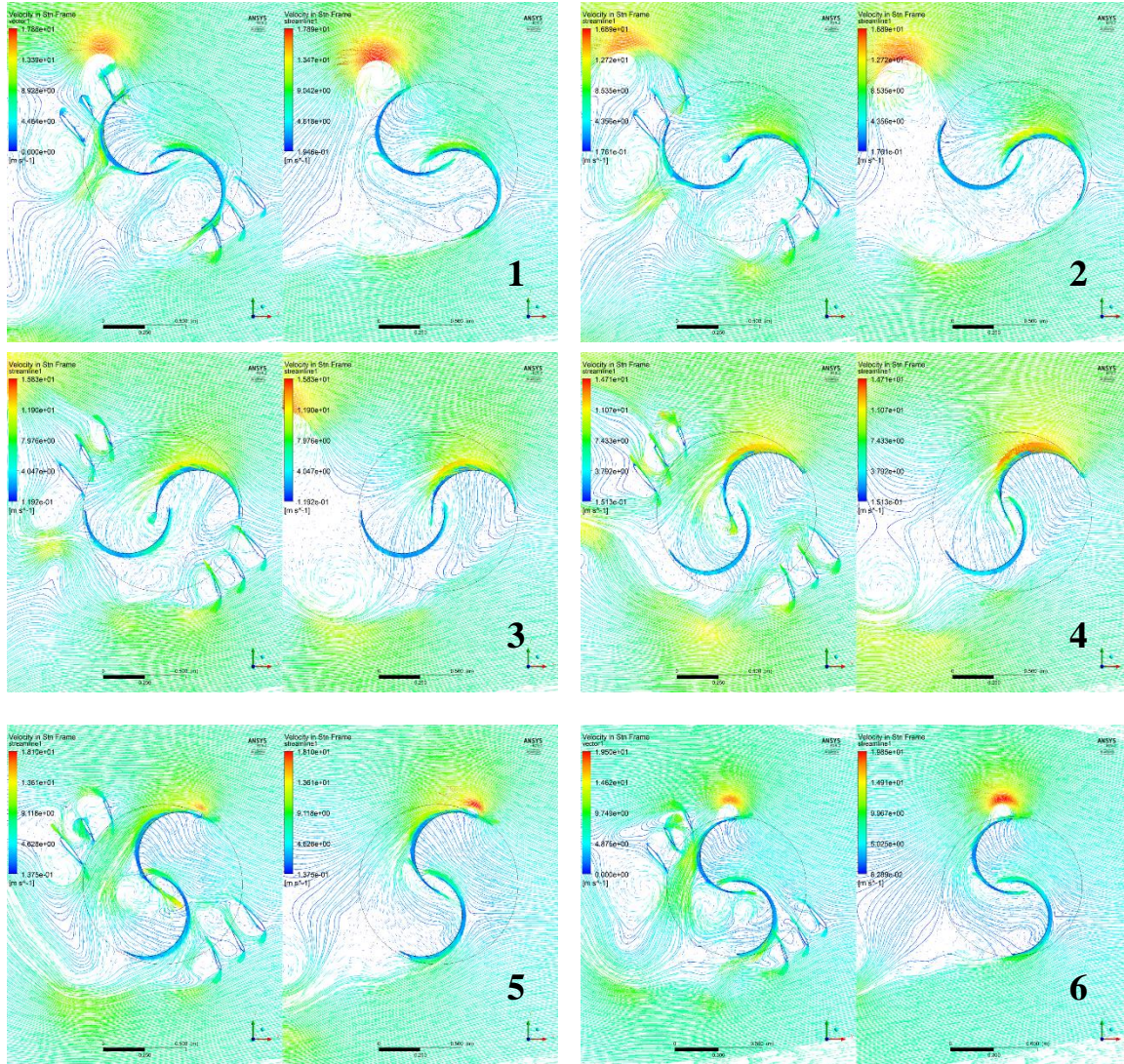


Figure II-3: Streamlines and velocity vector showing the flow stream in a vaned and vaneless Savonius turbine for various angles at TSR of 0.6. (1) is for rotor angle of 30, (2) is for angle of 60, (3) is for angle of 90, (4) is for angle of 120, (5) is for angle.



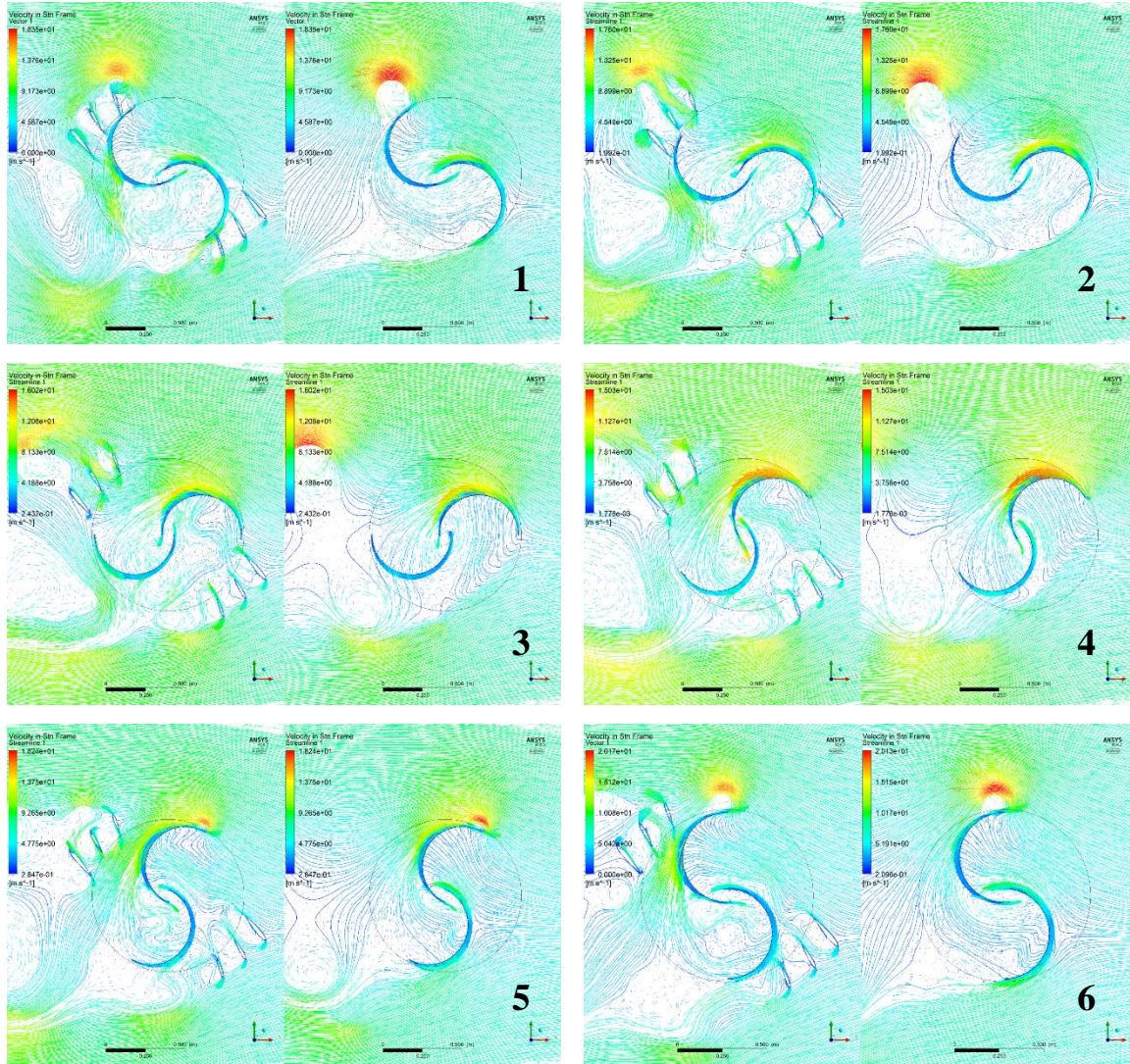


Figure II-4: Streamlines and velocity vector showing the flow stream in a vaned and vaneless Savonius turbine for various angles at TSR of 0.7. (1) is for rotor angle of 30, (2) is for angle of 60, (3) is for angle of 90, (4) is for angle of 120, (5) is for angle.



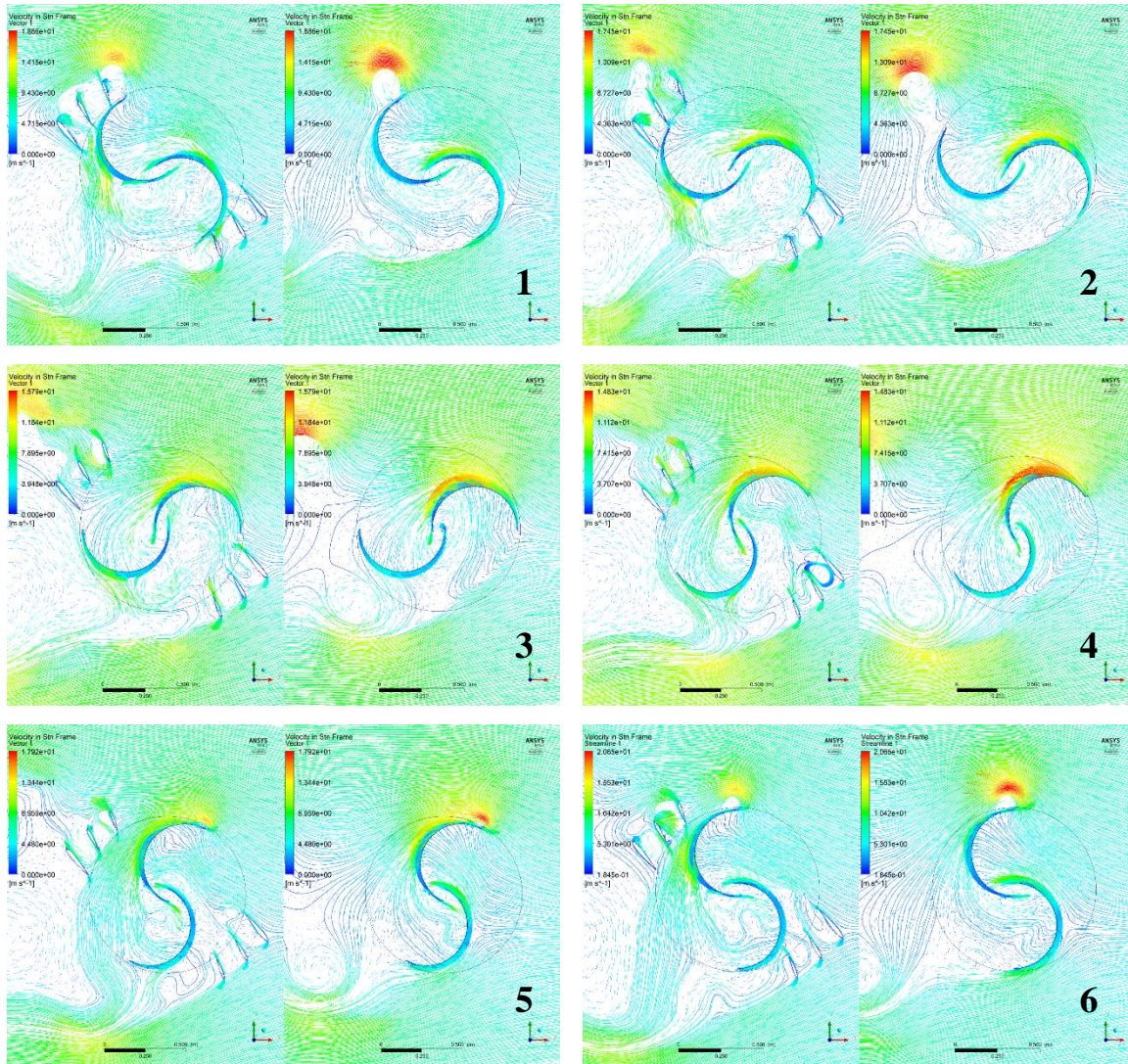


Figure II-5: Streamlines and velocity vector showing the flow stream in a vaned and vaneless Savonius turbine for various angles at TSR of 0.8. (1) is for rotor angle of 30, (2) is for angle of 60, (3) is for angle of 90, (4) is for angle of 120, (5) is for angle.



Figure II-6: Streamlines and velocity vector showing the flow stream in a vaned and vaneless Savonius turbine for various angles at TSR of 0.9. (1) is for rotor angle of 30, (2) is for angle of 60, (3) is for angle of 90, (4) is for angle of 120, (5) is for angle.